Master's thesis

NTNU
Norwegian University of Science and Technology
Faculty of Natural Sciences
Department of Chemical Engineering

Sahra Louise Guldahl-Ibouder

Selectively oxygen-functionalized carbon-supported cobalt catalysts for Fischer-Tropsch synthesis

Master's thesis in Chemical Engineering and Biotechnology
Supervisor: Magnus Rønning
Co-supervisor: Felix Herold
June 2023

NTNU
Norwegian University of
Science and Technology

Sahra Louise Guldahl-Ibouder

Selectively oxygen-functionalized carbon-supported cobalt catalysts for Fischer-Tropsch synthesis

Master's thesis in Chemical Engineering and Biotechnology
Supervisor: Magnus Rønning
Co-supervisor: Felix Herold
June 2023

Norwegian University of Science and Technology
Faculty of Natural Sciences
Department of Chemical Engineering

NTNU
Norwegian University of
Science and Technology

Acknowledgements

This master's thesis is the final work of a five years master's program in Chemical Engineering and Biotechnology at the Norwegian University of Science and Technology and was carried out in the Catalysis group at the Department of Chemical Engineering.

Firstly I would like to thank my supervisor, Professor Magnus Rønning. His continuous support and advice throughout the master's thesis have been invaluable. Secondly, I would like to extend my gratitude to my co-supervisor, Dr. Felix Herold. The guidance and support I have received have truly been beyond my expectations.

I would also like to thank Estelle Marie M. Vanhaecke for giving me the required training and for technical assistance in the lab, but also for the warm welcome and inclusion of the master's students into the catalysis group.

In addition, I would like to thank Oliver Leubner at the Technical University of Darmstadt for performing the Temperature programmed desorption measurements presented in the thesis.

Abstract

Cobalt catalyzed Fischer-Tropsch (FT) synthesis is a viable way of producing synthetic liquid fuels and chemicals from sustainable feedstocks such as biomass and non-recyclable plastic waste. Common support materials for FT catalysts are refractory oxides such as alumina and silica [1, 2]. However, the interaction between the support and the cobalt can lead to the formation of inactive and unreducable phases such as $CoAl_2O_4$ and $CoSiO_4$ [3]. Carbon exhibits a lot of the same desirable properties as the oxides mentioned previously, but it does not interact as strongly with the metal particles [4, 5]. However, because of the low metal-support interactions, it can be challenging to obtain a good dispersion, and a significant degree of sintering is commonly observed. A way to mitigate these problems is by introducing oxygen functional groups to the carbon surface. The oxygen functional groups are expected to act as anchoring sites and immobilize the metal particles. Although a lot of research has been carried out on oxidized carbon supports for cobalt catalyzed FT synthesis, little attention has been paid to selective oxygen functionalization to investigate the influence of select oxygen surface groups on the performance of the catalyst.

To address this, carbon black was functionalized by nitic acid at temperatures between 70 and 140°C, before being subjected to heat treatments at different temperatures between 330 and 650°C. A reference support without oxygen on the surface was prepared by subjecting pristine carbon black to a reducing atmosphere at 950°C. Pre-synthesized cobalt oxide nanoparticles were deposited onto the carbon black after support functionalization. The properties of the catalysts were determined by Raman spectroscopy, nitrogen adsorption-desorption, temperature programmed desorption (TPD), X-ray photoelectron spectroscopy (XPS), scanning transmission electron microscopy (S(T)EM), Microwave Plasma Atomic Emission Spectroscopy (MP-AES), X-ray diffraction (XRD), and temperature programmed reduction (TPR). Activity, selectivity, and stability were evaluated by catalytic tests at FT conditions with p = 20 bar, $H_2/CO = 2.1$, and temperatures between 220 and 240°C. The catalytic testing revealed that there were significant differences in the behavior of the catalysts, both during reduction and FT reaction.

TPD and XPS measurements indicated that the selective oxidation had been successful. Overall, the catalyst on the oxidized support that had not been subjected to any heat treatments exhibited the highest cobalt time yield (CTY), while the lowest performance was seen for the catalyst on the reference support. Interestingly, the catalyst with non-functionalized support showed the highest site time yield (STY) out of all the catalysts. The main deactivation mechanisms observed were sintering and presumably re-oxidation of the metal particles. The catalysts with functionalized supports sintered less than the reference, which is in line with earlier observations of oxygen groups acting as anchoring

sites. The lowest particle growth was observed on the catalyst support that had not been subjected to a heat treatment, indicating that carboxylic acid groups are especially important for metal immobilization.

Sammendrag

Kobolt katalysert Fischer-Tropsch (FT) er en måte å produsere syntetisk drivstoff og kjemikalier fra bærekraftig råmateriale, slik som biomasse og ikke-resirkulerbar plastavfall. Vanlige bæremateriale for FT katalysatorer er blant annet aluminiumoksid og silisiumoksid [1, 2]. Disse materialene interagerer imidlertid med metallet og danner inaktive faser som det ikke er mulig å redusere som $CoAl_2O_4$ og $CoSiO_4$ [3]. Karbon innehar mange av de samme egenskapene som de overnevnte materialene, men interagerer ikke like sterkt med metallpartiklene [4, 5]. På grunn av de svake metall-bærer interaksjonene kan det være utfordrende å oppnå god dispersjon, og en betydelig sintring av koboltpartikler på ikke-funksjonalisert karbon har blitt observert. Man kan redusere disse utfordringene ved å introdusere oksygen til overflaten av karbonet. De funksjonelle gruppene forventes å virke som ankringspunkter, og immobilisere metallpartiklene. Til tross for at det er blitt gjort mye forskning på oksidert karbon som bærer for kobolt katalysert FT syntese har det blitt lagt lite vekt på selektiv oksygen funksjonalisering for å undersøke effekten av enkelte oksygen gruppers innflytelse på ytelsen til katalysatoren.

For å undersøke dette ble karbon oksidert med salpetersyre ved temperaturer mellom 70 og 140°C, før karbonet ble varmebehandlet ved ulike temperaturer mellom 330 og 650°C. En bærer ble laget som referanse ved å varmebehandle karbon i en reduserende atmosfære ved 950°C. Nanopartikler av koboltoksid ble deponert på karbonet etter funksjonalisering. Egenskapene til katalysatoren ble kartlagt med Raman spektroskopi, nitrogen adsorpsjon-desorpsjon, temperaturprogrammert desorpsjon (TPD), røntgenfotoelektronspektroskopi (XPS), sveiptransmisjonselektronmikroskopi (S(T)EM), mikrobølge plasma atomemisjonsspektroskopi (MP-AES), røntgenkrystallografi (XRD), og temperaturprogrammert reduksjon (TPR). Aktivitet, selektivitet og stabilitet ble evaluert ved å teste katalysatoren under FT forhold med p = 20 bar, $H_2/CO = 2.1$, og temperaturer mellom 220 og 240°C. Det ble observert betydelige forskjeller mellom ytelsen til katalysatorene både ved redusering og reaksjon.

TPD og XPS målinger viser at den selektive oksideringen var vellykket. Katalysatoren med oksidert bærer som ikke hadde blitt utsatt for varmebehandling, Co/CB-70, viste høyest CTY, mens den laveste omdanningen av CO ble målt av katalysatoren uten oksygengrupper på bæreren, Co/CB-H, hadde høyest STY av alle katalysatorene. De dominerende deaktiveringsmekanismene var sintring og formodentlig re-oksidering av metallpartiklene. Katalysatorene med oksidert bærer sintret mindre enn referansekatalysatoren. Partikkelveksten var lavest på katalysatoren som hadde en oksidert bærer, men som ikke hadde blitt utsatt for varmebehandling. Dette indikerer at karboksylsyregrupper har en sentral rolle i immobiliseringen av metallpartikler.

Contents

List of Figures **ix**

List of Tables **xii**

1 Introduction **1**

2 Literature Review **3**

2.1 Carbon black as support for FT catalysts 3

2.1.1 Oxidation of carbon support materials 4

2.1.2 Surface reactions and identification of oxygen groups 6

2.1.3 Heat treatment of oxidized carbon 9

2.2 Catalytic performance of carbon-supported cobalt catalysts 10

2.2.1 Activity 10

2.2.2 Selectivity 15

2.2.3 Deactivation 20

3 Theory **24**

3.1 Catalyst preparation 24

3.1.1 Oxidation with nitric acid 24

3.1.2 Thermal desorption 24

3.1.3 Colloidal cobalt nanoparticle synthesis 25

3.1.4 Loading of pre-prepared nanoparticles 25

3.2 Characterization 25

3.2.1 BET 25

3.2.2 XPS 26

3.2.3 XRD . . . 27
3.2.4 TPD . . . 28
3.2.5 TPR . . . 28
3.2.6 Raman spectroscopy . . . 28
3.2.7 S(T)EM . . . 29
3.2.8 MP-AES . . . 29
3.2.9 Gas Chromatography . . . 30

4 Methods **31**

4.1 Catalyst preparation . . . 31
4.1.1 Oxidation of carbon black . . . 31
4.1.2 Heat treatments . . . 31
4.1.3 CoO nanoparticle synthesis . . . 32
4.1.4 Nanoparticle deposition . . . 33
4.2 Catalytic testing . . . 33
4.2.1 Reduction . . . 33
4.2.2 Fischer-Tropsch synthesis . . . 34
4.3 Characterization . . . 35
4.3.1 Nitrogen adsorption-desorption . . . 35
4.3.2 Raman . . . 35
4.3.3 XPS . . . 35
4.3.4 XRD . . . 35
4.3.5 S(T)EM . . . 35
4.3.6 TPR . . . 36
4.3.7 MP-AES . . . 36
4.3.8 TPD . . . 36

5 Results and Discussion **37**

5.1 Support . . . 37
5.1.1 Structure and textural properties . . . 38
5.1.2 Oxygen functionalization . . . 41

5.2 Fresh catalyst . . . 48
5.3 Reduced catalyst . . . 50
5.4 Catalytic testing . . . 53
5.4.1 Co/CB-H . . . 55
5.4.2 Co/CB-70 . . . 56
5.4.3 Co/CB-95-H330 . . . 56
5.4.4 Co/CB-120-H530 . . . 57
5.4.5 Co/CB-140-H650 . . . 58
5.5 Spent catalyst . . . 58

6 Conclusion **60**

7 Further work **62**

A TPD **74**
A.1 Quantification of TPD data . . . 74
A.1.1 Fitting of TPD curves . . . 74

B XPS **76**
B.1 Fitting of XPS data . . . 76
B.1.1 C 1s orbital . . . 76
B.1.2 O 1s orbital . . . 76
B.1.3 XPS spectra . . . 76

C Raman spectroscopy **79**
C.1 Deconvolution of Raman spectra . . . 79
C.2 Crystallinity parameters . . . 79

D Nitrogen adsorption-desorption **80**
D.1 Sample weight . . . 80
D.2 Physisorption isotherms . . . 80

E Particle size distributions **82**

F MP-AES **84**

G TPR **85**

G.1 Sample weight 85

G.2 TPR measurements 85

H Catalytic testing **87**

H.1 Activity calculations 87

H.1.1 CO conversion 87

H.2 Selectiviy calculations 88

I P&ID **89**

List of Figures

2.1 High-resolution TEM images of carbon black. (a) Shows a closeup of the carbon layers that makes up the carbon black primary particles. (b) Shows how the particles agglomerate to form larger structures. Macropores are formed between the agglomerated carbon primary particles. From [20]. . . . 4

2.2 Illustration of oxygen functional groups at the surface of oxidized carbon. . 7

2.3 Illustration of the two types of lactones found on typical edge configuration in carbon. Lactones on zigzag edges have a higher ring strain and therefore decompose more easily. 8

2.4 TPD and TPR profiles of MWCNTs functionalized with nitrosulfuric acid. The top row shows a linear temperature program, while the bottom row displays the results from isothermal heating. The colored areas draw attention to the differences between the signal in inert and reducing atmosphere [44] 9

2.5 Calculated potential energy for CO activation at the transition states for breaking the C=O bond via a direct and H-assisted route. The figure shows both hcp (A) and fcc (B) facets. CO + 1/2 H_2 in gas phase was used for the zero energy reference. Modified from [53] 11

2.6 (a) Evolution of volume ratio $V_{\alpha/\beta}$ as a function of annealing temperature. α denotes the hcp phase, while β is the fcc structure. The cobalt particle diameter was 30nm [57]. (b) TPR-XRPD of a Co/CNF catalyst. The graphs show the successive reduction of Co_3O_4 to CoO and further to metallic cobalt in the phases hcp Co and fcc Co. A and B denote large and small Co_3O_4 crystallites respectively, as the particles studied had a bimodal particle size distribution [58]. 12

2.7 (a) Activity (CTY) as a function of Co particle size. (b) TOF as a function of particle size. T = 220°C, H_2/CO = 2, p = 1bar. From [59] 13

2.8 Depiction of the selectivity to different chain lengths changes with the chain growth probability, α. From [72]. 16

2.9 A schematic illustration of hydrogen spillover on carbon-supported cobalt particles. 17

2.10 (a) Methane selectivity as a function of Co particle size. (b) Octane/octene ratio as a function of particle size. (a) and (b) T = 220°C, $H_2/CO = 2$, p = 1bar. Modified from [59] (C) Hydrogen coverage as a function of particle size. T = 210°C, $H_2/CO = 10$, p = 1.85 bar. From [60]. 19

2.11 The two main sintering mechanisms (a) coalescence and (b) Ostwald ripening 21

3.1 X-rays scattering by atoms in a periodic lattice. d is the space between the lattice planes and θ is the angle between the incoming X-rays and the normal to the reflecting plane. Adapted from [95]. 27

3.2 Raman and Rayleigh scattering. m is the ground vibrational state and n is an excited vibrational state. From [98]. 29

4.1 Schematic illustration of the synthesis of CoO nanoparticles through the hot injection method. From [14] 33

4.2 Simplified illustration of the setup used for catalytic testing. The full PID can be found in Appendix I 34

5.1 Schematic illustration of oxygen functional groups being eliminated from the carbon surface during heat treatments. 38

5.2 Nitrogen adsorption-desorption isotherms showing the different isotherm profiles between (a) CB-H and (b) CB-140-H650. 39

5.3 STEM micrographs showing the difference in structure of (a) CB-H and (b) CB-140-H650. 39

5.4 Raman spectrum of CB-H 40

5.5 (a) HWHM of the G peak, (b) ID/IG ratio, and (c) G peak position for all the catalyst supports. 40

5.6 Mass loss curves from the TGA. The dashed lines indicate the heat treatment temperatures. 42

5.7 CO and CO_2 emissions from CB-70. 43

5.8 (a) CO and (b) CO_2 emissions for each oxidized support material. CB-H is not included here, as there were no detectable emissions from this sample. . 44

5.9 Deconvoluted TPD signals from CO and CO_2 emissions. 45

5.10 Quantification of (a) CO and (b) CO_2 emitting groups from the deconvolution of the TPD data from all the oxidized supports. 46

5.11 (a) Deconvoluted C 1s orbital. (b) Deconvoluted O 1s orbital. 47

5.12 Quantification of the bonds in the (a) C 1s orbital, and (b) O 1s orbital. . . 47

5.13 (a) STEM micrograph of the cobalt nanoparticles before deposition. The STEM image was taken with an accelerating voltage of 30kV, and an emission current of 10μA. (b) The particle size distribution of the particles before deposition onto the support material. From [14]. 48

5.14 STEM micrograph showing the cobalt nanoparticles deposited on carbon black for Co/CB-70. The STEM image was taken with an accelerating voltage of 30kV, and an emission current of 10μA. 49

5.15 XRD measurements of the fresh catalysts. ($\diamond$) CoO 50

5.16 TPR profiles of the catalysts. 51

5.17 X-ray diffractograms of the reduced catalysts. ($\diamond$) CoO, ($\circ$) hcp Co ^{0}. . . . 53

5.18 Cobalt time yield from the activity testing of the catalysts. The dashed lines show when the temperature was changed. p = 20 bar, $p_{H_2}/p_{CO} = 2$. . 53

5.19 (a) Initial site time yield compared to the initial degree of reduction calculated from TPR measurements. (b) Loss in activity compared to the loss in surface area for all catalysts. 55

5.20 (a) XRD measurements of the spent catalysts. ($\circ$) hcp cobalt, ($\square$) fcc cobalt.(b) The mean particle size of the fresh, reduced, and spent catalysts. 58

B.1 Deconvoluted C 1s orbital. 77

B.2 Deconvoluted O 1s orbital 78

D.1 N_2 physisorption isotherms for all catalyst supports 81

E.1 Particle size distribution for fresh, reduced and spent catalyst Co/CB-H . . 82

E.2 Particle size distribution for fresh, reduced and spent catalyst Co/CB-70 . . 82

E.3 Particle size distribution for fresh, reduced and spent catalyst Co/CB-95-H330 83

E.4 Particle size distribution for fresh, reduced and spent catalyst Co/CB-120-H530 83

E.5 Particle size distribution for fresh, reduced and spent catalyst Co/CB-140-H650 83

G.1 TPR measurements for all the catalysts 86

List of Tables

4.1 Acid and heat treatment temperatures of the catalyst support materials. . . 32

5.1 The specific surface area of the support materials measured by nitrogen adsorption-desorption. CB denote untreated carbon black. 38

5.2 The mass loss from TGA measurements and surface oxygen content from XPS measurements for all support materials. 41

5.3 The cobalt loading and average particle size of the fresh catalyst. 50

5.4 Reduction data from TPR studies. The reduction temperature was taken to be the temperature at the peak maximum. 52

5.5 Mean diameter of cobalt particles on the reduced catalysts, and the difference in particle size between the fresh and the reduced catalyst. 52

5.6 Summary of activity and selectivity data from the FT synthesis experiments. X_{CO} Denotes the CO conversion where the selectivities were measured, at 77 h on stream. STY is the site time yield, and the subscripts i and f denotes *initial* and *final* respectively corresponding to 0 and 112 h on stream. 54

5.7 The loss in surface area and conversion of all the catalysts. 54

C.1 Ratio between D and G peak, position of the G peak, and half width at half maximum for the G peak for all the catalyst supports. 79

D.1 Weight of measured sample used to find the specific surface area of the catalyst suppors 80

F.1 Weight of the samples used for MP-AES to determine cobalt loading. 84

G.1 Weight of measured sample used for TPR. Both a linear temperature program, and a reduction program mimicking the reduction the catalyst is subjected to prior to synthesis. 85

Chapter 1

Introduction

In 2015 196 countries signed the Paris Agreement committing to "pursue efforts to limit the global temperature increase to 1.5°C above pre-industrial levels" [6]. Global warming is linked to human activity after the industrial revolution, which has been heavily reliant on fossil energy sources [7]. The temperature has already increased by 1.1°C, and the effects of climate change are starting to show. Increased occurrence of extreme weather conditions such as heat waves, droughts, and tropical cyclones are some of the consequences of an increased global temperature. The key to halting this development is to replace fossil energy sources with sustainable energy production and storage. Most of the global greenhouse gas emissions come from using fossil fuels as energy sources for electricity, heat, and transport [8]. In addition, direct emissions from the chemical industry purely related to production and not energy consumption are 2.2% of the total global greenhouse gas emissions. These data show that there is a large potential to mitigate emissions both in the energy sector and in the chemical industry.

Finding new energy sources and new ways to produce chemicals that are climate-neutral or climate-positive is a huge challenge. There has been an increased focus on renewable energy sources in recent years, but the issue of energy storage has not been solved satisfactorily. Many sustainable energy sources only produce energy intermittently, typical examples of this are solar and wind power. To harness these intermittent energy sources it is important to have a reliable energy storage system in place. Lithium-ion batteries have become the first choice for many applications such as small electric appliances and passenger cars. These batteries do however generally not have a high enough energy density to power units that require a high degree of energy over extended time periods, such as planes and cargo ships. Some argue that hydrogen can be used as an energy carrier in these situations, but there are concerns about the storage and safety of hydrogen that have still not been resolved. Synthetic fuel made from biomass, captured CO_2, or other carbonaceous feedstocks are a viable alternative for these hard-to-albeit sectors. By gasifying carbonaceous waste streams such as municipal waste and non-recyclable plastic, or by using the reverse water gas shift reaction to produce CO from captured CO_2, it is possible to valorize waste and emissions that would otherwise not be exploited by using the Fischer-Tropsch synthesis. Not only does this have the potential to mitigate emissions from the energy sector and the chemical industry, but it is a viable way to close the carbon circle. Waste and emission reduction is one of the pillars of green chemistry [9]. It is

however not plausible that it will be possible to avoid producing waste and CO_2 emissions completely. Using these carbon sources to produce synthetic fuels and other chemicals instead of fossil resources is a good alternative to CO_2 sequestration and landfills.

FT synthesis converts synthesis gas (CO and H_2) to various-length hydrocarbons. The products can be processed further into fuels or platform chemicals that are used in the production of rubbers, surfactants, fibers, etc. [3, 10, 11]. The most active metals for FT synthesis are cobalt, iron, and ruthenium[11]. Nickle also produces FT products but is more active for methanation than desired [12]. Because of the high cost associated with ruthenium, it is not relevant in an industrial context. Iron is widely employed as a catalyst for FT synthesis, but it has a higher activity for the water gas shift reaction than cobalt, and cobalt is more active at lower temperatures[11]. Several metals such as platinum, palladium, and rhenium have been employed as promoters to enhance the reduction of the metal active site[11, 12].

As cobalt is an expensive metal, it is desirable to maximize the active sites by dispersing the cobalt onto a high surface area support material. This allows for cobalt nanoparticles which have a high surface area to volume ratio to form on the surface. Typical support materials are Al_2O_3, SiO_2, and TiO_2[12]. However, these tend to interact strongly with the metal phase and form unreducible and nonactive phases such as $CoAl_2O_4$ [3]. As an alternative, it is possible to use carbon as support. Carbon is relatively inert in this context and does not interact strongly with the metal. This is however not entirely nonproblematic. The low interaction with the support facilitates sintering of the particles which deactivates the catalyst. The metal-support interactions can be modified by introducing heteroatoms such as oxygen to the surface. Oxygen groups act as anchoring sites on the surface and immobilize the metal particles.

Scope of this work

The aim of this thesis was to investigate the effects of a selectively oxygen-functionalized carbon support material for cobalt-catalyzed FT synthesis. Oxidation with nitric acid followed by heat treatments was used to create carbon black surfaces with tunable surface chemistry. Pre-synthesized nanoparticles were prepared based on the work of van Deelen et al.[13] as part of the specialization project prior to starting the thesis [14]. The nanoparticles were deposited on the modified carbon black and the catalyst was tested under FT conditions. The surface chemistry of the carbon black was characterized with TPD and XPS. The structural and textural properties of the support were determined with Raman spectroscopy and N_2 physisorption. The cobalt loading was determined with MP-AES and the particle size distributions were found manually by measuring the particles from DF-STEM images. The oxidation state and crystallographic phase of the cobalt were investigated using XRD. Reduction temperatures and degree of reduction were found with TPR. The catalysts were tested in a tubular fixed bed reactor at 20 bar and an H_2/CO ratio of 2.1. The temperature varied between 220 and 240°C during the time on stream.

Chapter 2

Literature Review

The literature review is intended to shed light on the properties of carbon black and how they can be modified by introducing oxygen functional groups to the surface. Defunctionalization through thermal desorption will be highlighted as a method to tune the surface chemistry, and the role of temperature programmed desorption (TPD) in the identification of surface species will be discussed. Catalytic performance will be discussed in terms of three performance indicators, namely activity, selectivity, and stability of the catalyst. The influence of different parameters on the performance will be covered with a focus on oxygen functionalized carbon supported cobalt catalysts.

2.1 Carbon black as support for FT catalysts

Carbon exhibits many of the desired properties of a catalyst support material[4]. Among other characteristics, high surface area and thermal stability are important for their use as support. In addition, pristine carbon is relatively inert, which makes it attractive for use in FT synthesis, as it does not form unreducible phases with the metal, such as alumina and other common support materials [10]. Activated carbon and carbon black are the two most used carbons in catalysis, although nanocarbons such as carbon nanotubes (CNTs) and nanofibres (CNFs) are also gaining interest [5, 15]. Carbon black typically has a smaller surface area than activated carbon as the primary particles are not intrinsically porous. The pore structure is instead formed between agglomerates of carbon black particles.

The pore structure of the support influences the performance of the catalyst by dictating the metal particle size and diffusion of species inside the pores when using impregnation and calcination methods for metal loading [15]. Fu et al. [16] used CNTs and activated carbon with different pore sizes to study the effect of porosity on the performance of cobalt catalysts for FT synthesis. They found that CNFs with larger pore sizes resulted in better selectivity towards C5+ products and higher activity compared to the activated carbon with a pore size of around 1 nm. As the average pore diameter was smaller than the mean particle size, most of the particles were located outside the pores, decreasing the area of carbon available for metal particles. Larger pore structures also facilitate the diffusion of reactants to the active sites. The macroporous structure that carbon black provides is

therefore beneficial to study carbon-supported cobalt catalysts for FT synthesis.

Carbon black is produced through the incomplete combustion of hydrocarbons, either in the form of tar, lighter liquid hydrocarbons, or gaseous hydrocarbons [17, 18]. Depending on the amount of air available during synthesis there are two types of carbon black, furnace black and acetylene black, where acetylene black is prepared in the absence of oxygen. Furnace blacks are known to be easier to oxidize than acetylene black [19].

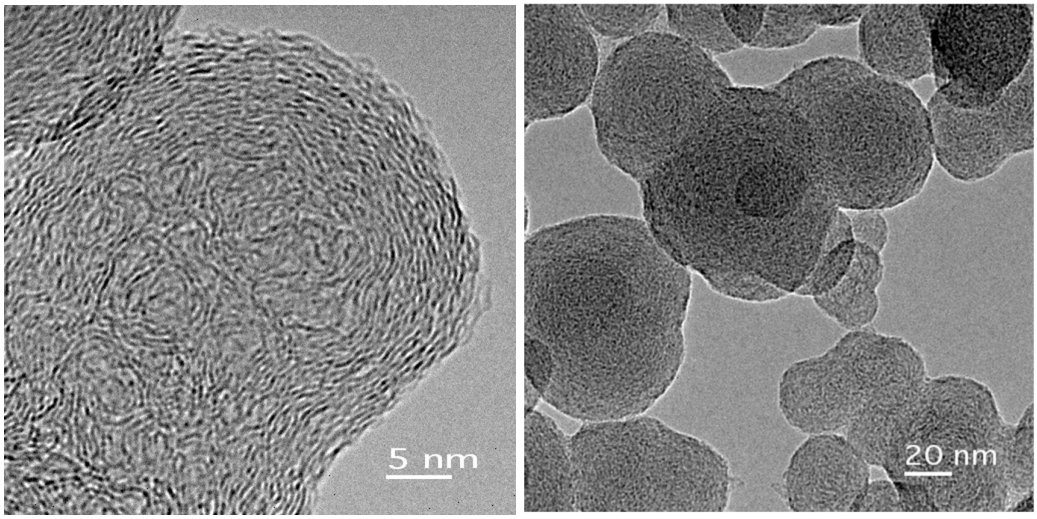

(a) **(b)**

Figure 2.1: High-resolution TEM images of carbon black. (a) Shows a closeup of the carbon layers that makes up the carbon black primary particles. (b) Shows how the particles agglomerate to form larger structures. Macropores are formed between the agglomerated carbon primary particles. From [20].

Figure 2.1 shows a high-resolution TEM picture of the internal structure of carbon black. The carbon layers are visible in the micrograph, and they are arranged in an onion-like formation, with the internal structure being more amorphous while the outer layers exhibit a more ordered graphite-like crystalline structure [21]. Carbon black is a 0D carbon nanomaterial, meaning all dimensions of the carbon black particle are in the nanoscale[5]. The particles are made up of sp^2-hybridized carbon planes connected in a paracrystalline structure, and the particles agglomerate to create larger carbon structures with meso and macropores [22, 23].

2.1.1 Oxidation of carbon support materials

The chemical properties of carbon can be changed by introducing heteroatoms to the surface, and examples of common dopants are oxygen, nitrogen, sulfur, and boron [24]. By causing charge delocalization and introducing defects caused by differences in coordination number, bond length, and atomic radius, the heteroatoms embedded in the carbon matrix can provide active sites on the carbon and promote charge transfer to reactants, thus exhibiting catalytic activity without the presence of metals for certain reactions [25]. One of the most common and useful ways of altering the surface chemistry of carbon support materials for catalysis is through the functionalization with oxygen groups. In this

instance, the oxygen is not commonly embedded in the carbon matrix but forms functional groups on the surface or the edges of basal planes[26]. The oxygen alters some of the properties of the carbon, such as improving hydrophilicity [4, 27, 28]. This could aid in the preparation of catalysts by improving wettability during impregnation with polar media, as well as improve interactions between the support and the metal cations used for impregnation[29, 2]. It is also well known that oxygen surface groups act as anchoring sites for metal nanoparticles, which is believed to prevent sintering and facilitate better dispersion of metal on the carbon surface [2, 3, 30]. Oxygen functionalization of carbon materials is therefore an attractive way of modifying carbon for use as support in catalysis.

Adsorption of heteroatoms on the carbon surface of an sp^2 hybridized carbon is mainly dictated by edge carbon atoms and point-defects, meaning structural carbon vacancies and nonaromatic rings[5]. These sites are more reactive because of the unpaired electrons that are localized there. Depending on the nature of the treatment, oxidation can also introduce new defects, and change the morphology of the carbon. Oxidation treatments are commonly used to break open CNTs and to introduce defects on the carbon surface [31]. This not only facilitates metal immobilization but also provides lower internal mass transfer limitations by opening the pore structure [32]. It is therefore important to choose a suitable oxidation treatment that facilitates the degree of oxidation required, and takes into account potential structural damage as a consequence of oxidation.

There are several ways to introduce oxygen groups to a carbon surface. The oxidation can take place in gaseous or liquid phase, and some of the oxidation agents reported in literature are ozone, air, oxygen plasma, hydrogen peroxide, sulfuric acid, and nitric acid [3, 30, 33]. Datsyuk et al.[34] investigated the effect of different oxidation treatments on the structure and surface chemistry of multiwalled carbon nanotubes (MWCNTs). Both acidic and basic oxidation agents were employed, using refluxed nitric acid, a mixture of ammonium hydroxide and hydrogen peroxide, and a mixture of sulphuric acid and hydrogen peroxide (piranha solution). A reference material was prepared by treating the MWCNTs in hydrochloric acid to remove impurities and oxygen groups on the surface present from the synthesis of the nanotubes. The oxidation treatments increased the amount of surface oxygen in the order nitric acid > piranha > ammonium hydroxide/hydrogen peroxide. While the two latter treatments did not lead to additional defects in the carbon structure compared to the HCl-treated sample, the nitric acid caused a significant increase in defect sites, in addition to shortening the nanotubes. Nitric acid was therefore deemed the most invasive oxidation agent of the ones listed above.

Although nitric acid partially destroys the carbon structure, it can be used to investigate differences in the oxidation of carbons. The harsh treatment provided by nitric acid was taken advantage of by Kamegawa et al.[19] as they looked into the effect of oxidation on the two types of carbon black, namely furnace black and acetylene black. The carbon was oxidized at 100°C with nitric acid. After the oxidation treatment, the carbon was separated by molecular weight. The carbon had decomposed to fractions of carbon planes with oxygen functional groups at the edges as a consequence of the harsh treatment. This allowed them to study the differences in oxidation time and of the two types of carbon black on the degree of oxidation as well as the change in the structural integrity of the materials. They observed that the elemental composition of the carbon fractions stayed almost constant regardless of the oxidation time for the furnace black except for the

fraction with the largest particles, but the yield of smaller-sized fractions increased with oxidation time. The acetylene black mainly consisted of the fraction with the heaviest compounds, even after 1000 h of oxidation. This indicates that even with harsh oxidation treatment, the acetylene black structure did not break into fractions. The oxidation time does not seem to influence the degree of oxidation significantly, but the length of the acid treatment was important to the structural integrity of the material. Using nitric acid for shorter time periods could be a way of introducing a high degree of oxygen groups, while still keeping the structural changes in the carbon low.

Kamegava et al.[19] are not alone in observing a significant change in the carbon after oxidation with acid treatments [34, 3]. Especially at elevated temperatures the acid degrades the carbon structure. Shi et al.[21] used the invasive nature of the nitric acid treatment to hollow out carbon black particles for use in lithium-ion batteries, while Tang et al.[35] observed that an increased oxidation time progressively changed the structure of the carbon black particles to become hollow at the center. The carbon close to the center of the carbon black particles is more curved than close to the perimeter. The increased curvature in the carbonaceous structure leads to an increased reactivity and the center is therefore more easily oxidized [36].

2.1.2 Surface reactions and identification of oxygen groups

The oxidation treatments introduce oxygen functional groups to the surface of the carbon, but identification of these groups can be challenging. Figure 2.2 shows a schematic presentation of the groups that are formed on an oxidized carbon structure. Possible methods used to assess the surface chemistry include Diffuse Reflectance Fourier Transform Spectroscopy (DRIFTS), acid-base titration, point of zero charge (PZC) analysis, X-ray photoelectron spectroscopy (XPS), Nuclear Magnetic Resonance (NMR) spectroscopy and temperature programmed desorption (TPD) [19, 30, 37, 38, 39, 40].

None of the aforementioned analysis tools are suitable as a stand-alone method to accurately determine the composition of oxygen surface groups. DRIFTS can give an accurate depiction of the surface chemistry, but the interpretation of the spectra is difficult as the nature of the carbon causes a low signal-to-noise ratio, and the overlap of contributions to the bands makes it difficult to distinguish the various functional groups [41, 30]. Acid-base titration and PZC analysis is a good way to determine the acid-base properties of the surface, but it does not give information on neutral groups. XPS provides information about the surface of the sample but does not probe functional groups that are located inside pore structures. Distinguishing between groups with similar bond structures is also a challenge. Although XPS only assesses the surface layer of the sample, it is possible to use the data for quantification of surface species. TPD measurements might be the most useful characterization method for analyzing functionalized carbon. During heating the oxygen functional groups decompose as CO and CO_2 depending on the nature of the group. TPD can therefore also be used for quantification, by measuring the concentration of carbon oxides emitted at different temperatures. However, since the data is collected at an increasing temperature, the surface groups detected might not be entirely representative of the surface at room temperature. Surface reactions between functional groups take place at elevated temperatures changing the surface chemistry, and the signals from the

desorbing groups overlap making it challenging to accurately determine the concentration of different groups before heat treatment. TPD also gives information about the desorption temperatures of the different groups and by studying TPD data one can anticipate the surface reactions that take place during defunctionalization by heating.

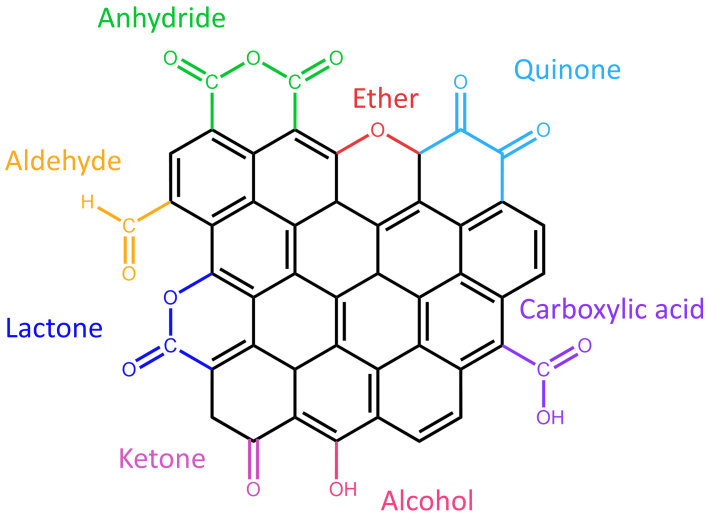

Figure 2.2: Illustration of oxygen functional groups at the surface of oxidized carbon.

Surface reactions between oxygen groups were investigated by Göckeler et al.[42] using TPD measurements. Carbon black was functionalized with nitric acid at 150°C for 2 h, 4 h, 6 h, and 24 h. A correlation between the number of carboxylic acid groups and water emitted from the carbon surface is reported. Water coordinated to carboxylic acid groups at ambient conditions is proposed as a possible explanation for the correlation in emissions. Water is also presumably released through condensation reactions between neighboring alcohol and carboxylic acid groups, as the released water also scales with the sum of released anhydrides and lactones. This indicates that parts of these groups were formed during TPD and that the hydrolyzed form is present at ambient conditions. Temperature programmed reduction (TPR) measurements also revealed some interesting behaviors at elevated temperatures in a hydrogen atmosphere. Carbonyls and quinones are reduced to phenols, which are further reduced to aromatics leading to a release of water in two steps. It was also observed that more CO_2 was released compared to the TPD measurement, although the total oxygen released was the same for both TPD and TPR. It is therefore likely that H_2O produced during reduction reacts with the surface groups. Hydrolysis of carboxylic anhydrides to two carboxylic acid groups or armchair lactones that react with water to form carboxylic acid and phenol groups could be part of the explanation of why an elevated CO_2 signal was observed. This gives insight into both how surface groups behave during heating, as well as reduction at elevated temperatures, two common processes in the preparation of catalysts and during FT synthesis.

Hall and Calo [43] also studied the secondary surface reactions that take place during TPD on oxidized char samples, taking an extra interest in how surface species interact with gaseous species emitted during heating. The char was oxidized with a flow of oxygen before being exposed to CO to induce a higher concentration of gaseous CO in the pores than would be present just from heating. Char that had been loaded with CO released

more CO_2 at lower temperatures (300-800K). This increase was not observed for an unoxidized char with CO treatment, indicating that CO reacts with surface groups causing the development of CO_2 during the following TPD. Not only does CO react with surface groups, but experiments done on unoxidized carbon treated with CO also emitted CO at high temperatures, indicating that the CO adsorbs to the surface of the carbons during the initial exposure at 200°C. It is therefore likely that CO developed during the heat treatment can re-chemisorb to the surface, although to which extent this is relevant is difficult to determine. The CO readsorption mechanism depends on the structure and porosity of the carbon as well as a number of other factors. Even though it is not easy to pinpoint exactly the cause of the gas emissions that are detected during TPD, the study shows that interaction between surface groups and desorbed CO could take place, changing the surface chemistry at elevated temperatures.

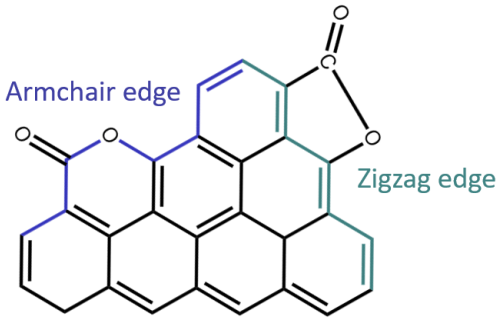

Figure 2.3: Illustration of the two types of lactones found on typical edge configuration in carbon. Lactones on zigzag edges have a higher ring strain and therefore decompose more easily.

In addition to surface reactions, there are more challenges associated with TPD measurements. The most common way of setting up a TPD measurement is by using a linear temperature ramp. This can however make it difficult to separate which functional group gives rise to the CO and CO_2 emissions as a consequence of overlapping desorption ranges for different species. Düngen et al.[44] proposed using non-linear TPD measurements to aid in the separation of signals arising from various oxygen functional groups on the surface of MWCNTs. Overlapping of signals that arise during TPD can prevent the differentiation of certain functional groups that have similar desorption temperatures. The objective of a stepwise temperature increase during analysis would be to complete each desorption process prior to increasing the temperature further. The desorption temperature of a certain oxygen group on the surface does not just depend on the nature of the group, but also on the chemical environment that it is in [38]. For example would lactones found on zig-zag edges and armchair edges have different desorption temperatures. Lactones in a zig-zag configuration have been found to decompose at lower temperatures because of the difference in ring-strain as shown in Figure 2.3 [45, 44]. Assuming a random distribution of binding energies of each functional group, this can be modeled using a Gaussian curve. Some groups are however not possible to separate in this way as the decomposition temperature overlap too severely. Figure 2.4 shows the difference between using a linear heating program and a program with isothermal steps. The key to a successful stepwise TPD is choosing the optimal temperature program. This can be done by first using linear

TPD to approximate the desorption temperatures of the different functional groups, and subsequently using this data to determine the isothermal steps. Düngen et al. [44] argue that peak symmetry validates a successful temporal separation of oxygen species.

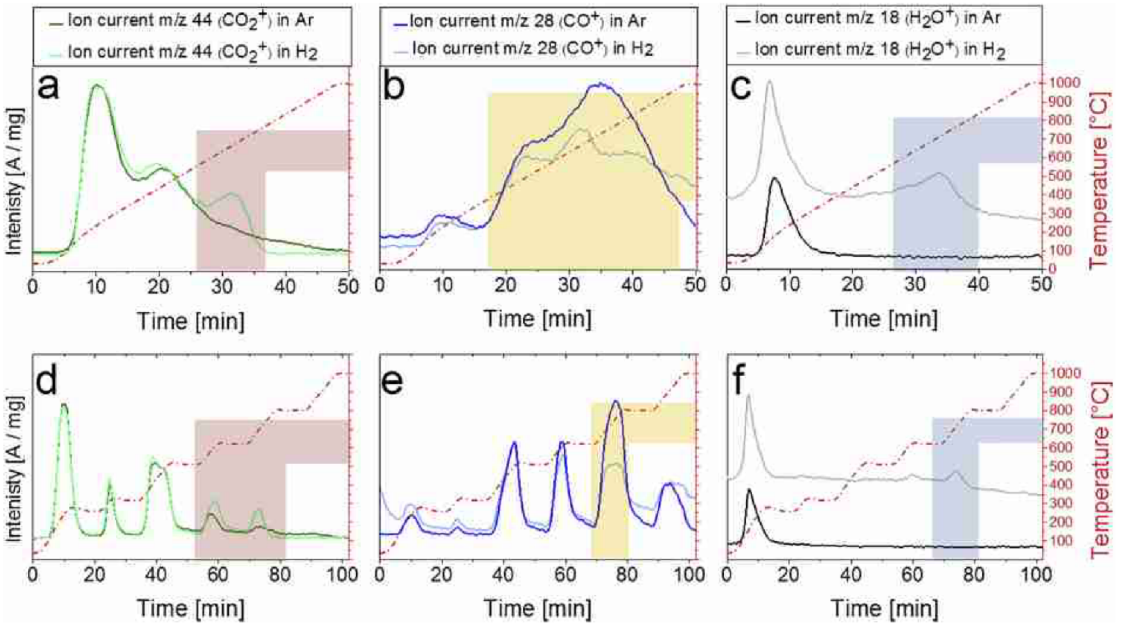

Figure 2.4: TPD and TPR profiles of MWCNTs functionalized with nitrosulfuric acid. The top row shows a linear temperature program, while the bottom row displays the results from isothermal heating. The colored areas draw attention to the differences between the signal in inert and reducing atmosphere [44]

.

2.1.3 Heat treatment of oxidized carbon

TPD measurements are not only useful to identify oxygen functional groups, but it also gives valuable information on the possibilities of altering the surface chemistry by thermal desorption. The functional groups have distinct chemical characteristics, therefore a change in the relative concentration of the different groups would lead to altered properties in the carbon. Tuning the surface chemistry of carbon is challenging, as there is currently no way of selectively oxidizing the material directly. There are however post-oxidation treatments that can alter the surface group distribution[39]. Using TPD measurements as a guide to determine heat treatment temperatures for successive desorption of surface groups, is a viable way to remove oxygen somewhat controlled from the carbon.

Zhuang et al.[46] used heat treatments at 823 K, 873 K, 923 K, 973 K, and 1023 K to thermally desorb certain functional groups from the surface. The heat treatments resulted in a shift in the peak maxima indicating that groups with desorption temperatures lower than the heat treatment temperature were successfully removed from the surface. There were however CO_2 emissions detected at around 573 K for every sample, regardless of heat treatment temperature. This could be caused by the re-adsorption of oxygen from the air at ambient temperatures after heat treatment on the unsaturated carbon sites where the oxygen functional groups were removed. This is a well-known phenomenon studied by Menéndez et al.[47, 48] among others. They looked into the reoxidation behavior of

carbons after heat treatment using both inert and reducing atmospheres during heating. The experiments showed that carbon exposed to H_2 during heating did not re-adsorb oxygen to the same extent as the surface exposed to nitrogen. This seems to be caused by the gasification of the most reactive unsaturated carbon atoms, and the stabilization of the reactive sites left behind after oxygen group decomposition by hydrogen.

TPD studies, as well as the aforementioned papers on thermal desorption of groups, show that it is possible to tune the surface chemistry by first introducing an array of different oxygen functional groups to the surface with oxidation agents such as nitric acid, followed by heat treatments at temperatures settled upon based on data from TPD studies. The resulting carbon surface has a higher concentration of surface groups with decomposition temperatures above the temperature of the heat treatment the surface has been exposed to. Oxygen is likely to readsorb to reactive carbon atoms left behind after heating, but this effect can be minimized by treatment in a hydrogen atmosphere.

2.2 Catalytic performance of carbon-supported cobalt catalysts

A lot of research has been done on the FT reaction after Fischer and Tropsch published their first studies on the topic in the nineteen twenties. As a literature review that details the wealth of knowledge that has been accumulated over the years is beyond the scope of this thesis, a select few topics that are deemed to be essential to the understanding of the catalytic tests presented in the results and discussion part of the thesis is presented here. The articles featured have an emphasis on carbon-supported cobalt catalysts and the influence of oxygen groups on catalytic performance.

2.2.1 Activity

The Fischer-Tropsch reaction is essentially a polymerization reaction where the monomers are created in situ from CO and H_2 and can be characterized by the following steps [49, 50].

- Initiation by CO dissociation and CH_x formation.
- Propagation via C-C coupling reactions
- Termination and desorption of the hydrocarbon chain

The products are aliphatic and olefinic compounds, while by-products include water and CO_2 [51]. Assuming synthesis gas that is free from CO_2, CO is the only source of carbon, and the activity is often measured in terms of CO-conversion (X_{CO}), cobalt time yield (CTY) meaning the CO-conversion per gram cobalt in the reactor, and turnover frequency (TOF) or site time yield (STY), namely the conversion per active site.

There is a lot of discussion on the mechanism of the FT reaction, ranging from how CO dissociates on the cobalt surface, to which part of the reaction is the rate-determining

step[51, 50, 52, 53, 54]. A selection of papers related to the topics of activity are presented here. Details of the discussion on the mechanism of FT synthesis are however not included, as this is not investigated in the experimental part of the thesis.

Influence of crystallographic structure

The active phase of the catalyst is widely accepted as metallic cobalt, although it has been proposed that both cobalt oxides and cobalt carbide participate in the reaction[55, 56]. This however seems to be highly support dependent [49]. The discussion of the active phase is however beyond the scope of this thesis, and from now on the term will exclusively refer to metallic cobalt.

It is however not just the oxidation state of the cobalt that influences the catalyst activity. The structure of the cobalt nanoparticles is also important, as FT synthesis is structure sensitive [49]. This means that the elementary steps of the reaction are dependent on certain active sites with a distinct geometrical configuration. As there are many elementary steps involved in the synthesis, such as CO-dissociation, hydrogenation, and C-C coupling, a variety of active sites might be part of dictating the catalytic behavior. To better understand the structural effects that are at play during the synthesis, there have been numerous studies on the role of metallic cobalt crystallography. Metallic cobalt is found in three phases, face-centered cubic (fcc), hexagonal closed packed (hcp), and cubic primitive (cp) [49]. The two former allotropes are expected to be present for cobalt nanoparticles under FT synthesis conditions.

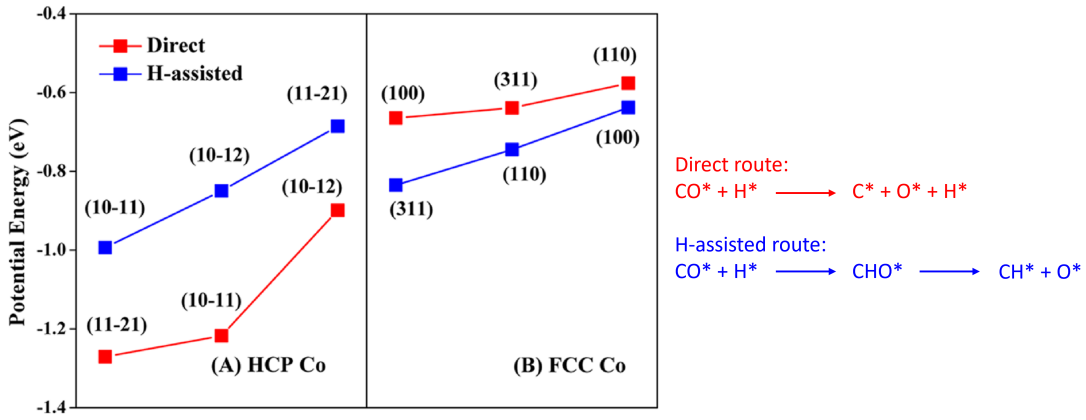

Figure 2.5: Calculated potential energy for CO activation at the transition states for breaking the C=O bond via a direct and H-assisted route. The figure shows both hcp (A) and fcc (B) facets. CO + 1/2 H_2 in gas phase was used for the zero energy reference. Modified from [53]

Lyu et al.[54] compared fcc and hcp single-phase cobalt catalysts for the FT reaction. They identified CO dissociation as the rate-determining step in both catalysts and found that Co in an hcp lattice exhibits higher activity towards hydrocarbon formation. These results are in line with an earlier study by Liu et al.[53] on the effect of hcp versus fcc crystallographic phase on CO activation. Using a first-principle kinetic model they found that CO dissociation on hcp Co follows a direct route, while it proceeds through H-assisted dissociation on fcc Co. As presented in Figure 2.5, the potential energy for CO activation

was found to be lower in the case of direct CO dissociation on hcp Co than the H-assisted route on fcc for all facets explaining why an increased activity is observed for the hcp phase.

Knowing that the hcp phase is more active for FT synthesis than fcc facets, a natural question to ask is which parameters influence the formation of one phase over the other. The topic is well studied, and although the answer is complex, both temperature and crystallite size seems to play an important role [49].

The effect of particle size on the crystal phase of cobalt nanoparticles was investigated by Kitakami et al.[57]. They found that small particles with a diameter under $\sim$ 20 nm display a pure fcc structure, while the hcp structure becomes dominant at a diameter of $\sim$ 40 nm. For FT catalysts the desired cobalt particle size is 6-8 nm, which would suggest a fcc structure in the cobalt, this however is not necessarily the case. Temperature is also important, as the transition from fcc to hcp cobalt is temperature dependent. This was also investigated during the study by annealing the cobalt particles. Figure 2.6a shows the evolution of the volume ratio between the hcp and the fcc phase. At higher temperatures the hcp phase is completely transformed to fcc.

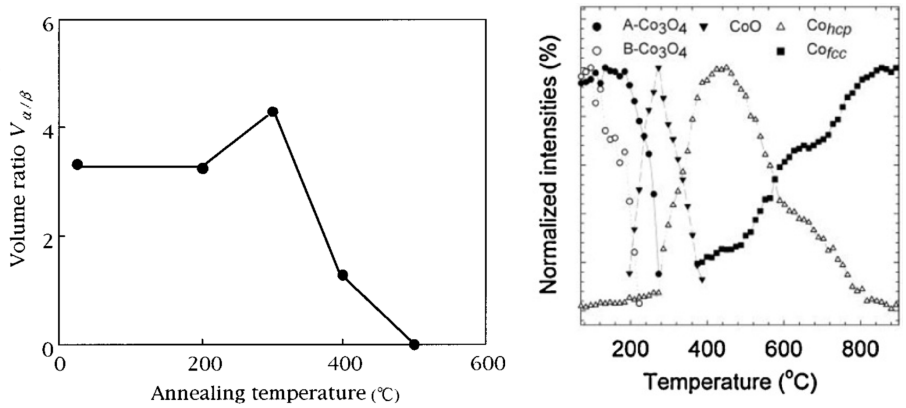

Figure 2.6: (a) Evolution of volume ratio $V_{\alpha/\beta}$ as a function of annealing temperature. α denotes the hcp phase, while β is the fcc structure. The cobalt particle diameter was 30nm [57]. (b) TPR-XRPD of a Co/CNF catalyst. The graphs show the successive reduction of Co_3O_4 to CoO and further to metallic cobalt in the phases hcp Co and fcc Co. A and B denote large and small Co_3O_4 crystallites respectively, as the particles studied had a bimodal particle size distribution [58].

The effect of temperature on the crystal phase was also studied by Tsakoumis et al.[58]. Temperature programmed reduction (TPR) up to 1000 °C at 10 °C/min of a carbon-supported cobalt catalyst monitored in situ by XRPD was used to reveal that the fcc and hcp phases were developing simultaneously during reduction. This indicates that the Co phases actually are intergrown. The TPR-XRPD in Figure 2.6b shows that the dominating phase is highly temperature dependent, and the hcp phase reaches a maximum right before the transition temperature of bulk cobalt from hcp to fcc at 420 °C, after which the fcc phase is prevailing. Sintering of cobalt crystallites was observed during the TPR, which can explain the increased intensity of the fcc phase in the XRPD in addition to further hcp - fcc transformation.

The intergrown phases presented by Tsakoumis et al.[58], and the annealing procedure performed by Kitakami et al.[57], indicate that the nanoparticles on the catalyst are not strictly one phase or another, but depending on size and temperature they are composed of fractions of the two. In situ XRD measurements are therefore required to accurately determine the phase composition of the nanoparticles during synthesis.

Influence of particle size

It has been documented that the activity of FT catalysts is closely linked to the particle size of the cobalt [59, 60, 61]. The turnover frequency is lower for smaller particles, and several studies have tried to uncover the mechanism behind this effect. Since carbon is an inert support material, it is well suited to study the properties of the cobalt particles without the interference of strong metal-support interaction.

Bezemer et al.[59] did an extensive study on the effect of cobalt particle size on the activity and selectivity of CNF-supported catalysts. Particles in the range of 2.6-27 nm were studied. Activity testing revealed that the TOF of particles with sizes above 6 - 8 nm was constant, while it decreased for smaller particles. Figure 2.7 shows the CTY and TOF of the different-sized particles. It is clear that the intrinsic activity of smaller particles is lower than particles above 6 nm.

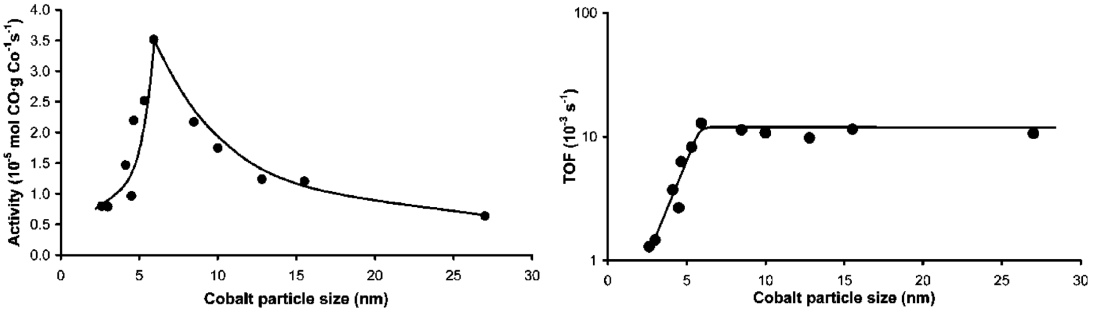

(a) **(b)**

Figure 2.7: (a) Activity (CTY) as a function of Co particle size. (b) TOF as a function of particle size. T = 220°C, $H_2/CO = 2$, p = 1bar. From [59]

The proposed explanation was that the domains that contain the active sites for FT synthesis, might not be stable, or might be present in a non-optimal ratio in smaller particles. It is also mentioned that CO-induced surface reconstruction might be part of the explanation.

It has been documented that CO has an invasive nature, and can cause restructuring of the cobalt surface, however, the mechanism is not completely known. Venvik et al.[62, 63] used STM to monitor changes in the cobalt structure upon adsorption of CO. They saw a migration of Co atoms on the cobalt surface resulting in a trough-and-ridge structure for both $(11\bar{2}0)$ and $(10\bar{1}2)$ facets. de Groot and Wilson [64] also studied CO-induced surface reconstruction that created triangular-shaped cobalt islands on the surface. Both authors suggest cobalt carbonyls are the mobile species, although this was not supported by any experimental findings. Even though the geometrical reconstruction is mostly referred to as being caused by CO, this might not be the case. Ciobîcă et al.[65] studied the effect of

FT adsorbates on the structure of the cobalt particle surface by density functional theory (DFT) calculations on fcc facets. They saw a change from more compact surfaces, to more open and reactive surfaces which they attributed to a reconstruction caused by adsorbed carbon as this was the only species that could change the order of stability of the different cobalt surfaces according to their calculations. Although CO might not directly cause the restructuring, the decomposed molecule will result in carbon bound to the cobalt that is capable of changing the surface structure.

den Breejen et al.[60] also looked into cobalt particle size effects by using Steady-State Isotropic Transient Kinetic Analysis (SSITKA). Their findings supported the conclusion of the study by Bezemer et al.[59]. In addition, the SSITKA experiments revealed that small particles have a lower surface coverage, and an increased residence time of CH_x intermediates than the larger particles, which impedes the activity. They were also able to measure the degree of irreversibly bonded CO, which was found to have a linear correlation with the fraction of cobalt surface atoms with a low coordination number (CN = 4-6). Smaller particles have a higher ratio of coordinatively unsaturated atoms, thus resulting in a higher degree of irreversibly bonded CO, which does not participate in the FT reaction. CO and CH_x species that are strongly bound to the surface of the particle geometry were proposed to influence the formation of CO reservoirs, which reduces the CO-induced surface reconstruction mentioned earlier.

Influence of carbon support oxidation

Many studies have been done on the influence of oxygen surface groups on the performance of a carbon-supported cobalt catalyst for the FT reaction. Doping of carbon with heteroatoms is mostly regarded as a way of introducing anchoring sites to the carbon and increasing the metal-support interactions. Metal anchoring is however not the only effect oxygen-functionalized carbon supports can have on the catalytic performance.

van Deelen et al.[66] studied pre-synthesized cobalt nanocrystals (NC) on carbon nanotubes (CNTs). They found the TOF of the oxidized supports to be 35% lower than for the catalyst prepared from the pristine CNFs. The lower TOF was attributed to differences in crystalline Co^0 on the two supports, as the cobalt particles on the oxidized support had a 32% lower crystallinity of metallic Co than the cobalt on pristine carbon. This effect was also reported by Chernyak et al.[67] in a study where they compared cobalt catalysts with and without oxidized supports. The cobalt on oxidized support was found to not be crystalline, and therefore not catalytically active. This was only observed on the support that had been treated with the most severe oxidation procedure, presumably because the high degree of functionalization prevents the formation of a crystal lattice. It is however important to note that although the surface groups hindered crystallization during reduction, it did not hinder the formation of a metal phase.

Not only the degree of crystallinity is affected by the oxidation. Other structural differences can be causing the change in activity for catalysts on functionalized supports. Eschemann et al.[2] also investigated the difference between oxidized and unoxidized CNFs as support for FTS. Similar to van Deelen et al.[66] they observed a lower TOF for the catalyst with oxidized support. Using in situ XRD they were able to attribute this difference in TOF

mainly to the presence of the hcp phase in the unoxidized catalyst, while it was not present in the cobalt on the oxidized support. As discussed previously, hcp is considered more active for the FT reaction than fcc.

Although many studies find a decrease in activity from the introduction of oxygen groups to the surface, this is not always the case. Davari et al.[68] looked into the effect of surface functionalization on catalytic performance. CNFs were used as the support material and functionalized with oxygen and nitrogen groups. Comparing the oxygen-functionalized and pristine CNF-supported catalysts, the oxidized catalyst shows a significantly higher CO conversion and FTS reaction rate (g CH/g cat./h). This is attributed to a higher BET surface area, better catalyst reducibility, higher metal dispersion, and decreased particle size which would increase the number of surface active cobalt sites. A TOF was not calculated. The particle size distribution is similar for particles larger than 6nm, while the oxidized catalyst has more particles in the range of 2-5nm. These are however not as active for the FT reaction, as discussed previously. Another paper that reported an increase in activity for functionalized support materials is a study by Trépanier et al.[69] The higher the degree of oxidation, the higher the CO conversion. Their conclusion was similar to Davari et al.[68], but they also attributed some of the differences to electron effects caused by the curved sp^2-hybridized carbon and the position of the nanoparticles on the CNTs showing that the cause of the increased activity can not solely be attributed to the direct influence of oxygen groups, but also the structural changes induced by the oxidation treatment.

2.2.2 Selectivity

The product from the FT synthesis can be described by the Anderson-Schulz-Flory (ASF) distribution presented in Figure 2.8 [70]. Then the molar fraction M_n, where n denotes the carbon number, is only dependent on the chain growth probability α following the relationship presented in Equation 2.1 [71].

$$M_n = n(1-\alpha)\alpha^{n-1} \tag{2.1}$$

where α can be expressed as a relationship between the rate of propagation reactions (r_p) and the rate of termination reactions (r_t) as presented in Equation 2.2.

$$\alpha = \frac{r_p}{r_p + r_t} \tag{2.2}$$

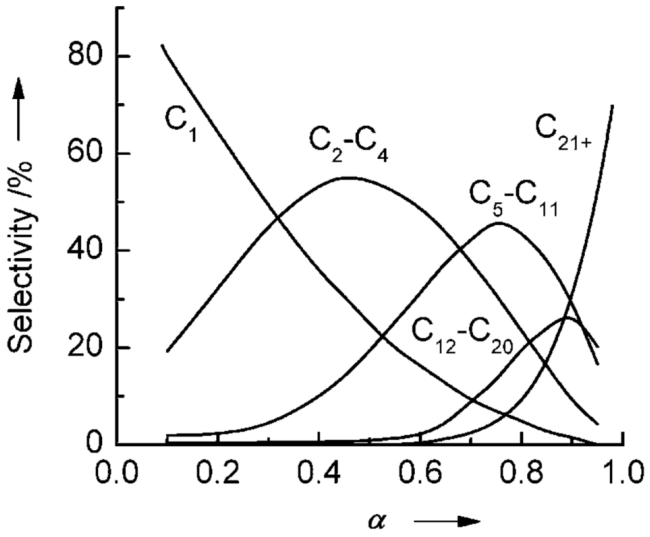

Figure 2.8: Depiction of the selectivity to different chain lengths changes with the chain growth probability, α. From [72].

The ASF distribution describes an ideal polymerization reaction and has been criticized as parts of the experimental product distribution deviate significantly from the predicted values[73, 71]. Enhanced selectivity to methane and a lower-than-predicted selectivity to C2 compounds are common deviations from the ASF distribution. The poor description of lighter hydrocarbons can be improved by calculating a separate chain-growth probability for each of the products following Equation 2.3[74]. Where r is the molar rate, and the subscripts g and t stand for growth and termination respectively.

$$\alpha_{C_n} = \frac{r_{g,n}}{r_{g,n} + r_{t,n}} = \frac{\sum_{m=n+1}^{\infty} r_{C_m}}{\sum_{m=n+1}^{\infty} r_{C_m} + r_{C_n}} \tag{2.3}$$

Lögdberg et al.[75] looked into the selectivity of the different hydrocarbon products. They observed that for cobalt catalysts there is a specific interrelationship between hydrocarbon selectivities that is also valid for the non-ASF distributed part of the product spectrum (C1-C5). This link is suggested to be a common monomer pool and therefore disregards the idea of separate methanation sites being present on the fresh catalyst. The formation of these separate active sites during the reaction is however not ruled out, which would be in line with what was suggested by Schultz et al.[52]. They propose that during FT synthesis, the structure of the catalyst changes, and that to understand the mechanisms behind the behavior of the catalyst, it is the structure that develops in situ that needs to be taken into account. The influence of CO on the surface structure was discussed in Section 2.2.1. There are three main domains created in this process according to Schultz et al. The first is peak and mountain sites where the cobalt atoms have low coordination numbers, these sites facilitate chain growth. The second type of active sites are hole and valley sites. These areas are suitable for CO dissociation. The third and final domain is the remaining plane sites that act mostly as hydrogenation catalysts. CO is also expected to bind strongly to these sites and hinder the adsorption of other species in the FT regime.

The desired products in FT synthesis are heavier hydrocarbons (C5+), as these compounds can easily be valorized further to fuels and other chemicals. In addition, methanation is successfully catalyzed in the industry today by nickel-based catalysts, methane formation is therefore not desired. The goal for FT catalysts is to have a high selectivity for C5+ hydrocarbons while producing as little methane as possible.

Influence of surface hydrogen coverage

The selectivity is closely linked to the amount of hydrogen available on the surface of the catalyst. A higher hydrogen coverage generally leads to the production of shorter hydrocarbon chains. The FT chain growth reaction can roughly be explained in three steps, and the selectivity depends on the relative rate of the three, namely chain initiation, chain growth, and complete hydrogenation to methane. As hydrogenation reactions are important, it is natural to look into the influence of hydrogen availability on selectivity.

Weststrate et al.[76] investigated the influence of surface species on the selectivity of the FT reaction. Iodomethane and dichloromethane were used to investigate the influence of hydrogenation vs. coupling reactions on $CH_{3,ads}$ and $CH_{2,ads}$ respectively. They observed that when there were vacancies on the catalyst surface where hydrogen could be accommodated, methyl dehydrogenation to CH followed by C-C coupling of the methyl adsorbates was the dominant path, while hydrogenation to methane was prevailing when there were few sites available for hydrogen to adsorb. The ratio of adsorbed hydrogen to the free sites available for hydrogen adsorption is therefore essential to understanding the mechanism that controls selectivity in FT synthesis. A high ratio favors methane production, while a low ratio promotes chain growth.

One of the mechanisms that dictate the amount of hydrogen available on the surface is hydrogen spillover. This effect involves dissociated hydrogen bound to the cobalt particles migrating onto the carbon support that acts as a hydrogen reservoir.

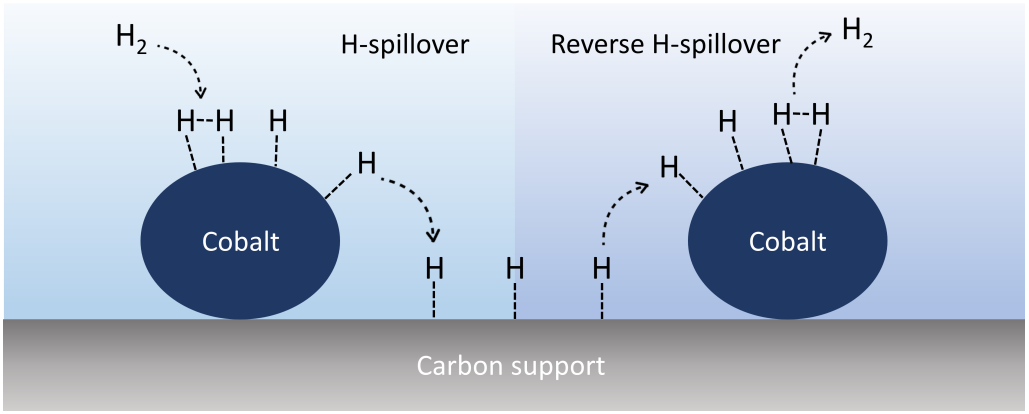

Figure 2.9: A schematic illustration of hydrogen spillover on carbon-supported cobalt particles.

Zhang et al.[77] looked into hydrogen spillover effects on the performance of a carbon-supported cobalt catalyst for the FT reaction. They found that smaller particles and carbon with a high frequency of defects exhibited a higher degree of atomic hydrogen

spillover from cobalt to the carbon surface than the other catalysts, and this resulted in a higher selectivity to methane. Thus indicating that particle size is a factor contributing to the extent of hydrogen spillover.

Functional groups on the surface of the carbon have also been studied as a possible influence on hydrogen spillover effects. Wang et al.[78] looked into the influence of oxygen functional groups on the hydrogen spillover of Pt-doped carbons. They found that oxygen groups enhanced the spillover effect by presenting possible adsorption sites for atomic hydrogen. Experimental results showed that carbon with dominating semiquinone groups measured by XPS had the highest hydrogen uptake. Ab initio molecular orbital calculations showed that the binding energies between the spilled-over hydrogen and the oxygen functional groups followed the following order: lactone > semiquinone > carboxyl, where lactone groups bound the hydrogen irreversibly.

Ghogia et al.[79] studied carbon-supported cobalt catalysts, and assessed differences in hydrogen spillover between varying carbon support materials, as well as oxidized and pristine carbon. From H_2-TPD measurements, they found that more hydrogen was desorbed than what could be attributed to the coverage of the metal particles. They concluded that the excess hydrogen must come from the surface, and the observations from the TPD stemmed from a reverse H-spillover effect. H_2-TPD also revealed hydrogen bound to the surface as a result of H-spillover. Both effects were enhanced by an increased number of oxygen functional groups and defects in the support. From FT tests of the catalysts, they could correlate the increased hydrogen spillover effects with a higher selectivity to methane, and a higher paraffin/olefin ratio.

Influence of particle size

Particle size is not only important for the activity of the catalyst, but it also plays an important role when it comes to selectivity. Studies on particle size effects show that the selectivity to C5+ hydrocarbons decreases, while the production of methane goes up for catalysts with particle sizes smaller than 6-8 nm [59, 60]. A high paraffin/olefin ratio was also found for small particles. Both findings indicate a higher hydrogenation activity. Figure 2.10a and 2.10b show the correlation between particles size and increased hydrogenation of surface species from a study by Bezemer et al.[59]. Figure 2.10c shows the correlation between particle size and hydrogen coverage on the surface of the catalyst. As can be seen from the data, the increase in hydrogen coverage correlates to a higher methanation activity and a higher paraffin/olefin ratio.

den Breejen et al.[60] used SSITKA experiments to determine the correlation between particle size and hydrogen coverage. As presented in Figure 2.10c, the hydrogen coverage increased significantly for particle sizes smaller than 5 nm. As mentioned previously, a higher degree of available hydrogen on the surface of the catalyst facilitates methane formation. This might explain the increased methanation activity of catalysts with smaller particle sizes.

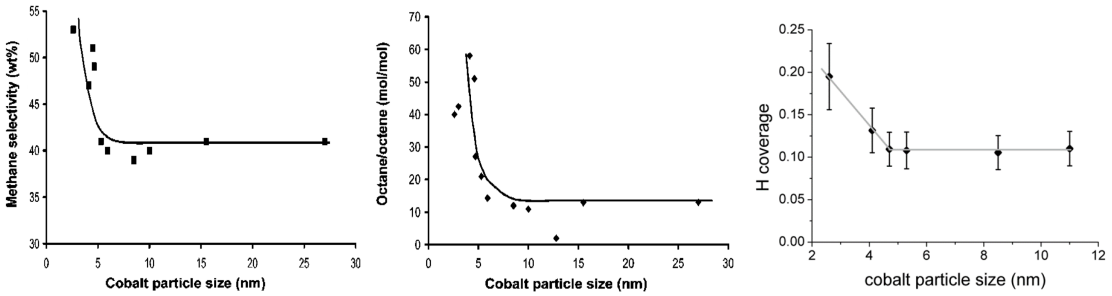

(a) **(b)** **(c)**

Figure 2.10: (a) Methane selectivity as a function of Co particle size. (b) Octane/octene ratio as a function of particle size. (a) and (b) T = 220°C, $H_2/CO = 2$, p = 1bar. Modified from [59] (C) Hydrogen coverage as a function of particle size. T = 210°C, $H_2/CO = 10$, p = 1.85 bar. From [60].

Influence of water

One of the main byproducts of the FT reaction is water, and it has been found that water significantly influences the selectivity towards C5+ products[80]. This effect is observed regardless of the origin of the water. Adding water to the reactor therefore had the same effect as increased water production during high conversions.

$$(2n+1)H_2 + nCO \rightarrow C_nH_{2n+2} + nH_2O \tag{2.4}$$

Equation 2.4 shows a simplified description of the polymerization reaction that happens during FT synthesis, and it is clear that one water molecule is created for each CO molecule consumed. Because of this, the water production is proportional to the conversion. As water influences selectivity, there is also a correlation between conversion and selectivity to C5+ products.

Influence of oxygen functional groups

As mentioned previously, oxygen has been found to influence hydrogen spillover effects. It is therefore interesting to look at how oxygen functionalization influences product distribution. Trépanier et al.[69] found that the selectivity towards C5+ hydrocarbons was reduced with increased support oxidation. Albeit CO conversion was not constant for the different catalysts tested, which also influences the selectivity as discussed earlier. The catalyst with the lowest conversion did however show the highest selectivity to C5+ compounds. The decrease in selectivity to higher hydrocarbon products was attributed to the increase of hydrogen adsorbed to the catalyst surface brought about by the oxygen functional groups. The increase in hydrogen causes more termination reactions, and hydrogenation to paraffins instead of chain growth to heavier hydrocarbons. Nakhaei Pour et al.[81] used a Langmuir-Hinshelwood-Hougen-Watson (LHHW) kinetic model developed by van Steen and Schultz [51] and the Van't Hoff equation to calculate the adsorption enthalpy for hydrogen on different catalysts. The heat of hydrogen adsorption was found to be highest for the unoxidized carbon support, while it decreased with the degree of func-

tionalization. This explains the increased hydrogen spillover that is observed for oxidized supports.

It is clear that hydrogen availability on the surface increases for oxidized supports, and that this leads to a higher degree of hydrogenation reactions, but there are other changes induced by the oxygen functional groups that influence the product distribution. According to a study by Eschemann et al.[2] the adsorption of α-olefins primary products on the hydrophobic CNT surface facilitates readsorption on the cobalt particles and favors additional chain growth. On a hydrophilic surface, this would not be observed, therefore this provides an explanation as to why oxygen functionalization leads to a higher paraffin/olefin ratio.

2.2.3 Deactivation

Catalyst deactivation is a process in which the catalyst loses its initial activity. The deactivation can be reversible or irreversible, and there are several deactivation mechanisms that are common for cobalt-based FT catalysts. The most prominent are sintering, reoxidation, and carbonaceous deposits covering the active sites. In addition, poisoning is a common problem in FT plants, but this topic will not be covered here as no compounds that could poison the catalyst were present in the syngas used for the experimental part of the thesis.

Sintering

Sintering is a process of crystallite growth, as the smaller surface-to-volume ratio of larger particles is energetically favored [82]. There are two main mechanisms of sintering, namely Ostwald ripening and coalescence. The first denotes atomic migration where smaller particles dissolve and combine with larger particles, while the latter describes crystallite migration where small crystals combine to form larger particles. The two phenomena are schematically illustrated in Figure 2.11. Sintering majorly influences the overall activity of the catalyst as it lowers the total surface area and thus the active sites that are available on the cobalt particles. The Hüttig temperature of the metal is an important factor to consider when dealing with sintering. The closer the reaction temperature gets to the melting temperature, the faster the solid-state diffusion gets, which in turn facilitates sintering. The Hüttig temperature is the temperature at which atoms at defects become mobile [83]. For bulk cobalt the Hüttig temperature is 253 °C, which is quite close to the operating temperature of FT synthesis, and lower than the reduction temperature common for carbon-supported cobalt FT catalysts [69, 2, 84]. In addition, the temperature when atoms become mobile might be much lower for small particles compared to the bulk of the same material[83].

Sintering is seen in most catalysts after some time on stream, but the nature of the support can influence the degree and rate. Strong metal-support interactions can prevent sintering and are therefore desirable to obtain a stable catalyst. On the other hand, too strong interaction can cause hard-to-reduce phases which are also undesirable. Designing good catalyst supports therefore requires intermediate metal-support interactions.

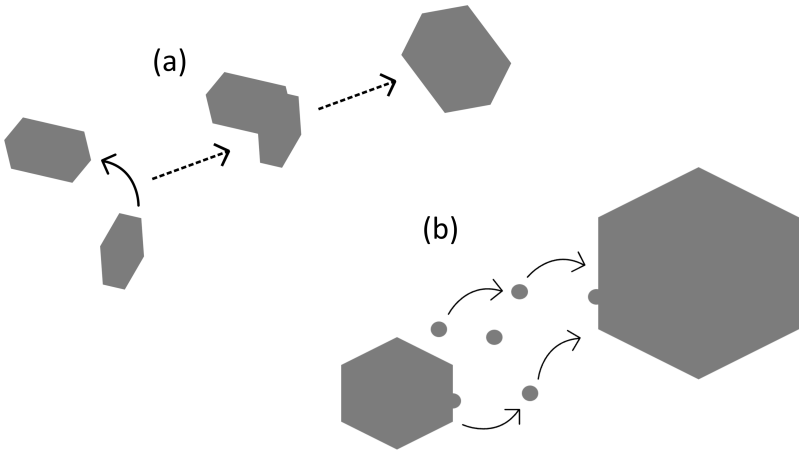

Figure 2.11: The two main sintering mechanisms (a) coalescence and (b) Ostwald ripening

As mentioned earlier, carbon is inert and therefore does not interact significantly with the metal particles. However, the addition of heteroatoms, for example oxygen, increases the support-metal interactions and can reduce sintering [84]. Chernyak et al.[32] looked into the effect of nitric acid treatment of CNFs at different durations on the stability of cobalt particles. They found that the oxidized supports prevent sintering of the cobalt particles, but also that the harshest acid treatment caused excessive harm to the support, which in turn led to more sintering than for the less oxidized supports. They concluded that the surface geometry played a larger part in preventing sintering than the oxygen groups themselves, as these defect sites with unsaturated carbon also can act as anchors for the metal particles [69].

van Deelen et al.[66] investigated the effect of oxidation treatment on CNT-supported pre-synthesized Co nanocrystals (NCs). In line with Chernyak et al.[32] they observed less sintering on the oxidized supports. They propose that the oxygen functional groups act as anchoring sites for the cobalt particles, and therefore prevent sintering. They also observed a lower degree of reduction (DOR) for the particles dispersed on the oxidized support, and suggest that the lower reducibility could result in remaining cobalt oxide that interacts more strongly with the oxidized surface compared to metallic cobalt. On the other hand, they observed smaller particles ($\sim$ 3 nm) on the oxidized supports after reduction and passivation which were not present on the fresh catalyst, indicating a redispersion during one of these treatments. These small particles could be the reason for a low DOR, as small particles are known to be harder to reduce. The increased immobilization of the particles can therefore both be attributed to oxygen functional groups on the surface, as well as defect sites created during acid treatment.

Reoxidation of cobalt particles

Although both CO and H_2 are reducing agents, the main by-product of FTS is water which is capable of oxidizing the cobalt particles. The partial pressure of water in the reactor is therefore an important parameter for this deactivation mechanism. At high conversions, there is more water produced, as discussed earlier, and therefore there is a chance that

the metal gets reoxidized during synthesis. The stability of cobalt nanoparticles at FT conditions was studied by van Steen et al.[85] as the properties of nanoparticles can vary significantly from the bulk properties of the metal. They saw that small metal cobalt nanoparticles could be oxidized to $Co(II)O$ in a water/hydrogen atmosphere similar to that during FT synthesis depending on the crystallite size, morphology, the starting crystal phase, support-metal interactions, and the p_{H_2O}/p_{H_2} ratio.

Experimental findings also show that reoxidation can be a likely deactivation mechanism. Yu et al.[27] used oxidized CNF-supported cobalt catalysts to study their performance for the FT reaction. TEM revealed that the particle size stayed similar to the fresh catalyst after reduction and throughout the synthesis. The catalyst was re-reduced after 120 h on stream, which recovered more than 90% of the initial activity. As no sintering was detected, and re-reduction restored most of the activity, they concluded that the deactivation was caused by re-oxidation related to the surface carboxyl groups introduced through the oxidation of the CNFs. On the other hand, Eschemann et al.[2] monitored the oxidation state of cobalt for the FT reaction over CNT-supported cobalt catalysts using in situ XANES and XRD measurements. Both the catalysts on oxidized and pristine carbon did not reoxidize during the duration of the experiment (8h). The degree of reduction was similar for both catalysts, and it was overall quite high. While Yu et al.[27] operated at a constant conversion of 50%, Eschemann et al.[2] did not keep the conversion constant, and it differed from catalyst to catalyst, ranging between 18 and 42%. The lower conversion causing a lower partial pressure of water could be part of the explanation for the differences observed, but as mentioned earlier, p_{H_2O}/p_{H_2} ratio is just one of many parameters influencing the rate of reoxidation.

Carbonaceous deposits

The surface of FT catalysts is covered by carbon-containing molecules, be it CO or longer hydrocarbon chains. It is therefore not unlikely that carbon species that act as inhibitors by blocking active sites can be formed under reaction conditions through for example the Boudouard reaction shown in equation 2.6 [82].

$$CO \rightleftharpoons CO_2 + C \tag{2.5}$$

$$CO \rightarrow CO_2 + C_{ads} \tag{2.6}$$

TEM images can reveal if the metal nanoparticles are covered by carbonaceous species. Chernyak et al[67] used TEM to discover encapsulated amorphous cobalt on their catalyst, while no encapsulation was observed for the crystalline particles. This lead to the conclusion that the carbon disproportionation (DP) reaction shown in Equation 2.5 proceeds predominantly on the particles with poor crystallinity. This could be caused by low hydrogenation activity at those surfaces. Amorphous particles have a large degree of unsaturated sites that coordinate CO molecules which facilitates carbon formation through the DP reaction. The amorphous carbon was found on oxidized carbon supports, while the untreated carbon had particles with a higher degree of crystallinity.

Although carbon formation on the surface of catalysts has been detected as a possible deactivation mechanism, generally the hydrogen present on the cobalt surface should not allow carbon to accumulate to the degree of deactivation, as it is mostly rapidly hydrogenated and therefore regarded as a surface intermediate[82]. In the case of hydrogen deficiency, however, it is more likely to occur a buildup of carbonaceous species which might cause catalyst deactivation.

Chapter 3

Theory

3.1 Catalyst preparation

3.1.1 Oxidation with nitric acid

The surface chemistry of carbon can be changed by introducing oxygen functional groups with an oxidation agent such as nitric acid. The oxidation mainly takes place on the edges of basal planes and at point-defects in the carbon matrix [5]. Carbon black is a paracrystalline sp^2 hybridized carbon, and there are a wide array of defect sites suited for oxygen functionalization on the surface. Describing the oxidation mechanism for carbon black with nitric acid is complicated as the structure around the reactive carbons atoms at different defect and edge sites varies greatly. Several authors have performed theoretical studies of carbon nanotubes (CNTs) as model systems to gain insight into oxidation with nitric acid, but only detail specific reaction sites [86, 87]. In general, the aqueous solution of nitric acid involves the presence of three ions, namely NO_3^-, NO_2^-, and H_3O^+.The result of the oxidation is a wide variety of oxygen groups on the surface, although the exact composition might vary slightly with oxidation time and temperature [86, 14].

3.1.2 Thermal desorption

The oxygen functional groups that form on the carbon surface are thermolabile and decompose to CO and CO_2 at elevated temperatures. Thermal desorption of groups is both a tool that can be used to identify groups on a carbon surface and for changing the surface chemistry of the oxidized carbon. Depending on the identity of the group, and the chemical environment it is in, it has a specific desorption energy. When a group desorbs, it requires a carbon-carbon bond breakage, and the energy required to break this bond varies slightly depending on how the oxygen is bound to the carbon, and the structure of the surface [45]. The majority of carbon surface oxygen functional groups decompose when exposed to temperatures between 100 and 1000°C, with carboxylic acids generally desorbing at relatively low temperatures, followed by primary alcohols, carboxyl anhydrides, phenols, ethers, carbonyls, lactones, and quinones [41]. During TPD measurements, the sample is generally heated in an inert atmosphere to avoid reactions with species in

the gas phase.

3.1.3 Colloidal cobalt nanoparticle synthesis

Thermal decomposition is one of the most useful techniques for synthesizing uniform metal nanoparticles with regard to shape and crystallinity [88]. A precursor of the desired metal is added to a solution with an organic surfactant [89]. The precursor is typically an organometallic compound or an inorganic salt. The nanoparticle formation consists of four stages, pre-nucleation, nucleation, growth, and annealing. One of the goals of the synthesis is to have a narrow size distribution, which requires the nucleation and growth stages to be temporally separated. This can be achieved by using a hot-injection method where a precursor at room temperature is injected into a hot solution containing surfactants leading to instant nucleation of metal particles [90]. After the initial nucleation, the particles start their growth phase. The surfactants bind to the surface through Lewis-acid-base interactions where the polar head of the ligand acts as a base [89]. The interaction between the metal and the ligand dictates the shape and size of the nanoparticles. A strong interaction might hamper growth, but provide stability and surface passivation, while a weak bond might result in uncontrolled growth and insufficient colloidal stability.

Metallic cobalt nanoparticles are oxidized when they come into contact with air after the synthesis. Depending on the temperature at which the cobalt particles are exposed to oxygen either CoO or Co_3O_4 is formed [13]. Exposure at room temperature will yield CoO, while exposure at elevated temperatures ($\sim 200°C$) will yield Co_3O_4. van Deelen et al. found that Co_3O_4 particles grew more during reduction and FT synthesis, CoO particles were therefore preferred.

3.1.4 Loading of pre-prepared nanoparticles

The pre-synthesized nanoparticles were deposited on the carbon support through wet impregnation, meaning that the pre-synthesized nanoparticles were mixed with the carbon in a solution that was in excess of the support pore volume, unlike incipient impregnation, where the volume of the solution would be equal to the pore volume [91]. In order to provide good dispersion of the particles on the carbon support and to avoid agglomeration, the procedure was carried out at 200°C. The high temperature ensures high nanoparticle mobility, which facilitates a high dispersion.Nanoparticles are known to adhere to surfaces because of their high surface-to-volume ratio, therefore the nanoparticles are deposited onto the carbon support instead of remaining in the solution [92].

3.2 Characterization

3.2.1 BET

A common way to determine the surface area and pore structure of a catalyst or catalyst support is by nitrogen adsorption-desorption [93]. Nitrogen physisorbes to the surface and

the nitrogen uptake is measured as a function of relative pressure. The principle behind the method is to gain knowledge on the amount of gas necessary to form a complete monolayer on the surface [94]. An N_2 molecule takes up 0.162nm^2 at 77 K, and using the number of molecules needed to form a monolayer it is possible to calculate the total surface area of the sample as shown in Equation (3.1). The specific surface area of the material can then be calculated using Equation (3.2).

$$A_s = n_m N_A \rho_m \tag{3.1}$$

$$a_s = A_s / m \tag{3.2}$$

A_s is the surface area of the sample being measured, n_m is the monolayer capacity, N_A is avogadros number, ρ_m is the area occupied by one adsorbed nitrogen molecule, a_s is the specific surface area and m is the mass of the sample that is being measured. The Brunauer-Emmett-Teller (BET) equation, shown in Equaiton (3.3), is used to find the monolayer capacity.

$$\frac{p/p^0}{n(1-p/p^0)} = \frac{1}{n_m C} + \frac{C-1}{n_m C}(p/p^0) \tag{3.3}$$

Where n is the specific amount adsorbed to at the relative pressure p/p^0 and n_m is the specific monolayer capacity. C is a parameter that is exponentially related to the energy of monolayer adsorption [93]. The specific monolayer capacity is found by using the linear relationship between $(p/p^0)/n(1-p/p^0)$ and p/p^0. It is necessary to restrict the pressures used for the BET plot to the linear part of the isotherm.

3.2.2 XPS

XPS provides information about the chemical nature of the surface of a sample such as elemental composition, the oxidation state of the elements, and the dispersion of one phase over another [95]. The method measures the intensity of photoelectrons as a function of their kinetic energy. An incoming X-ray beam illuminates the sample, and an atom adsorbes a photon of energy hv so that a core or valence electron with binding energy E_b is ejected. The kinetic energy (E_k) of the photoelectron can be described by Equation (3.4).

$$E_k = hv - E_b - \phi \tag{3.4}$$

h is Planck's constant, v is the frequency of the exciting radiation, and ϕ is the work function of the spectrometer. The binding energy E_b is relative to the Fermi level of the sample.

3.2.3 XRD

XRD is one of the most commonly used characterization methods to assess crystalline solid materials [95]. It gives information about the crystalline phases present and an indication of crystallite size. X-ray diffraction occurs when an X-ray beam is elastically scattered by atoms in a periodic lattice. The scattered monochromatic X-rays interfere constructively when they are in phase, and the angles of maximum intensity allow for the calculation of the spacing between the lattice plane by using Braggs relation presented in Equation (3.5),

$$n\lambda = 2d\sin\theta; \quad n = 1, 2, ... \tag{3.5}$$

where n is the order of the reflection, λ is the wavelength of the incoming X-rays, d is the interspacing between the lattice planes, and θ is the angle between the incoming X-rays and the normal to the reflecting lattice as shown in Figure 3.1.

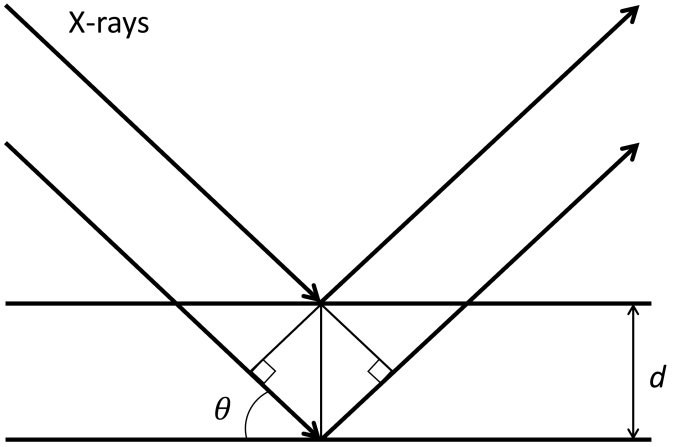

Figure 3.1: X-rays scattering by atoms in a periodic lattice. d is the space between the lattice planes and θ is the angle between the incoming X-rays and the normal to the reflecting plane. Adapted from [95].

The crystal size of the sample can be related to the peak width from the XRD diffractogram using the Scherrer formula presented in Equation (3.6),

$$< L >= \frac{K\lambda}{\beta\cos\theta} \tag{3.6}$$

where $< L >$ is a measure of the dimension of the particle in the direction perpendicular to the reflecting plane, λ is the wavelength of the X-ray, β is the peak width, θ is the angle between the beam and the normal to the reflecting plane, and K is a constant.

3.2.4 TPD

Temperature programmed desorption (TPD) uses the thermolability of surface species to assess the surface chemistry of a sample [41]. The sample is heated in an inert atmosphere during a temperature ramp, which is typically either linear or a sequence of linear and isothermal steps [45]. The decomposition products of oxygen functional groups on a carbon surface are CO and CO_2, which are analyzed with a mass spectrometer (MS) as they are emitted from the sample. The difference in desorption temperatures between the oxygen groups ensures a difference in intensity in the emitted gases, enabling the separation of groups on the basis of decomposition temperature. The desorption rate r_d follows Arrhenius' law and can be described by the Polanyi-Wigner equation presented in Equation (3.7) [96].

$$r_d = -\frac{dN_A}{dt} = A \cdot N_A^x exp\big(-\frac{E_d}{RT}\big) \tag{3.7}$$

N_A is the concentration of adsorbed groups, t is time, E_d is the activation energy for desorption, A is a pre-exponential factor of the desorption rate constant, x is the kinetic order of desorption, R is the gas constant, and T is temperature. E_d and A can be functions of the coverage of surface species.

3.2.5 TPR

Temperature programmed reduction (TPR) is a method used on reducible catalysts to gain information about the behavior during reduction[97]. The catalyst is exposed to a reducing atmosphere, usually a mixture of hydrogen and an inert gas, during a specific temperature program. Typically the reducing behavior is observed during a linear temperature ramp to determine at which temperature the catalyst is reduced and the degree of reduction. The rate of reduction is measured by monitoring the hydrogen content at the outlet of the gas stream passing through the catalyst bed. This technique can also give information about the initial oxidation state of the sample.

3.2.6 Raman spectroscopy

Raman spectroscopy is a way of determining the structural properties of a material. The sample is irradiated with a single frequency of radiation, which is scattered when in contact with the sample[98]. The scattered beam is detected, and the energy is one vibrational unit of energy different from the energy of the incident beam. The scattering takes place by the incoming light interacting with the sample and distorting the cloud of electrons around the nuclei which forms an unstable temporary state called a "virtual state". As the state is not stable, the photon is quickly re-radiated. This type of scattering is referred to as Rayleigh scattering and is considered elastic, as the photon will be emitted with very small frequency changes. If the incident beam induces nuclear motion, energy will either be transferred from the incident photon to the molecule, or from the molecule to the photon by one vibrational unit. This is called Raman scattering, and the process is

considered inelastic as the energy of the photon changes after scattering. Figure 3.2 shows the change in energy between the vibrational states for Rayleigh and Raman scattering.

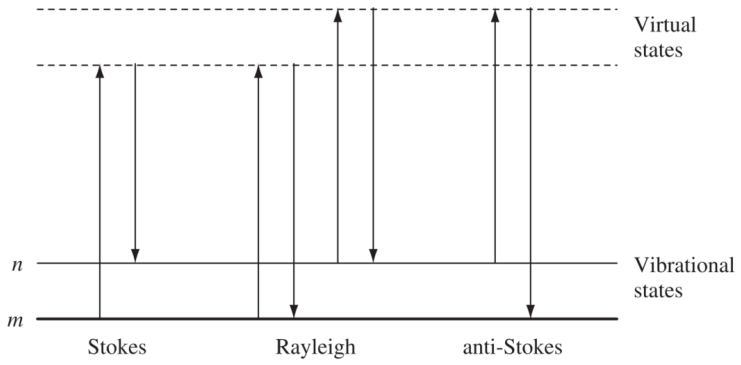

Figure 3.2: Raman and Rayleigh scattering. m is the ground vibrational state and n is an excited vibrational state. From [98].

If Raman scattering leads to an absorption of energy by the molecule, the process is referred to as Stokes scattering, while if the molecule is present in an excited state and energy is transferred to the scattered photon, the process is called anti-Stokes scattering.

3.2.7 S(T)EM

Scanning transmission electron microscopy (S(T)EM) is an electron microscope that combines the properties of scanning electron microscopy (SEM) and scanning transmission electron microscopy (STEM). A transmission stage and a detector can be fitted onto a SEM instrument to operate it in STEM mode.

A TEM image is created by electrons passing through a sample of various density and thickness, causing the electrons to lose energy [95]. The transmitted electrons form a two-dimensional image with varying brightness depending on the attenuation of the beam. SEM involves rastering an electron beam across the surface of the sample to detect secondary or backscattered electrons as a function of the position of the primary beam. The contrast of the image is dependent on the angle at which the electrons are emitted in relation to the detector. The parts of the surface facing the detector appear brighter than areas that are facing a different direction.

3.2.8 MP-AES

Microwave plasma atomic emission spectrometry (MP-AES) is an analysis designed to quantify elements in a solution [99]. In atomic emission spectroscopy, the atoms of the analyte are excited by a high thermal environment and promoted to a relatively higher energy level [100]. When the excited atoms are shifted back to lower energy they emit light at specific wavelengths depending on the element. The light is detected at the element specific wavelength, and the emission intensity is proportional to the concentration of atoms or ions in the solution which makes it possible to use the emission data for quantification. The sample is heated in a nitrogen-based plasma with a temperature of

approximately 5000 K [99]. The sample is injected into the plasma with a nebulizer. As the analyte has to be in a solution, acid digestion is commonly applied to solid materials in order to use MP-AES.

3.2.9 Gas Chromatography

Gas chromatography (GC) is used to analyze components in gas streams [101]. There are two phases, one mobile and one stationary, in the case of GC, the mobile phase is a gas with the analyte. The mobile phase transports the analyte along the stationary phase. The analyte distribution between the gaseous and stationary phases is dictated by adsorption or solubility depending on whether the stationary phase is a solid or a liquid respectively. The separation process can be described by a series of discrete equilibrium steps where equilibrium is formed between the solute in the mobile and in the stationary phase. The solute that remains in the mobile phase after equilibrium is established is transported to the next equilibrium step where a new equilibrium is reached. In reality, a complete equilibrium is not reached at each distribution step, and the mobile phase does not move steadily through the column. The solute distribution over the column is expected to follow a normal distribution, and the chromatography peaks therefore have a Gaussian peak shape. The identification of a compound in a gas mixture can be obtained by comparing the retention time of compounds in the analyte with the retention time of known samples. The relative concentration can be found by assessing the peak area or height.

Chapter 4

Methods

4.1 Catalyst preparation

4.1.1 Oxidation of carbon black

Carbon black (Printex 60, Orion Engineered Carbons) was oxidized with nitric acid (65.0-67.0%, Sigma-Aldrich) based on a procedure suggested by V. Datsyuk et al.[34]. The protocol is similar to the oxidation performed during the specialization project [14]. Generally 2.2 g carbon black was dispersed in 55 mL nitric acid in a 150 mL round bottom flask equipped with a condenser and magnetic stirring at 250 rpm. The flask was submerged in an oil bath that was heated to the desired temperature. Four carbon black samples were oxidized at different temperatures. The oxidation temperatures were chosen based on the work presented in the specialization project that was completed prior to starting the master thesis[14]. The chosen temperatures were 70, 95, 120, and 140°C. The solution was kept under these conditions for 2 h. Afterward, the dispersion was transferred to a centrifuge tube, and centrifuged at 5000 rpm for 5 minutes. The supernatant was decanted, and the carbon black was re-dispersed in deionized water before centrifuging again with the same parameters. The washing cycle was repeated three times. After washing the sample was dried overnight at 100°C in a drying oven.

4.1.2 Heat treatments

After oxidation, the carbon black samples were heat treated in an electric furnace under an inert atmosphere. The carbon was heated in a tubular quartz reactor with a quartz sintered disk to hold the carbon black in place. The temperatures were chosen based on TPD measurements that were taken during the specialization project, and the heat treatment procedure is the same as employed then [14]. The samples were treated at 330, 530, and 650°C to remove oxygen groups that desorb below the temperature in question. The samples were heated at a heating ramp of 5 K/min, and the desired temperature was held for 2 h. Argon was used as the inert gas, and the flow through the reactor was 100 mL/min.

A sample of carbon black without oxygen functional groups was prepared by heating pristine carbon black in a flow of 10 mL/min hydrogen and 90 mL/min argon to 950°C. The high temperature is expected to remove all oxygen functional groups that are present on the carbon after synthesis, and the hydrogen is present to avoid reactive carbon sites created by the desorption of functional groups re-adsorbing oxygen when exposed to the atmosphere after heat treatment. The samples were named based on the oxidation and heat treatment temperature after the convention CB-*"oxidation temperature"* - H*"Heat treatment temperature"*.

Table 4.1: Acid and heat treatment temperatures of the catalyst support materials.

Name	Oxidation temperature [°C]	Heat treatment temperature [°C]
CB-H	-	950
CB-70	70	-
CB-95-H330	95	330
CB-120-H530	120	530
CB-140-H650	140	650

4.1.3 CoO nanoparticle synthesis

The nanoparticles used in the master thesis were synthesized as part of the specialization project prior to starting the thesis [14]. The particles were prepared according to a procedure by van Deelen et al.[66], which was based on a previously reported method by Iablokov et al.[102]. A schematic illustration of the procedure is presented in Figure 4.1.

The cobalt nanoparticles were prepared via a colloidal synthesis. 73.5 μL oleic acid (90% technical grade, Sigma-Aldrich) was transferred to a 100 mL 3-necked flask equipped with a condensation column and two septa. The flask was connected to a Schlenk line through the condenser column. The Oleic acid was degassed at 100°for 30 minutes under vacuum with magnetic stirring at 150 rpm. Subsequently, nitrogen was introduced to the system, and the flask was restored to atmospheric pressure. 7.5 mL 1,2-dichlorobenzene (99% anhydrous, Sigma-Aldrich) was injected into the flask via a 10 mL syringe. The mixture was heated to 174°C under constant magnetic stirring at 750 rpm.

While the flask was heating, 270 mg of dicobalt octacarbonyl (90%, Sigma-Aldrich) was dissolved in 1.5 mL 1,2-dichlorobenzene inside a glovebox. The cobalt precursor was introduced to the flask via a syringe after the solution in the flask had reached 174°C. The nanoparticles formed for 20 minutes after injection of the precursor, before the reaction was quenched with a water bath. The septa were removed from the flask, and the nanoparticles were exposed to air at room temperature under 650 rpm magnetic stirring for one hour to oxidize the metallic cobalt to CoO.

The nanoparticles were washed with 2-propanol. First, the solution from the flask was transferred to centrifuge tubes and 2-propanol was added to a total volume of 40 mL. The dispersion was centrifuged for 20 minutes at 2200 G. The supernatant was decanted before the nanoparticles were re-dispersed in 1 mL n-hexane (100 $\geq$, Merck) using a vortex mixer. 2-propanol was added to the solution to a total volume of 40 mL, and the washing cycle was repeated three times. After the last wash, the nanoparticles were re-dispersed

in 2 mL toluene (100 ≥, Merck) and stored in a glass vial.

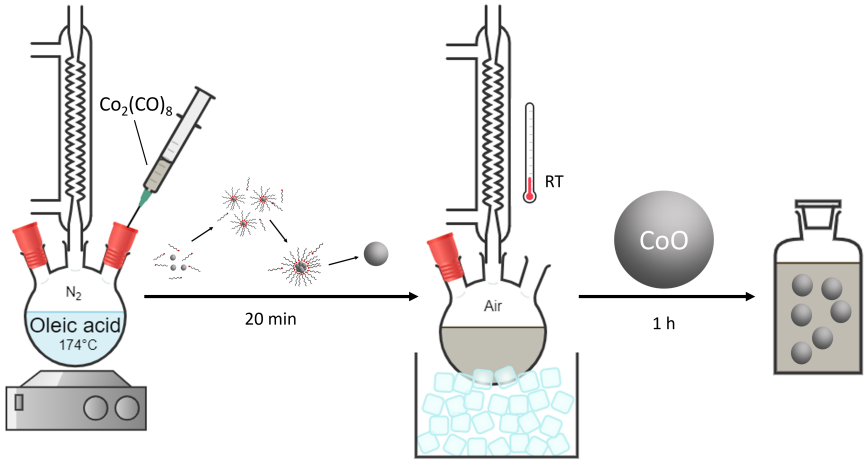

Figure 4.1: Schematic illustration of the synthesis of CoO nanoparticles through the hot injection method. From [14]

4.1.4 Nanoparticle deposition

The cobalt nanoparticles were deposited on the carbon black support through wet impregnation at elevated temperature under a nitrogen atmosphere on a Schlenk line following a procedure by van Deelen et al.[13]. 15 mL of 1-octadecene (90% technical grade, Fischer Scientific) was added to 0.75 g of support in a three-necked round bottom flask equipped with a cooler and stirred for 15 minutes at 400 rpm to disperse the carbon in the solvent. 2400 μL of the nanoparticle solution was added to the flask and closed with two septa. The suspension was heated to 50 °C while drawing vacuum. The solution was then degassed at 100°C for 30 min before the flask was flushed with nitrogen, and the temperature was raised to 200°C and held for 30 min. Subsequently, the suspension was cooled in an inert atmosphere.

The suspension was transferred to a centrifuge tube and acetone was added to aid in the transfer and separation of the catalyst. The suspension was centrifuged for 5 min at 2500 G. The supernatant was decanted, and the catalyst was re-dispersed in 2 mL n-hexane, and washed with 6 mL acetone before centrifuging again at the same conditions. The washing cycle was repeated 6 times. Finally, the catalyst was dried at 60°C in a vacuum oven. The catalysts were named after the following convention, Co/CB-*"oxidation temperature"* - H*"heat treatment temperature"*

4.2 Catalytic testing

4.2.1 Reduction

Reduction experiments took place in the same fixed-bed reactor that was used for the catalytic testing. Typically 40 mg undiluted catalyst was placed inside a tubular metal reactor and held in place by two glass wool plugs. The reactor was installed into the

reaction setup as schematically presented in Figure 4.2. The catalyst was reduced under a flow of 7.5 mL/min argon and 2.5 mL/min hydrogen. The reactor was heated to 350°C at 1 K/min, and the catalyst was reduced at this temperature for 8 h at atmospheric pressure. After the reduction, the reactor was cooled to room temperature, and the catalyst was passivated with 10 mL/min 1% O_2 in Ar for 2 h.

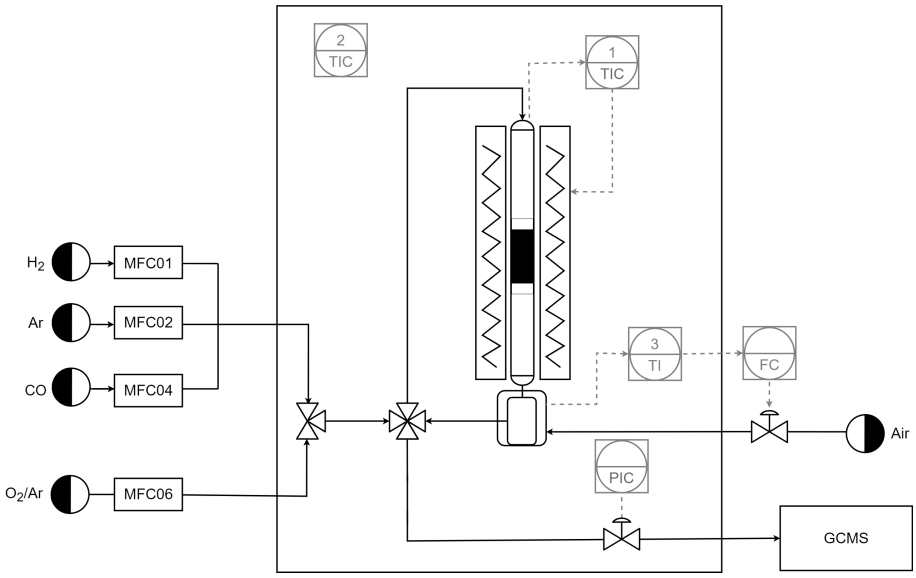

Figure 4.2: Simplified illustration of the setup used for catalytic testing. The full PID can be found in Appendix I

4.2.2 Fischer-Tropsch synthesis

Fischer-Tropsch synthesis tests took place in a tubular fixed-bed reactor. Typically 200 mg of catalyst mass was mixed with 800 mg of SiC to ensure even heat distribution inside the reactor. The catalyst was held in place inside the reactor by two glass wool plugs. The catalyst was reduced in a flow of 7.5 mL/min argon and 2.5 mL/min hydrogen at 350°C for 8 h at atmospheric pressure as described above. After the reduction, the temperature was decreased to 190°C at 5 K/min in a flow of argon. The temperature was held at 190°C for 1 h before the pressure inside the reactor was increased to 20 bar with a pressure ramp of 5 bar/min. After two hours the synthesis gas was introduced, 3.05 mL/min hydrogen, 1.45 mL/min carbon monoxide, and 0.5 mL/min argon as an internal standard for the gas chromatograph. 12 h after introducing the syngas, the temperature was increased to 220°C with a temperature ramp of 0.1 K/min. The temperature was held constant for 80 h before increasing the temperature further to 230°C at 1 K/min. This temperature was maintained for 15 h before the temperature was raised again, from 230 to 240°C with a temperature ramp of 1 K/min. 240°C was held constant for an additional 15 h before the temperature was lowered back to 220°C. After 5 h, the temperature was lowered to room temperature, and the pressure was subsequently lowered to atmospheric pressure, and the reactor was flushed with argon for 1 h. 10 mL/min O_2 in argon was introduced to passivate the catalyst before it was removed from the reactor.

4.3 Characterization

4.3.1 Nitrogen adsorption-desorption

The BET surface area was determined by N_2 adsorption-desorption isotherms measured in a Micrometrics Tristar 3020 BET porosimeter using the Brunauer-Emmet-Teller (BET) equation. The samples were degassed overnight at 200°C under vacuum prior to the measurement. The adsorption and desorption were measured at 77K from 0.00 to 0.99 p/p^0. Typically, 60 mg of each sample was used for the measurement.

4.3.2 Raman

Raman spectroscopy was measured using a Horiba Jobin Yvon HR800 with a 633 laser, an acquisition time of 60 s and 10 accumulations. The spectra were recorded between 900 and 2000 cm^{-1} The data were fitted according to the procedure described by Mallet-Ladeira et al. [103].

4.3.3 XPS

The XPS measurements were carried out by Dr. Felix Herold. X-ray photoelectron spectroscopy (XPS) was measured on a Kratos Analytical Axis Ultra DLD spectrometer with a monochromatic Al Kα irradiation (1486.6 eV). The anode was operated at 10 kV with an aperture of 700 x 300 μm. Surveys were recorded with a pass energy of 160 eV. HR-XPS measurements were carried out with a pass energy of 20eV.

4.3.4 XRD

X-ray diffraction measurements were taken with a Bruker D8 ADVANCE DaVinci with Cu$\kappa\alpha$ radiation and a LynxEye SuperSpeed Detector. The acquisition time of each measurement was 120 min, and the sample was measured with 2θ values between 10°and 75. A fixed slit of 0.2°was used for all the measurements. To avoid dust formation during handling of the sample, Kapton foil was used to cover the catalyst.

4.3.5 S(T)EM

S(T)EM images were taken on a Hitachi High-Tech SU9000. Typically an acceleration voltage of 30kV and an emission current of 10μV was employed. The particle size distributions were determined using more than 150 individual particles from each sample. The S(T)EM samples were prepared by dispersing the catalyst in n-hexane by sonication before the solution was drop-casted on a TEM grid. The spent catalyst was dispersed in n-hexane and stirred for 1 h with a magnetic stirrer before depositing it on the grid to dissolve any FT products that might be present on the catalyst surface in order to obtain a clear image of the catalyst after catalytic testing.

4.3.6 TPR

TPR was carried out using an Altamira Benchcat Hybrid-1000HP unit. Typically 30 mg of catalyst was placed inside a u-shaped quartz reactor between two glass wool plugs. The sample was heated inside an electrical furnace. Two temperature programs were used to assess the reduction behavior of the catalyst. First a linear temperature ramp from room temperature to 800°C with a heating ramp of 5 K/min. The second temperature program was similar to the reduction procedure before catalytic testing. The catalysts were reduced at 350°C for 8h, followed by a temperature ramp to 800°C with a temperature ramp of 5 K/min.

4.3.7 MP-AES

The MP-AES measurements were carried out by Dr. Felix Herold. The catalyst was dissolved in 10 mL aqua regina by microwave digestion in a Berghof SpeedWave XPERT device. The solution was subsequently diluted to 50 mL with deionized water before the samples were filtered. An Agilent 4210 MP-AES device was used for the quantification of the cobalt content. The calibration was carried out with Co standards.

4.3.8 TPD

The TPD measurements were carried out by Oliver Leubner at TU Darmstadt in a STA 409 PC Luxx thermogravimetric balance (NETZSCH) coupled to a calibrated online mass spectrometer (Omnistar, Pfeiffer Vacuum) with a heating ramp of 5 K/min and with helium as carrier gas. The data were fitted using Gaussian functions as explained in Appendix A.

Chapter 5

Results and Discussion

This section aims to present the data collected during support and catalyst characterization to shed light on the influence of carbon surface chemistry on the performance of the catalysts during FT synthesis. First, the characterization of the support is presented, then the properties of the fresh catalyst, reduction experiments and the measurements taken of the reduced catalysts, results from the FT synthesis experiments, and finally properties of the spent catalysts are presented.

5.1 Support

The goal of the oxidation procedure and the subsequent heat treatment was to produce carbon with different surface oxygen group distributions, but similar oxygen loading. The carbon black was first oxidized with nitric acid, introducing a wide array of oxygen groups, followed by a heat treatment to remove groups. This method takes advantage of the different decomposition temperatures of the surface groups to modify the surface chemistry. A schematic representation of oxygen groups leaving the surface can be seen in Figure 5.1. In reality, the surface groups decompose as CO and CO_2. Heat treatment temperatures were chosen from TPD measurements taken during the specialization project with the aim to completely desorb certain groups while groups with higher decomposition temperatures are still intact[14]. The oxidation temperature was chosen to keep the total surface oxygen content similar on each of the supports. A higher oxidation temperature introduces more oxygen groups to the carbon surface. As a higher heat treatment temperature removes an increased number of different surface groups, the concentration of each of the remaining groups has to be higher than for carbon with a wider array of groups in order to keep the total oxygen content the same. The structural and textural properties of the support are also important to the performance of the catalyst, and should therefore be comparable for all the functionalized carbons. Acid treatments are known to be invasive and create defects in the carbon. Structural, textural, and chemical changes to the carbon support material are presented in this section.

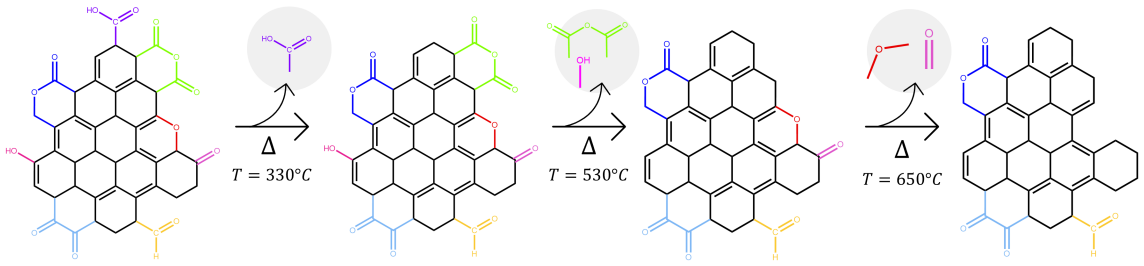

Figure 5.1: Schematic illustration of oxygen functional groups being eliminated from the carbon surface during heat treatments.

5.1.1 Structure and textural properties

The texture of the carbon black was assessed by nitrogen physisorption. The specific surface areas of the catalyst supports are presented in Table 5.1. The surface area increases with increasing oxidizing temperature and heat treatment temperature. Previous experiments performed during the specialization project showed that the surface area increases significantly with oxidation above 80°C [14]. The increased surface area is likely caused by the nitric acid damaging the carbon and roughening the surface, possibly creating small pore structures or opening occluded pores that were present in the carbon particles [28, 30, 66, 104]. The heat treatment is also likely to cause a further increase in surface area [14]. As the oxygen groups desorb they take carbon atoms with them, which leads to additional roughening of the surface.

Table 5.1: The specific surface area of the support materials measured by nitrogen adsorption-desorption. CB denote untreated carbon black.

	SSA $[m^2/g]$
CB	113
CB-H	114
CB-70	118
CB-95-H330	175
CB-120-H530	287
CB-140-H650	426

The isotherms from all the functionalized carbon can be found in Appendix D. Figure 5.2a shows the isotherm of CB-H which is typical for the shape of the carbon black isotherms. The isotherm is classified as type IV(a) with an H1 hysteresis loop [93]. This indicates a narrow-range mesoporous structure where capillary condensation took place during measurement.

Figure 5.2 shows a comparison of the BET isotherm of CB-H and CB-140-H650. The knee of the CB-140-H650 isotherm is significantly higher than CB-H, indicating a higher overall surface area and increased microporosity [93]. However, CB-140-H650 is also classified as a IV(a) isotherm. The shape of the hysteresis has changed slightly in the relative pressure range between 0.4 and 0.8, indicating a higher degree of mesoporosity.

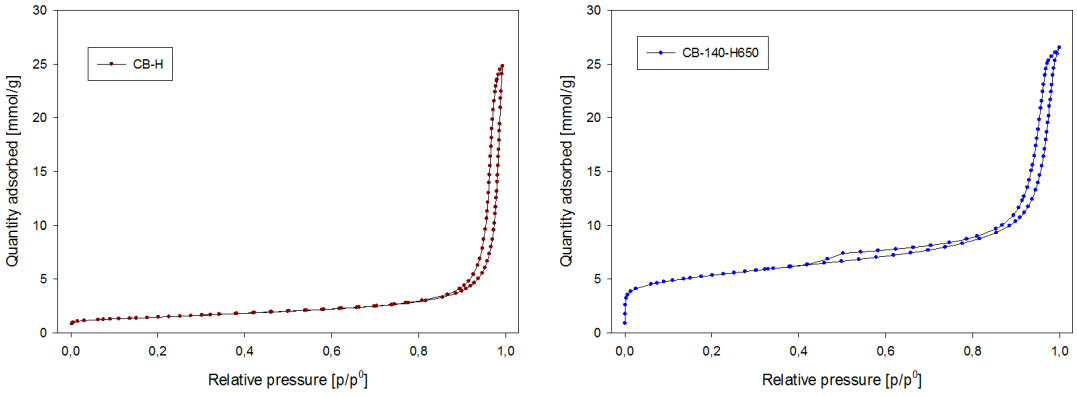

(a) **(b)**

Figure 5.2: Nitrogen adsorption-desorption isotherms showing the different isotherm profiles between (a) CB-H and (b) CB-140-H650.

STEM micrographs give more insight into the structural changes that have taken place during synthesis as can be seen in Figure 5.3. Figure 5.3a shows the reference support that was heated in a reducing atmosphere (CB-H), while Figure 5.3b shows CB-140-H650. The images both show carbon black agglomerates, but in Figure 5.3b it is clear that there is a darker circle around the perimeter of the primary particle. The electron micrographs and the shape of the hysteresis are similar to the data presented by Shi et al.[21] and Tang et al.[35] showing carbon black hollowed out by nitric acid. This suggests that CB-140-H650 has been oxidized from the inside out, instead of through a shrinking core mechanism. Amorphous carbon is more easily oxidized, and the center of the carbon black primary particles are known to be more amorphous than the carbon layers close to the surface [21, 36]. None of the other samples exhibited a hollow structure, presumably because the oxidation procedures were less invasive. Carbon black particles are nonporous, so it is likely that the acid treatment first creates microporous structures in the particles, subsequently oxidizing the carbon from within when the nitric acid can reach the center.

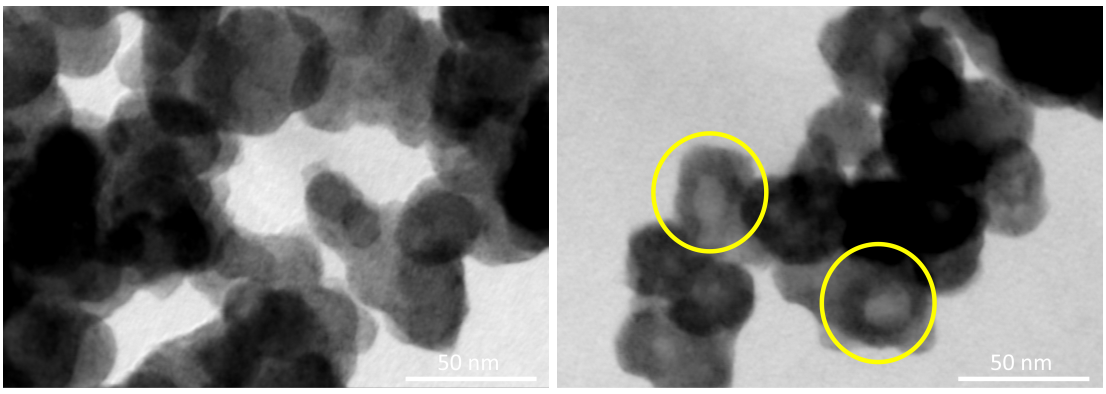

(a) **(b)**

Figure 5.3: STEM micrographs showing the difference in structure of (a) CB-H and (b) CB-140-H650.

The structural properties of the support materials were assessed with Raman spectroscopy. Figure 5.4 shows the Raman spectrum of CB-H. The spectrum is fitted according to a

suggested method by Mallet-Ladeira et al.[103]. Details about the fitting of the data can be found in Appendix C. The two peaks, D and G band, are found in all carbon materials. The D band is caused by a breathing mode that stems from defects in the sp^2 carbon matrix [105]. Perfect graphite does not allow for this vibrational mode as it is symmetry forbidden. The D band gives information about the degree of aromatic rings in the system as well as the presence of defects. Here the D peak is deconvoluted to D1 and D2 [103]. The presence of a D' band is not always necessary to adjust the shape of the G band. Mallet-Ladeira et al.[103] found experimentally that when the crystallite size is smaller than 10 nm, the D' band does not exist as it merges completely with the G band. The G peak is caused by bond stretching of all pairs of sp^2 atoms in rings and chains and can be found in all carbon structures.

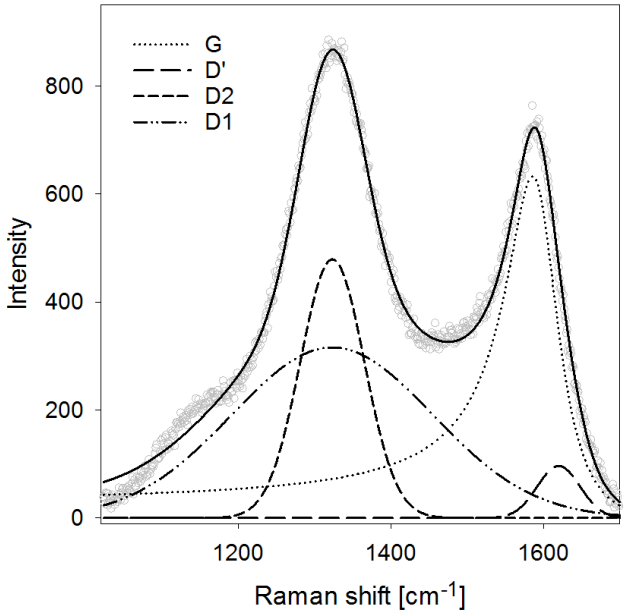

Figure 5.4: Raman spectrum of CB-H

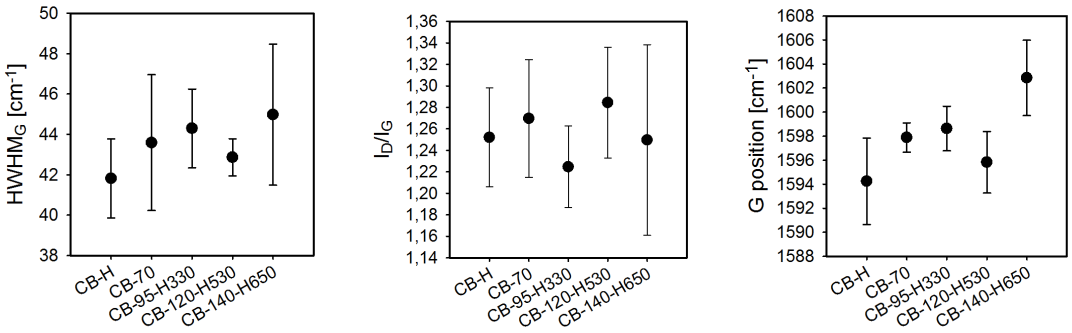

(a) **(b)** **(c)**

Figure 5.5: (a) HWHM of the G peak, (b) ID/IG ratio, and (c) G peak position for all the catalyst supports.

Three parameters are commonly used to evaluate the crystallinity of carbon. The intensity ratio between the D and G peaks, the position of the G peak, and the half width at half maximum of the G peak. Each sample was measured five times, and the error bars indicate the heterogeneity of the samples. The $HWHM_G$ gives a measure of the disorder in the sample and increases with an increased degree of disorder [105]. According to the Tunistra and Koening's law there relationship between the ID/IG ratio and the crystallite size is inversely linear [106]. This means that a higher ID/IG ratio generally means a smaller crystallite size. The position of the G peak also gives information on crystallinity. In general, the average G peak position moves from ca. 1580 cm^{-1} for perfect graphite to 1600 cm^{-1} for nanocrystallite sp^2 hybridized carbon. The data presented in Figure 5.5 shows that the samples overall retain a very similar crystallographic structure after the acid and heat treatment.

5.1.2 Oxygen functionalization

The changes in surface chemistry that were induced by the oxidation and heat treatments were assessed with TPD and XPS. The overall mass loss from chemisorbed species measured by TGA is presented in Table 5.2 together with surface oxygen content obtained from XPS. The TGA measurements were carried out in an inert atmosphere with a temperature ramp from 100 to 1000°C. The weight loss measured in the TGA includes the weight of carbon, as the oxygen groups decompose as CO and CO_2. The mass losses are in the same range and indicate that there is similar oxygen content on the carbon surfaces. The reference sample CB-H has a small mass loss compared to the other samples, indicating that the heat treatment in hydrogen successfully removed oxygen groups from the surface. The results vary slightly between the two methods. The XPS measurements seemingly show a decrease in total oxygen content for the samples with higher heat treatment temperatures. This can be seen in context with the increased porosity induced by the harsh acid and heat treatments. XPS is a surface-sensitive characterization method, while TGA gives access to information about the bulk material. Oxygen located inside of pores would therefore not be measured by XPS. These differences in the availability of information between the methods can be part of the explanation of the differences between the obtained data. The opposite is seen for CB-H, where the XPS measurement is substantially higher than what is expected from the mass loss measured from the decomposed groups. Overall one can see that the functionalization resulted in a somewhat similar oxygen loading for each support material, except the reference CB-H, which from the TGA data can be assumed to have a minimal concentration of oxygen groups on the surface.

Table 5.2: The mass loss from TGA measurements and surface oxygen content from XPS measurements for all support materials.

	Mass loss from chemisorbed species [wt%]	Surface oxygen content [at%]
CB-H	0.5	5.3
CB-70	5.1	8.0
CB-95-H330	4.6	6.2
CB-120-H530	5.6	6.2
CB-140-H650	4.5	4.4

The mass loss in the TGA was detected from 100 to 1000°C, and the curves presented in Figure 5.6 show at what temperatures the mass loss took place. The mass loss is correlated to the nature of the functional groups that are present at the surface. As discussed previously CB-H loses very little mass. The mass of CB-70 starts to decline almost immediately after heating, which suggests the presence of groups with a low decomposition temperature. The mass loss continues until 1000°C. CB-95-H330, CB-120-H530, and CB-140-H650 keep a stable weight initially, but eventually the graphs show a decrease in mass. As these samples already have been treated at higher temperatures, the groups that were initially present on the surface have already been decomposed, and therefore there are few groups with desorption temperatures below the heat treatment temperature remaining that would cause a mass loss. While the heat treatment temperature determines the temperature where the mass loss begins, the slope of the part of the curve showing the decreasing mass is determined by the concentration of groups with similar decomposition temperatures.

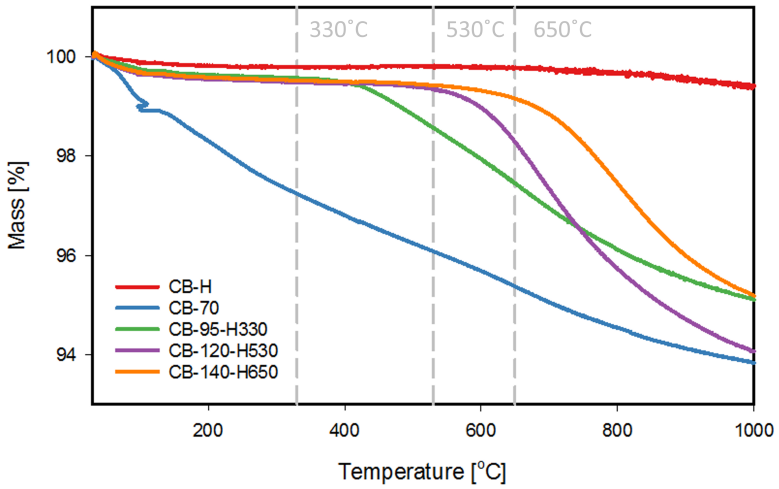

Figure 5.6: Mass loss curves from the TGA. The dashed lines indicate the heat treatment temperatures.

Figure 5.7 shows CO and CO_2 emissions from CB-70 during a TPD measurement with a constant temperature ramp from 100 to 1000°C in an inert atmosphere. This sample was not heat treated, and the emissions therefore stem from the full array of oxygen groups that were introduced to the surface through acid treatment. Each local maximum on the curves corresponds to the maximum intensity of the emissions from a certain group. Interpreting the emission curve can be difficult, as groups can have overlapping desorption energies. Overall there is a higher concentration of CO-emitting groups, which is in line with what is observed in literature on nitric acid functionalized carbon [42, 38]. It is worth noting however that nitric acid treatments lead to a higher concentration of CO_2 emitting groups than other oxidizing treatments such as air-oxidation [107, 38].

The heat treatment temperatures were determined based on TPD data obtained during the specialization project [14]. The decomposition temperatures of carboxylic acid derivatives are easier to separate than the CO emissions, therefore the heat treatment temperatures

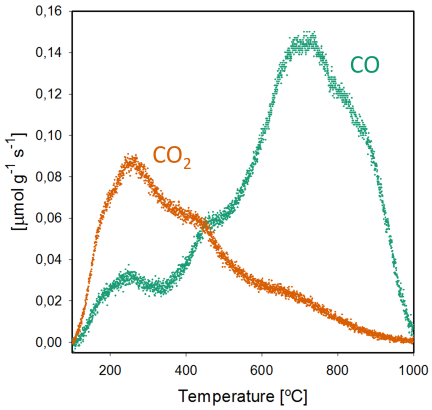

Figure 5.7: CO and CO_2 emissions from CB-70.

were determined from the deconvolution of the CO_2 emissions from a sample oxidized at 120°C. Figure 5.8 shows the changes in surface emissions during TPD for the different samples. The dashed lines indicate heat treatment temperatures.

The CO and CO_2 signals show that the heat treatments were successful in selectively removing surface species as the heat-treated samples have no or little emissions below their respective heat treatment temperature. As discussed previously, the intensity of the peaks increase for the samples with higher heat treatment temperatures, as the oxidation temperatures also were increased in order to maintain a similar oxidation degree for each sample. The combined area under the CO and CO_2 peaks for each sample should therefore be comparable.

The CO emitting groups are expected to be ethers, alcohols, ketones, aldehydes, and quinones, while the CO_2 emitting groups are carboxylic acids and carboxylic acid derivatives like carboxylic anhydrides and lactones [41]. The decomposition temperatures used to fit the data were assigned based on what has been reported in literature. It is possible to determine the adsorption temperature of different oxygen groups by using TPD, heat treatments, and other characterization methods such as XPS and titration. An example is how Otake and Jenkins [107] used linear TPD and selective neutralization to identify oxygen surface groups.

Figure 5.9 shows the deconvoluted TPD data for all the oxidized samples. The method used to fit the data is presented in Appendix A. The model is based on the notion that the groups desorb at different temperatures following a Gaussian distribution depending on the identity of the group, and the chemical environment it is in. As carbon black is paracrystalline, there are many different adsorption sites for the oxygen to bind to. A wide desorption peak indicates a wider array of different adsorption sites on the carbon. As all the carbon supports were made from the same carbon black, it is expected that the desorption ranges are similar for each support. The peak width was also kept in the same range for each species, as it is the carbon backbone that determines the width of the desorption range. The position of the peak maximum was kept similar for each support to assure the curves described the same species in each sample.

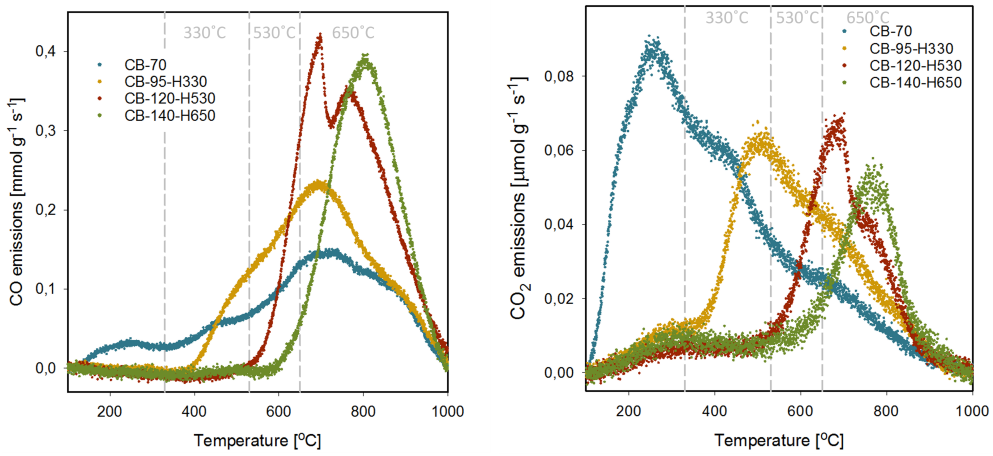

Figure 5.8: (a) CO and (b) CO_2 emissions for each oxidized support material. CB-H is not included here, as there were no detectable emissions from this sample.

The heat treatment temperature is indicated with a dashed line. The heat treatments removed virtually all CO-emitting groups, while some residual carboxylic acid and anhydrides are still present on the surface after heat treatment. This can be caused by the re-adsorption of oxygen when the samples were exposed to air at ambient temperature after heat treatment [47, 48]. Two types of lactones were assumed to be present on the surface, namely on zigzag and armchair edges. The difference in decomposition temperature stems from the difference in ring strain in the two types of lactones [45]. In reality, more complicated edge structures could also result in lactones with different decomposition temperatures, but these are assumed to be part of the Gaussian-shaped desorption temperature distribution of lactones I and II depending on their structure.

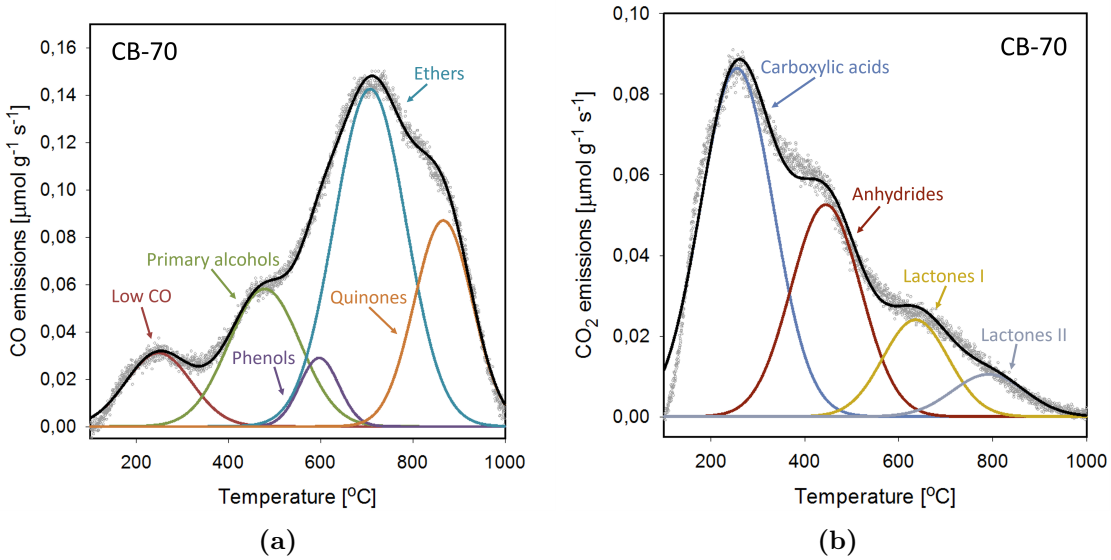

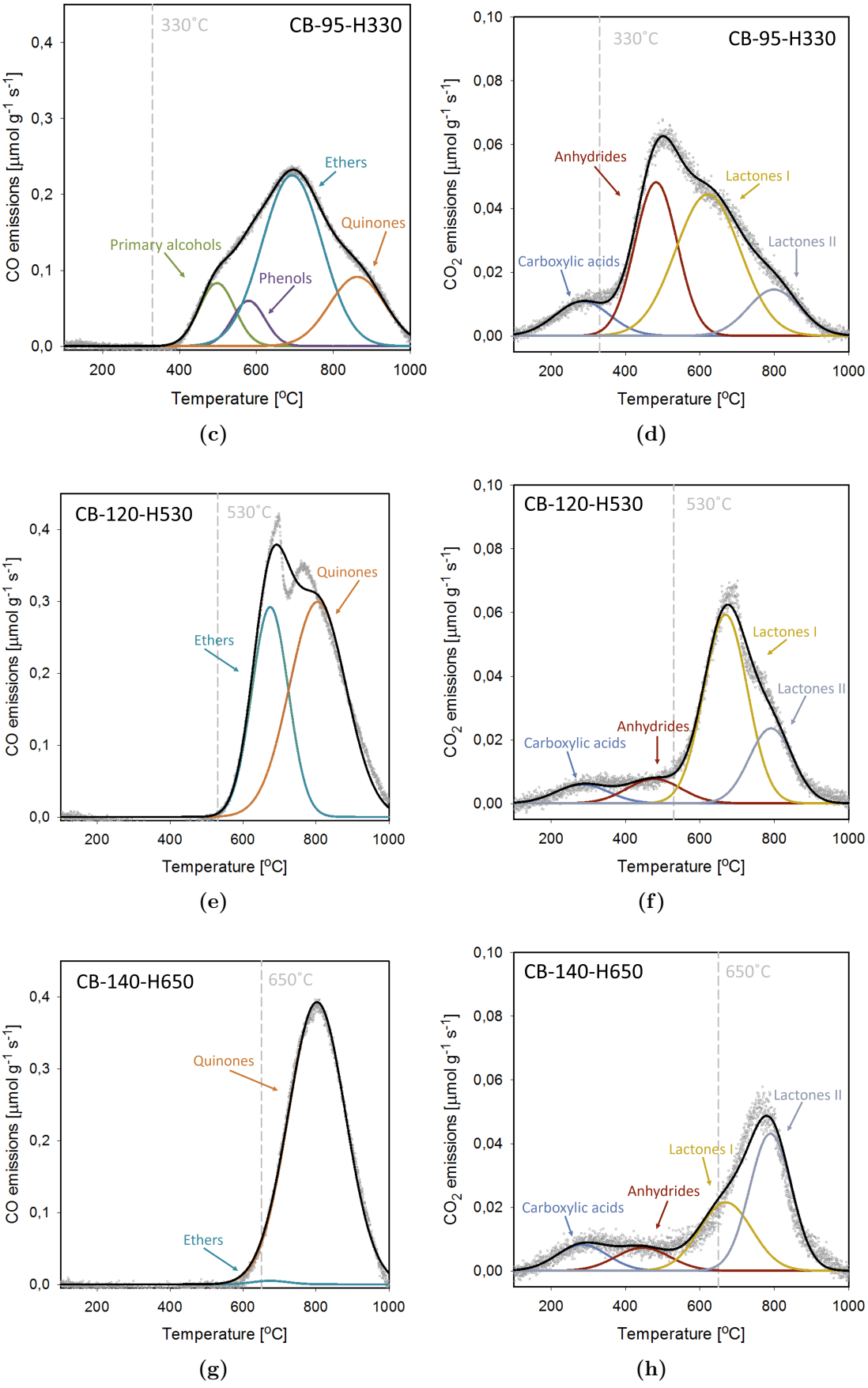

Figure 5.9: Deconvoluted TPD signals from CO and CO_2 emissions.

The parameters used to fit the curves make for a good fit in most cases. The CO emissions from CB-120-H530 deviate most from the Gaussian distribution used as a model. Although a better fit for these data could be obtained, the limits for the parameters were kept the same for all samples in order to correlate the Gaussian distributions to the physical phenomenon they describe as discussed previously. An explanation for the narrow peak seen in CB-120-H530 could be that part of the ether groups have been decomposed during the heat treatment prior to TPD measurement, and there are only the ethers that decompose at higher temperatures left. Apart from for CB-120-H530, the model used to fit the TPD data gives an accurate representation of the total emissions, and the deconvoluted peaks were therefore used to quantify the abundance of different groups on the surface of the carbon. Surface reactions were not taken into account for the quantification.

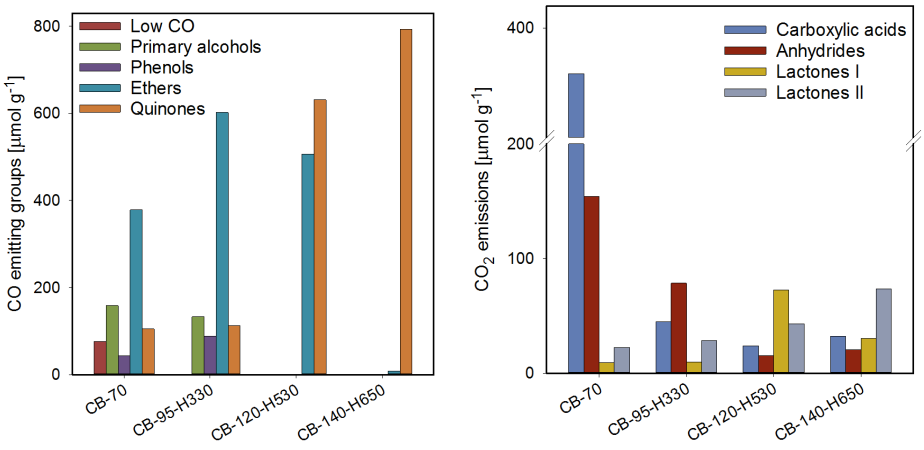

Figure 5.10: Quantification of (a) CO and (b) CO_2 emitting groups from the deconvolution of the TPD data from all the oxidized supports.

Figure 5.10 shows the amount of oxygen functional groups on the carbon per gram sample. From the bar diagram, it is clear how the groups get eliminated from the surface with increasing heat treatment temperature as the samples that were treated at high temperatures have progressively fewer different groups on the surface.

XPS was used in addition to TPD to identify the oxygen surface groups on the carbon. XPS probes binding energies of electrons of surface atoms. Deconvoluted spectra of the C 1s and O 1s orbital measured from CB-70 can be seen in Figure 5.11. The binding energies in the C 1s spectrum can be attributed to oxygen in phenols and ethers (C-O), ketones and quinones (C=O), and carboxylic acid, carboxylic anhydrides, and esters (-COO) [30]. The peak marked with $\pi \rightarrow \pi^*$ is referred to as the shakeup line and stems from aromatic compounds. The O 1s spectra are commonly divided into two peaks, oxygen bound with a double and a single bond to carbon. Quinones, ketones, and aldehydes have a double bond while ethers and phenols have single bonds. Carboxylic acids, anhydrides, and lactones contribute to both peaks as they contain both oxygen bound by a single and double bond to carbon. More details about the fitting of the XPS data can be found in Appendix B.

Quantification of the surface groups for all the samples is presented in Figure 5.12. It can be difficult to interpret data from XPS spectra as several of the groups have similar bond

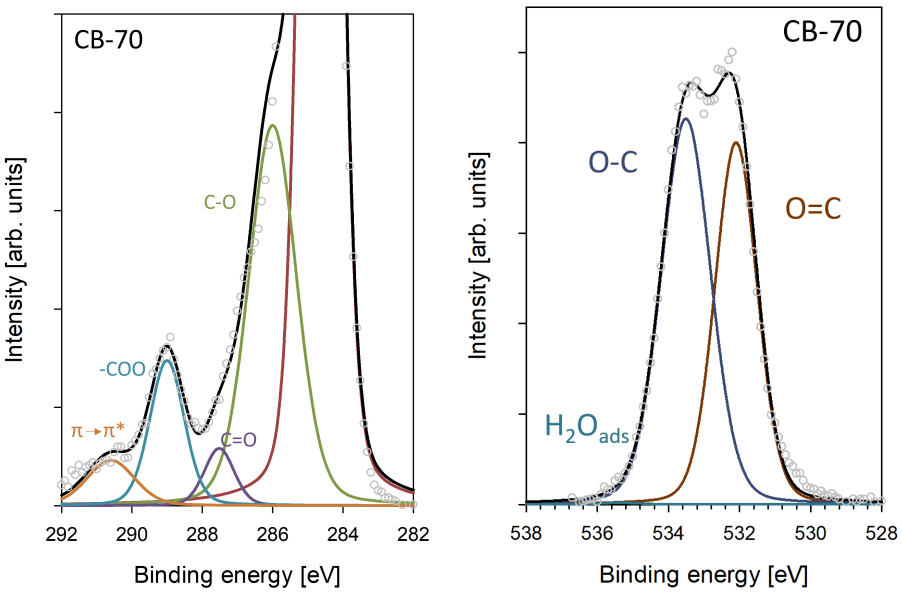

(a) **(b)**

Figure 5.11: (a) Deconvoluted C 1s orbital. (b) Deconvoluted O 1s orbital.

structures. The y-axis is given in %, as the bars represent how much of the oxygen on the surface is bound in the respective ways. The data from the C 1s orbital is therefore normalized with respect to the total amount of oxygen bonds.

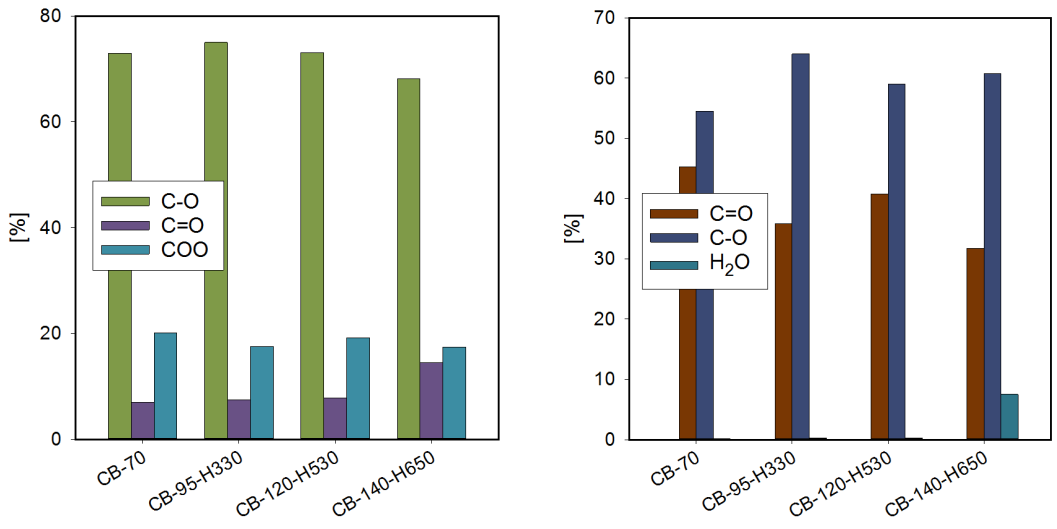

(a) **(b)**

Figure 5.12: Quantification of the bonds in the (a) C 1s orbital, and (b) O 1s orbital.

The first groups to decompose are carboxylic acids, which show up as COO in the C 1s spectra and as C=O and C-O in the O 1s spectra. From Figure 5.12 one can see that there is a slight decline in the bar showing COO bonds, and for the O 1 s orbital the most

obvious change is in the decrease of C=O bonds. During heat treatment at 530°C hydroxyl groups and carboxylic anhydrides decompose. This can be seen as a slight decrease in the C-O bond for both orbitals. The heat treatment at 650°C mainly removes ether groups, and this is visible as an additional decrease in the C-O bonds in the C 1s orbital, as well as an increase in C=O bonds. Comparing the quantification of the XPS results with the TPD measurements it is clear that there are some discrepancies. The low occurrence of C=O bonds in the XPS spectra is especially conspicuous. Both CB-120-H530 and CB-140-H650 have a high content of quinones on the surface according to the TPD curves. It is therefore expected that C=O bonds would be more prevalent in the quantification of surface groups from XPS. As mentioned previously, XPS is a surface-sensitive characterization method. The difference in group distribution between the two methods can be correlated to the location of the adsorption sites of the different groups. The conditions of the analysis were also completely different. During XPS the surface is probed at room temperature, while TPD uses elevated temperature to assess the oxygen groups. Surface reactions between groups or between species in the gas phase and on the surface can alter the carbon surface chemistry during heating.

5.2 Fresh catalyst

The catalysts were made by depositing pre-synthesized CoO nanoparticles on the carbon black supports after oxidation and heat treatments. The nanoparticles were made as part of the specialization project [14]. All data that is presented about the particles before deposition was collected prior to starting the thesis and some of the nanoparticle characterization is included here to show the changes in the particles before and after deposition. Figure 5.13a shows an electron micrograph of the spherical nanoparticles, while 5.13b shows the particle size distribution of the nanoparticles in dispersion.

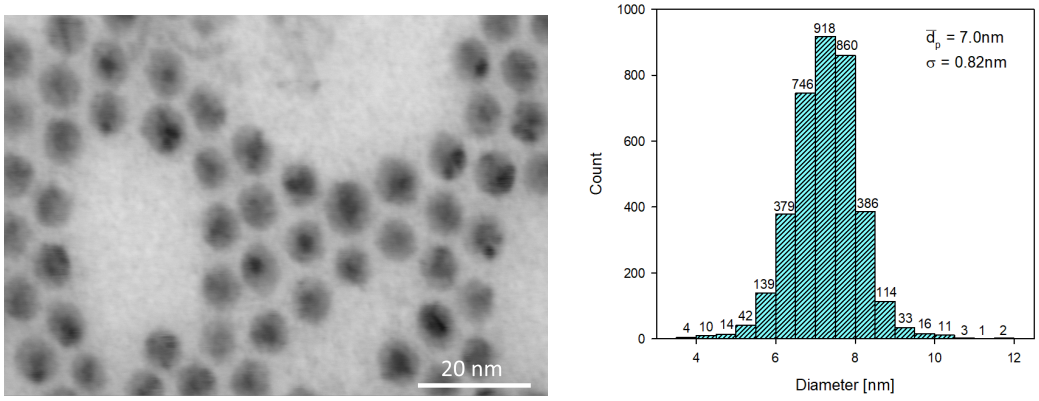

(a) **(b)**

Figure 5.13: (a) STEM micrograph of the cobalt nanoparticles before deposition. The STEM image was taken with an accelerating voltage of 30kV, and an emission current of 10μA. (b) The particle size distribution of the particles before deposition onto the support material. From [14].

Figure 5.14 shows Co/CB-70 after deposition of the cobalt nanoparticles. From STEM

images of all the catalysts it was clear that the nanoparticles were well dispersed on the surface, and that the particles had kept their spherical shape. The particle size of the cobalt nanoparticles can be found in Table 5.3. The mean diameter in Figure 5.13b is the size of CoO nanoparticles, while the diameters of the deposited particles are given as metallic cobalt, assumed to be 75% of the cobalt oxide size. The nanoparticles in solution were measured with ImageJ, while it was not possible to employ this method for the deposited particles. The deposited particles were therefore measured manually using DF-STEM images. The change of method can have led to small differences in the measured particle size, but overall the particles seem to have kept their size intact after deposition.

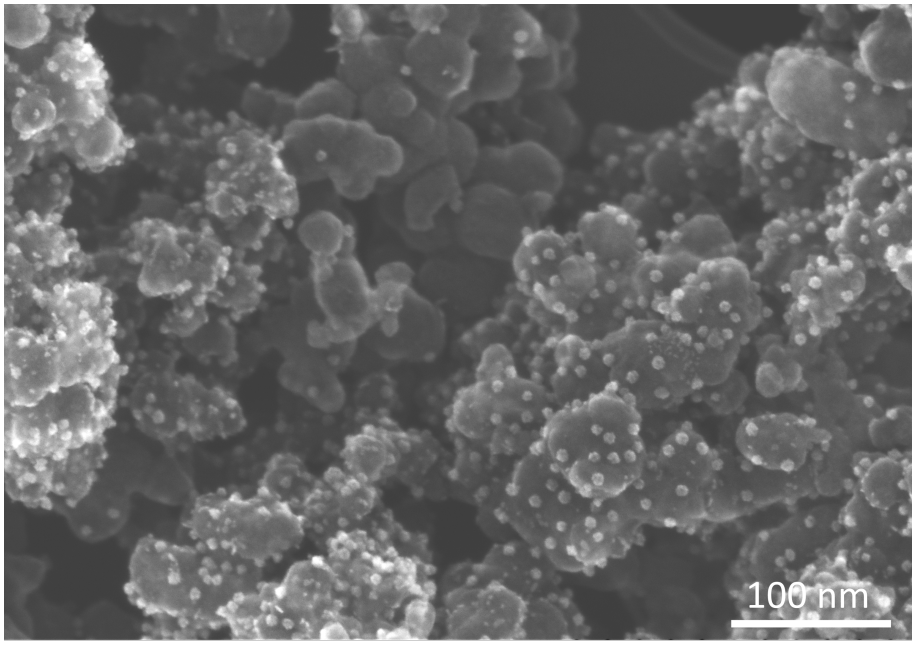

Figure 5.14: STEM micrograph showing the cobalt nanoparticles deposited on carbon black for Co/CB-70. The STEM image was taken with an accelerating voltage of 30kV, and an emission current of 10μA.

The cobalt loading was measured with MP-AES, and the results are presented in Table 5.3. The cobalt content for each sample is similar, and together with STEM images, it proves that the deposition of pre-synthesized nanoparticles was successful and yielded catalysts with a similar loading and a similar particle size. The biggest advantage of preparing the catalyst in this way as opposed to using incipient wetness impregnation or another impregnation method with a cobalt salt is that there is no need for a calcination step, which provides more control over the particle size and uniformity. This is especially important when creating model systems to study specific properties of the catalyst. Using the pre-synthesized particles allows for the investigation of the influence of oxygen functional groups on the behavior of the catalyst with a similar starting point in terms of particle size and dispersion for all the catalysts.

XRD of the fresh catalysts can be seen in Figure 5.15. The peak at 15°originates from the Kapton foil, while peaks at 25°and 43°can be assigned to the carbon (002) and (101) reflex respectively. The three peaks marked on the Co/CB-H spectrum confirm that the cobalt particles were indeed CoO. These peaks correspond to the (111), (200), and (220) reflexes. The peaks are broad, indicating small particles. It is possible to find the average particle

Table 5.3: The cobalt loading and average particle size of the fresh catalyst.

	Cobalt loading [wt%]	$\bar{d}_{fresh}$ [nm]
Co/CB-H	6.6	5.1
Co/CB-70	6.9	5.2
Co/CB-95-H330	6.9	5.3
Co/CB-120-H530	6.9	5.4
Co/CB-140-H650	6.7	4.6

size from XRD measurements using the Scherrer equation, however, as the broadness of the reflexes indicates a crystallite size close to or equal the detection limit of around 4 nm, the particle size was only determined from STEM images. There are no notable differences between the fresh catalysts visible in the XRD spectra. This is expected as the particle size was similar, and the cobalt nanoparticles maintained the same oxidation state after deposition.

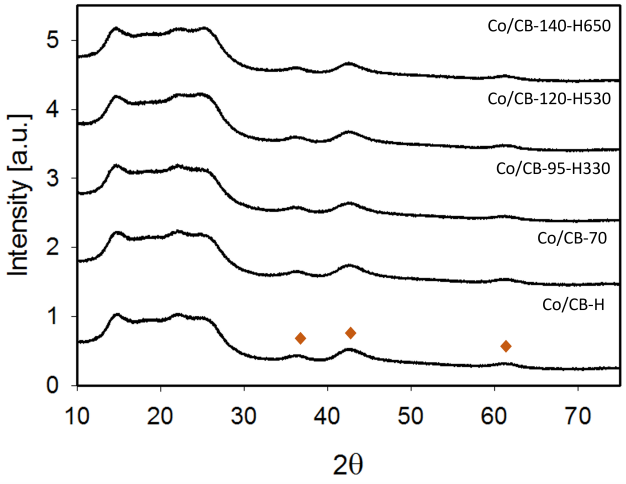

Figure 5.15: XRD measurements of the fresh catalysts. (◇) CoO

5.3 Reduced catalyst

TPR experiments were executed to determine the reduction temperature, and the degree of reduction (DOR) for all the catalysts. Figure 5.16 shows the hydrogen consumption during TPR. The graphs are normalized with respect to the cobalt content in each sample. The reduction temperatures can be found in Table 5.4. All of the catalysts show a sharp peak assigned to the reduction of CoO to Co^0. The second peak evolving at around 600°C is attributed to carbon gasification, possibly catalyzed by the cobalt particles[66]. Reduction of oxygen surface groups remaining on the surface after deposition likely also takes place, but this can not be seen from the TPR data [44].

Co/CB-H has the lowest reduction temperature and the highest hydrogen consumption. The increased heat treatments consistently shift the reduction peak towards higher temperatures, except for Co/CB-140-H650 which is shifted slightly to the left. Many authors

have reported a lower reduction temperature for catalysts with oxidized supports [32, 68, 84, 81]. These papers, however, report a two-step reduction from Co_3O_4 to CoO, and further to Co^0. Impregnation and calcination routines were implemented to synthesize the catalysts. The nanoparticles used here were subject to a low-temperature oxidation after the particle formation, yielding CoO [13]. In contrast to what others have reported, van Deelen et al.[66] found a higher reduction temperature for oxygen-functionalized supports using the same nanoparticle synthesis and deposition as used in this thesis. This was attributed to increased metal-support interactions between the oxidized support and the cobalt.

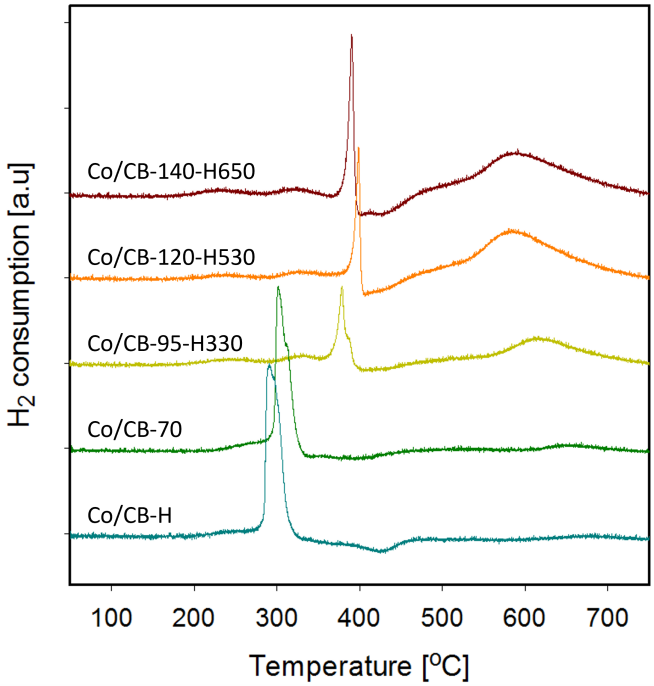

Figure 5.16: TPR profiles of the catalysts.

Table 5.4 shows the degree of reduction of all the catalysts. The DOR was calculated with the integral of the TPR peaks, and assuming all the cobalt in Co/CB-H was completely reduced. The implications of the DOR are however not so straightforward. It is not possible to say whether the reduction takes place following a shrinking core model with the remaining cobalt oxide being at the center of the particles, or if certain particles are not reduced at all. The difference between the two mechanisms is quite large, as this determines how much metallic cobalt is available to the reactants on the surface during synthesis.

The particle size after reduction can be found in Table 5.5. As can be seen, the particle size has increased for all the catalysts during reduction, but the most severe sintering has taken place on Co/CB-H. The average particle size has doubled after the reduction, indicating low metal-support interactions. This is in line with what is reported in literature, namely that oxygen groups act as anchoring sites for the nanoparticles which in turn hampers particle growth during reduction compared to non-functionalized supports [27, 68]. The sintering on the oxidized supports happens following this order: Co/CB-70 < Co/CB-95-

Table 5.4: Reduction data from TPR studies. The reduction temperature was taken to be the temperature at the peak maximum.

	Degree of reduction [%]	Reduction temperature [°C]
Co/CB-H	100	290
Co/CB-70	77	301
Co/CB-95-H330	27	378
Co/CB-120-H530	26	399
Co/CB-140-H650	29	390

H330 < Co/CB-120-H530 < Co/CB-140-H650, where Co/CB-70 has the smallest particles, and Co/CB-140-H650 has the largest. Correlating this to the surface chemistry can be difficult, as it is not entirely clear which surface groups are still present on the surface during reduction. Still, the catalyst with carbon that was functionalized with carboxylic acids (CB-70) shows very little sintering, which indicates that carboxylic acids are good anchoring sites. Carboxylic anhydrides and alcohols also seem to be good anchoring sites, although not as good as carboxylic acids. Ethers, quinones, and lactones also immobilize the metal to a certain degree, but not as efficiently as the other groups. Interestingly, an increase in surface defects does not seem to have a large contribution to the immobilization of the cobalt nanoparticles. Chernyak et al.[32] propose unsaturated carbons on defect sites to be the main immobilization agent, but as there is no decrease in particle size with increased surface area, it can be concluded that this effect is secondary to the influence of the oxygen groups.

Table 5.5: Mean diameter of cobalt particles on the reduced catalysts, and the difference in particle size between the fresh and the reduced catalyst.

	$\bar{d}_{reduced}$ [nm]	Particle size difference [nm]
Co/CB-H	11.5	6.4
Co/CB-70	6.3	1.1
Co/CB-95-H330	6.7	1.4
Co/CB-120-H530	7.5	2.1
Co/CB-140-H650	8.2	3.6

XRD measurements of the reduced catalysts presented in Figure 5.17 were able to give insight into the crystallographic structure of the metallic cobalt for Co/CB-H. Presumably, the other catalysts had particles that were so small that the passivation layer makes up most of the particles, and the metallic cobalt phase was therefore not measurable. Three diffraction reflections are observed from the X-ray diffractogram of Co/CB-H at 42°, 45°, and 47°, and can be assigned to the (100), (002), and (101) of hexagonal close packed (hcp) metallic cobalt respectively. Hcp is deemed to be the most active crystallographic structure for FT synthesis [54, 53].

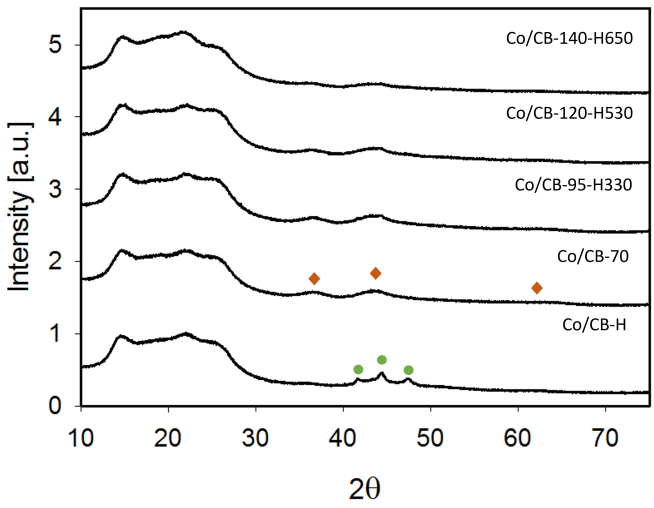

Figure 5.17: X-ray diffractograms of the reduced catalysts. (⋄) CoO, (○) hcp Co ^{0}.

5.4 Catalytic testing

The CTY and CO conversion from the FT synthesis is displayed in Figure 5.18. There were some interruptions during activity testing, but due to time limitations, it was not possible to repeat the experiments. The interruptions are visible in the graph as gaps between the data points. Although some data is missing, it is still possible to use the data sets to evaluate the performance of each catalyst. The activity and selectivity data are summarized in Table 5.6. The selectivity data presented was calculated at the CO conversion listed in the table, which is where the activity had stabilized, right before the first increase in temperature after 77 h on stream.

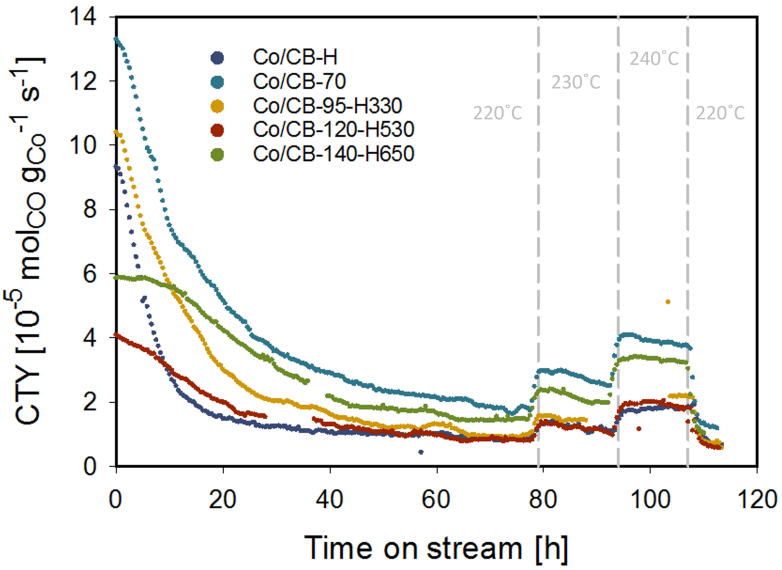

Figure 5.18: Cobalt time yield from the activity testing of the catalysts. The dashed lines show when the temperature was changed. p = 20 bar, $p_{H_2}/p_{CO} = 2$.

Table 5.6: Summary of activity and selectivity data from the FT synthesis experiments. X_{CO} Denotes the CO conversion where the selectivities were measured, at 77 h on stream. STY is the site time yield, and the subscripts i and f denotes *initial* and *final* respectively corresponding to 0 and 112 h on stream.

	X_{CO} [%]	S_{CH_4} [%]	S_{C5+}[%]	STY_i [$10^{-3}s^{-1}$]	STY_f [$10^{-3}s^{-1}$]
Co/CB-H	4.3	30	62	63	6
Co/CB-70	9.4	28	63	49	5
Co/CB-95-H330	5.0	28	64	41	4
Co/CB-120-H530	4.2	29	61	18	4
Co/CB-140-H650	7.7	23	68	30	8

The change in cobalt surface area and activity can be seen in Table 5.4. The change in area was calculated from the difference in particle size after reduction and after synthesis, and the activity loss was calculated from the change in conversion. Both the surface area loss and the initial STY compared to the DOR are shown in Figure 5.20. If sintering is the main deactivation mechanism then the change in activity should be comparable with the change in surface area. However, FT synthesis is a structure-sensitive reaction that is dependent on specific geometric configurations on the cobalt particles. It is therefore not a given that the occurrence of such sites is linearly dependent on the surface area. Quite the opposite, it has been found that larger particles most likely have a higher occurrence of such sites on the surface, although this effect tapers off for particles larger than 6nm [59]. In this case, all catalysts have average particle sizes above a diameter of 6 nm, and the activity can therefore be correlated to the total cobalt surface area.

Table 5.7: The loss in surface area and conversion of all the catalysts.

	Cobalt surface area loss [%]	Activity loss [%]
Co/CB-H	22	93
Co/CB-70	8	91
Co/CB-95-H330	40	94
Co/CB-120-H530	30	86
Co/CB-140-H650	38	82

As is displayed in Figure 5.18, there are two general shapes to the curves that can be observed from the data. Co/CB-H, Co/CB-70, and Co/CB-H330 have a high initial activity that rapidly drops within the first few hours of the catalytic testing. Co/CB-120-H530 and Co/CB-140-H650 have much lower initial activity, but the deactivation is not as rapid as for the other catalysts. Co/CB-70 and Co/CB-140-H650 have the highest CTY after the initial deactivation period at around 20 h on stream. The other three catalysts have a similar CTY both right before the initial increase in temperature and after returning to 220°C. From Table 5.6 one can see that the selectivity is relatively similar for all the catalysts. It is however difficult to compare selectivity at different CO conversions, as a higher partial pressure of water leads to a higher production of C5+ compounds. As a consequence, the selectivity to C5+ products is improved at high conversions. The following sections will therefore focus on the activity and possible deactivation mechanisms for all catalysts, and not on the selectivity results.

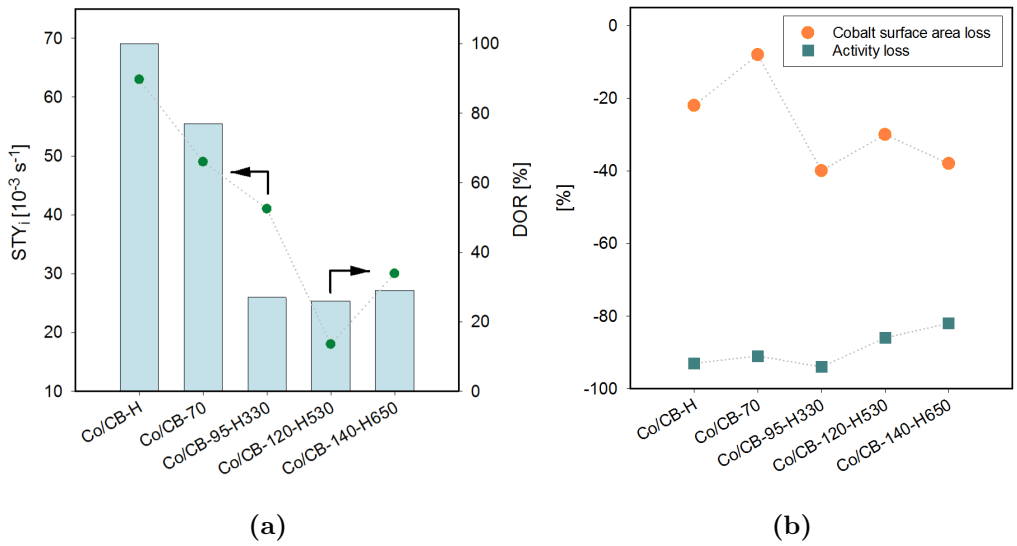

(a) **(b)**

Figure 5.19: (a) Initial site time yield compared to the initial degree of reduction calculated from TPR measurements. (b) Loss in activity compared to the loss in surface area for all catalysts.

5.4.1 Co/CB-H

Co/CB-H has a lower CTY than Co/CB-70 and Co/CB-95-H330, and it has the most rapid deactivation of all the catalysts. However, the STY$_i$ presented in Table 5.6 shows that it has the highest intrinsic activity. The XRD measurements show that the hcp phase was dominating in the particles after reduction. Hcp is known to be the most active cobalt phase for FT synthesis and van Deelen et al.[66] found that hcp was present in nanocrystals on unoxidized support, fcc was dominating in the cobalt on functionalized carbon by using in situ XRD measurements. Although a difference in crystallographic phase between the catalysts could be part of the explanation, it is difficult to say whether this is the cause of the superior initial STY, as there are no data available on the crystallographic phase of the other catalysts.

After exhibiting a high initial activity the catalyst rapidly deactivates. A high initial water pressure could facilitate particle growth, but the relatively small change in surface area shown in Figure 5.19b and the low STY$_f$ value show that the loss in activity cannot be explained exclusively by sintering of the nanoparticles [108]. The loss in surface area is 22%, which is not enough to justify an activity drop of 93%. Interestingly, the particle size of Co/CB-H increased the most during reduction compared to the other catalysts, but surface loss during the reaction is relatively low. There is reason to believe that the particle growth mainly took place at the beginning of the synthesis, as most of the deactivation takes place during the first 10 h on stream. With a high initial conversion, it is possible that the partial pressure of water is high enough to re-oxidize the particles. This mechanism is however most common for smaller particles (below 4.4 nm) that are easier to oxidize [109]. The TPR measurements also showed that Co/CB-H is the easiest catalyst to reduce out of the tested catalysts.

The activity before and after the increase in temperature is quite similar. Both sintering

and re-oxidation increase with high partial pressure of water. The activity is slightly higher at higher temperatures, but not enough to see a significant deactivation as a consequence of the water content. This could speak in favor of re-oxidation as the main deactivation mechanism, as sintering would worsen at higher temperatures regardless of the partial pressure of water in the reactor.

5.4.2 Co/CB-70

Co/CB-70 has the highest CTY throughout the testing, but the STY_i is slightly lower than for Co/CB-H. The reason can be found by comparing the DOR of the two catalysts with the STY_i as seen in Figure 5.19a. The unreduced cobalt is likely to be causing the lower initial site time yield. That, however, requires assuming the unreduced cobalt is at the surface of the particles. If this is the case, the DOR could provide the explanation for a lower STY_i.

Similarly to Co/CB-H, the activity of the catalyst declines rapidly. The loss in surface area is very little, as can be seen in Figure 5.19b. Sintering can therefore not explain the activity loss. This shows that the presence of carboxylic acids on the carbon support surface not only prevents sintering during reduction but also during the reaction. Co/CB-70 had the second lowest reduction temperature measured with TPR, but since the particles are relatively small, re-oxidation may be a viable deactivation mechanism for this catalyst. As for Co/CB-H, the fast initial deactivation coincides with high initial conversion levels in the beginning.

5.4.3 Co/CB-95-H330

The CTY data from Co/CB-95-H330 has a similar slope to the data from Co/CB-70, but the overall activity is slightly lower. From Figure 5.19a one can see that the initial DOR of this catalyst was significantly lower than for Co/CB-70, which could explain the lower initial activity. Compared to the STY_i of Co/CB-120-H530 and Co/CB-140-H650 which have similar DOR values, the initial activity is quite high.

Figure 5.19b shows that the surface area loss during the reaction is significant compared to Co/CB-70 while the change in activity is relatively similar. This could mean that the main deactivation mechanism is sintering, but it seems unlikely that Co/CB-70 and Co/CB-95-H330 would suffer from different deactivation mechanisms as their CTY profiles are so similar. The decrease in STY presented in Table 5.6 shows that there must be an additional deactivation mechanism at play. This could possibly be re-oxidation of the cobalt particles, which can be seen in context with the loss in surface area. Co/CB-95-H330 has the largest loss in surface area, namely 40%. The change in particle size during reduction however was negligible. Cobalt particles that are re-oxidized have been found to induce sintering [110]. This could provide an explanation as to why the slopes are so similar between Co/CB-70 and Co/CB-95-H330. Deactivation in both catalysts could be caused by re-oxidation caused by the high partial pressure of water at high conversions, but for Co/CB-95-H330 it is possible that the oxidized particles sinter and cause a loss in surface area. This mechanism would however be secondary to explaining the deactivation.

Relating this to the surface groups is challenging, as it is not clear which groups are still on the surface after reduction. If sintering of oxidized cobalt is happening on Co/CB-95-H330, but not on Co/CB-70 it could be caused by the carboxylic acid groups acting as anchoring sites both for metallic cobalt and oxidized cobalt, while the absence of this group causes the oxidized cobalt to sinter. It is however doubtful that groups with such a low desorption temperatures would survive on the surface during reduction conditions. The TPD measurements showed that most of the carboxylic acid groups on the carbon surface had decomposed before 330°C. The difference could therefore possibly be in the strength of the initial anchoring.

5.4.4 Co/CB-120-H530

Co/CB-120-H530 has the lowest initial CTY and STY. The slope is quite different from the previously discussed catalysts. The slope becomes steeper with time before it levels off at around 50 h on stream. Looking back on the mean particle diameter presented in Table 5.5, it is slightly bigger for Co/CB-120-H530 than the previous three catalysts. Although an increased particle size could explain the lower CTY, it does not explain the low STY_i. From Figure 5.19a one can see that the initial DOR is rather low, but compared to Co/CB-95-H330 the STY_i is much lower than expected. The low initial activity can therefore not be entirely explained by a low reduction degree. Co/CB-120-H530 may have fcc as dominating crystallographic phase as opposed to hcp which was measured for Co/CB-H. It was unfortunately not possible to obtain any data on the crystallographic structure of the metallic cobalt after reduction.

The deactivation mechanism also appears different than for the three previously discussed catalysts. The deactivation is slower, which could be caused by the lower partial pressure of water in the reactor as a consequence of the low initial activity. The support material used for this catalyst has a high abundance of ethers/carbonyls. Carbonyls have been shown to enhance hydrogen spillover by binding to the hydrogen, which could prevent re-oxidation of the particles [78]. The catalyst loses about 40% of its initial cobalt surface area, and the change in STY is the smallest for all of the catalysts. Sintering can therefore be pointed out as a plausible main deactivation mechanism. The loss in surface area during the reaction is however less severe than for Co/CB-95-330. As the particles sintered more for Co/CB-120-H530 than Co/CB-95-H330 during reduction it is hard to determine that the lower degree of sintering during the reaction is caused by a higher degree of certain oxygen groups. It may be likely that a lower degree of re-oxidation kept the particles less mobile which prevented an excessive surface area loss like what was seen on Co/CB-95-H330. The dominant groups on CB-120-H530 before deposition of cobalt particles were ethers, quinones, and lactones, while anhydrides and alcohols were additionally present on CB-95-H330. Comparing the two supports, there is a substantially higher concentration of ethers and quinones present on CB-120-H530. It could be possible that ethers act as good anchoring sites. Quinones are the most abundant surface species on CB-140-H650, where there is a higher degree of sintering, which means that they are probably not causing the immobilization on Co/CB-120-H530. As all of these functional groups have relatively high decomposition temperatures, therefore it is plausible that they are still present on the catalyst surface during synthesis.

5.4.5 Co/CB-140-H650

The CTY profile of Co/CB-140-H650 is very similar to Co/CB-120-H530, but Co/CB-140-H650 has a higher initial activity. Figure 5.19a shows that the degree of reduction of the two catalysts is very similar, still, Co/CB-140-H650 has a higher initial STY. This could be related to a slightly larger particle size. Bezemer et al.[59] found that the optimal particle size at 35 bar was 8 nm, while it was 6 nm at 1 bar indicating that the optimal particle size is slightly higher at elevated pressures. Co/CB-120-H530 has a mean particle size of 7.5 nm, and Co/CB-140-H650 has a mean particle size of 8.2. Although this difference is quite small, it could be part of the explanation for the higher initial activity. Regarding the deactivation mechanism, it is most likely driven by sintering, with a higher degree of surface loss than was observed for Co/CB-120-H530. Overall this catalyst had the least amount of deactivation.

5.5 Spent catalyst

The spent catalyst was characterized with XRD and STEM to determine the crystallite phase and particle size. The XRD measurement was challenging as SiC used as a dilutant to better heat transfer inside the reactor is a much more crystalline material than the catalyst, and therefore obstructed some of the peaks. Figure 5.20a shows part of the spectra where it was possible to identify the two cobalt phases. The peak at 42°stems from the (100) plane of hcp cobalt, but also from the (200) plane of SiC. Except for Co/CB-H, it is difficult to identify the phases as the crystallite domains in the particles are still too small to make a sharp peak in the spectrum. Most likely both phases are present in the particles. What can be seen from the data however is that Co/CB-H kept the hcp phase more or less intact during synthesis.

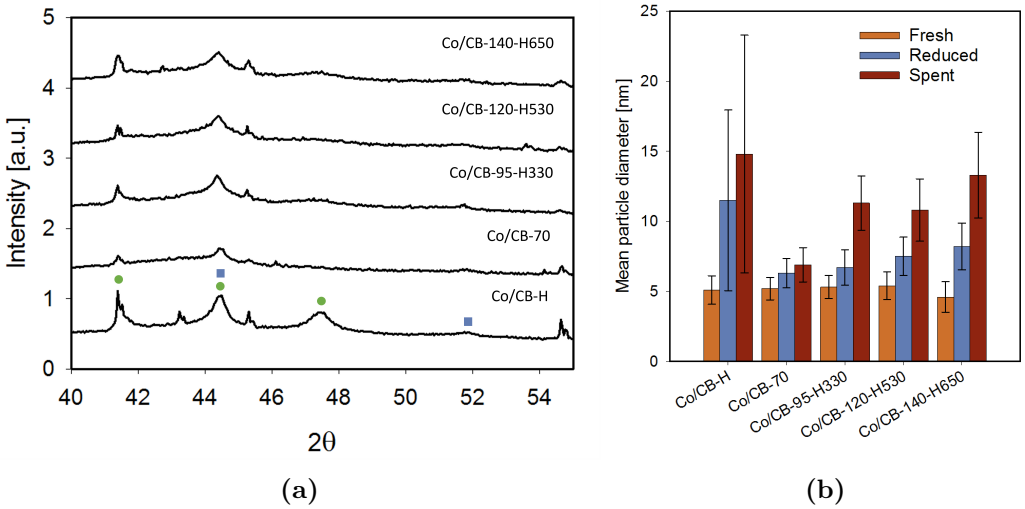

(a) **(b)**

Figure 5.20: (a) XRD measurements of the spent catalysts. (○) hcp cobalt, (□) fcc cobalt.(b) The mean particle size of the fresh, reduced, and spent catalysts.

Figure 5.20b shows the mean particle size for all the catalysts for fresh, reduced, and spent

samples as determined by STEM micrographs. Co/CB-H has the largest particles both after reduction and after reaction, but the sintering during the reaction is not as severe as the sintering that takes place during reduction. This could be explained by the rapid deactivation causing the partial pressure of water to be low in the reactor for most of the time on stream. This could have hampered the sintering as it is promoted by water [108]. Almost no particle growth can be measured on Co/CB-70 alluding to the importance of carboxylic acids when it comes to cobalt immobilization on the supports. Even with the highest CO conversion, and therefore a substantial degree of water in the reactor did almost no sintering occur. Co/CB-95-H330 did not sinter significantly during reduction, the particle growth during synthesis however is substantial, from 6.7 after reduction to 11.3 after catalytic testing. The possible explanations for this were discussed in detail in the previous section. Co/CB-120-H530 and Co/CB-140-H650 both sinter significantly during reduction and synthesis from 5.4 to 7.5 and 4.6 to 8.2 during reduction for the two catalysts respectively. The final particle size after the catalytic test was 10.8 for Co/CB-120-H530, and 13.3 for Co/CB-140-H650. The latter has a larger particle growth in both instances which could be related to the higher conversion.

Chapter 6

Conclusion

In this work, five different cobalt-based catalysts on carbon with varying surface oxygen functional groups were synthesized. The carbon support was oxidized with nitric acid to introduce functional groups to the surface. Subsequently, the groups were selectively desorbed by heat treatment. The result of the support functionalization was five different support materials with unique surface chemistry. The catalysts were characterized with STEM, nitrogen physisorption, Raman spectroscopy, TPD, TPR, XPS, XRD, and MP-AES. The catalytic tests took place in a tubular fixed bed reactor with a H_2/CO ratio of 2.1, p = 20 bar, and temperatures between 220 and 240°C.

The surface area increased significantly with increasing oxidation and heat treatment temperatures, from 114 m^2/g for CB-H, to 426 m^2/g for CB-140-H650. This was attributed to a roughening of the surface caused by the acid and heat treatments, and possibly the creation of pore structures in the carbon black primary particles. Data from TGA measurements indicated that the functionalized carbon samples had a similar overall oxygen content with a weight loss of 4.5-5.6 wt%. XPS measurements did not agree completely with the TGA results. The discrepancies were most likely caused by the increased porosity of the carbon exposed to harsh oxidation and heat treatment conditions during functionalization and defunctionalization, causing part of the oxygen groups to be unavailable to probing by XPS as it is a surface-sensitive characterization method. TPD measurements confirmed that the carbon was successfully oxidized and defunctionalized. CO and CO_2 emissions indicated that the heat treatments at different temperatures did subsequently remove oxygen groups as there was little gas emission at temperatures below the heat treatment temperatures the carbon had been subjected to. HR-XPS measurements also showed changes in surface chemistry.

The deposition of the cobalt nanoparticles yielded catalysts with cobalt loading of approximately 7wt%. The reference catalyst was most easily reduced, while the catalysts on oxidized supports had both higher reduction temperatures and a lower degree of reduction. Particle size measurements revealed that the particle growth was largest on the non-functionalized support, while the support that was not subjected to heat treatments had the lowest particle growth out of all the catalysts. The particle size after reduction and synthesis was 6.9 for Co/CB-70, while the particles grew to an average size of 14.8, 11.3, 10.8, and 13.3 nm for Co/CB-H, Co/CB-95-H330, Co/CB-120-H530, and Co/CB-140-

H650 respectively. It is possible that carboxylic acid groups, which were more abundant on the CB-70 support than in any other catalyst, are better anchoring sites than the other oxygen functional groups. Co/CB-70 had the highest CTY, while Co/CB-H had the highest STY, indicating that the intrinsic activity of Co/CB-H was superior to the catalysts on oxidized support, but the severe sintering led to an overall lower CO conversion over this catalyst. The difference in particle growth between the non-functionalized and the functionalized catalysts indicates that oxygen functional groups are important for the immobilization of metal particles on the surface. Carboxylic acid groups seem to play an especially important role, as there was significantly less sintering of the cobalt particles on Co/CB-70 compared to the other catalysts.

Chapter 7

Further work

The work presented in this thesis shows that there are significant differences in the performance of carbon supported cobalt catalysts for FT synthesis depending on the presence of different surface functional groups. In order to better understand what causes the differences between the selectively oxidized catalysts, further characterization is necessary. It would be useful to do additional XPS measurements after the nanoparticle deposition, to investigate which surface groups are still present after the catalyst synthesis. This could provide a better explanation for the differences in reduction behavior between the catalysts. In situ XPS measurements could also be used to investigate other metal-support interactions that could affect the performance of the catalyst, such as charge transfer.

As several studies have reported differences in crystallinity between the oxidized and unoxidized carbon supports, it would be interesting to do in situ XRD measurements in order to determine if there are differences in the crystalline phase of the cobalt nanoparticles induced by the different oxygen groups. This could provide an additional explanation of the differences in the initial activity other than differences in the degree of reduction.

By adding a second reduction to the catalytic testing, it would be possible to investigate whether the catalysts could regain some activity after the initial deactivation. If so, this would substantiate the claim that re-oxidation is one of the main deactivation mechanisms. In addition, HR-TEM could reveal whether there are carbonaceous deposits on the surface, which could also be a possible cause of deactivation.

Bibliography

[1] Zahra Gholami, Zdeněk Tišler and Vlastimil Rubáš. 'Recent advances in Fischer-Tropsch synthesis using cobalt-based catalysts: a review on supports, promoters, and reactors'. In: *Catalysis Reviews - Science and Engineering* 63.3 (2021), pp. 512–595. ISSN: 15205703. DOI: 10.1080/01614940.2020.1762367.

[2] Thomas O Eschemann et al. 'Effect of support surface treatment on the synthesis, structure, and performance of Co/CNT Fischer–Tropsch catalysts'. In: *Journal of Catalysis* 328 (2015), pp. 130–138. ISSN: 0021-9517. DOI: https://doi.org/10.1016/j.jcat.2014.12.010. URL: https://www.sciencedirect.com/science/article/pii/S0021951714003455.

[3] Haider Almkhelfe et al. 'Carbon nanotube-supported catalysts prepared by a modified photo-Fenton process for Fischer–Tropsch synthesis'. In: *Journal of Catalysis* 361 (2018), pp. 278–289. ISSN: 0021-9517. DOI: https://doi.org/10.1016/j.jcat.2018.02.009. URL: https://www.sciencedirect.com/science/article/pii/S0021951718300678.

[4] Francisco Rodríguez-reinoso. 'The role of carbon materials in heterogeneous catalysis'. In: *Carbon* 36.3 (1998), pp. 159–175. ISSN: 0008-6223. DOI: https://doi.org/10.1016/S0008-6223(97)00173-5. URL: https://www.sciencedirect.com/science/article/pii/S0008622397001735.

[5] Iann C Gerber and Philippe Serp. 'A Theory/Experience Description of Support Effects in Carbon-Supported Catalysts'. In: *Chemical Reviews* 120.2 (2020), pp. 1250–1349. ISSN: 0009-2665. DOI: 10.1021/acs.chemrev.9b00209. URL: https://doi.org/10.1021/acs.chemrev.9b00209.

[6] UNFCCC. 'The Paris Agreement'. In: *Paris Climate Change Conference - November 2015*. 2018.

[7] II Contribution of Working Groups I, H. Lee III to the Sixth Assessment Report of the Intergovernmental Panel on Climate Change [Core Writing Team and J. Romero (eds.)] *Paris Climate Change Conference - November 2015*. Tech. rep. Geneva, Switzerland: IPCC, 2023.

[8] Hannah Ritchie, Max Roser and Pablo Rosado. 'CO and Greenhouse Gas Emissions'. In: *Our World in Data* (2020).

[9] Paul T Anastas. *Green chemistry : theory and practice*. Ed. by John C Warner. Oxford: Oxford University Press, 1998. ISBN: 0198502346.

[10] Yanping Chen et al. 'Carbon-based catalysts for Fischer–Tropsch synthesis'. In: *Chemical Society Reviews* 50.4 (2021), pp. 2337–2366. ISSN: 0306-0012. DOI: 10.1039/D0CS00905A. URL: http://dx.doi.org/10.1039/D0CS00905A%20https://pubs.rsc.org/en/content/articlepdf/2021/cs/d0cs00905a.

[11] Olaf Deutschmann et al. 'Heterogeneous Catalysis and Solid Catalysts, 3. Industrial Applications'. In: *Ullmann's Encyclopedia of Industrial Chemistry*. DOI: https://doi.org/10.1002/14356007.o05{_}o03. URL: https://onlinelibrary.wiley.com/doi/abs/10.1002/14356007.o05_o03.

[12] Mark E Dry. 'The Fischer–Tropsch process: 1950–2000'. In: *Catalysis Today* 71.3 (2002), pp. 227–241. ISSN: 0920-5861. DOI: https://doi.org/10.1016/S0920-5861(01)00453-9. URL: https://www.sciencedirect.com/science/article/pii/S0920586101004539.

[13] T W van Deelen et al. 'Assembly and activation of supported cobalt nanocrystal catalysts for the Fischer–Tropsch synthesis'. In: *Chemical Communications* 54.20 (2018), pp. 2530–2533. ISSN: 1359-7345. DOI: 10.1039/C7CC07741F. URL: http://dx.doi.org/10.1039/C7CC07741F.

[14] Sahra Louise Guldahl-Ibouder. *Preparation of selectively oxygen-functionalized carbon black as support for cobalt catalysts*. Trondheim, Dec. 2022.

[15] Tingjun Fu and Zhenhua Li. 'Review of recent development in Co-based catalysts supported on carbon materials for Fischer–Tropsch synthesis'. In: *Chemical Engineering Science* 135 (2015), pp. 3–20. ISSN: 0009-2509. DOI: https://doi.org/10.1016/j.ces.2015.03.007. URL: https://www.sciencedirect.com/science/article/pii/S0009250915001761.

[16] Tingjun Fu, Jing Lv and Zhenhua Li. 'Effect of Carbon Porosity and Cobalt Particle Size on the Catalytic Performance of Carbon Supported Cobalt Fischer–Tropsch Catalysts'. In: *Industrial & Engineering Chemistry Research* 53.4 (Jan. 2014), pp. 1342–1350. ISSN: 0888-5885. DOI: 10.1021/ie402128y. URL: https://doi.org/10.1021/ie402128y.

[17] Haifeng Xiong, Linda L Jewell and Neil J Coville. 'Shaped Carbons As Supports for the Catalytic Conversion of Syngas to Clean Fuels'. In: *ACS Catalysis* 5.4 (2015), pp. 2640–2658. DOI: 10.1021/acscatal.5b00090. URL: https://doi.org/10.1021/acscatal.5b00090.

[18] Ljubisa R Radovic. 'Physicochemical Properties of Carbon Materials: A Brief Overview'. In: *Carbon Materials for Catalysis*. 2008, pp. 1–44. DOI: https://doi.org/10.1002/9780470403709.ch1. URL: https://onlinelibrary.wiley.com/doi/abs/10.1002/9780470403709.ch1.

[19] Katsumi Kamegawa et al. 'Oxidative degradation of carbon blacks with nitric acid: II. Formation of water-soluble polynuclear aromatic compounds'. In: *Carbon* 40.9 (2002), pp. 1447–1455. ISSN: 0008-6223. DOI: https://doi.org/10.1016/S0008-6223(01)00310-4. URL: https://www.sciencedirect.com/science/article/pii/S0008622301003104.

[20] Randy Vander Wal et al. 'Carbon Nanostructure Examined by Lattice Fringe Analysis of High-Resolution Transmission Electron Microscopy Images'. In: *Applied spectroscopy* 58 (2004), pp. 230–237. DOI: 10.1366/000370204322842986.

[21] Qing Shi et al. 'Turning carbon black into hollow carbon nanospheres to encapsulate Fe2O3 as high-performance lithium-ion batteries anode'. In: *Microporous and Mesoporous Materials* 332 (2022), p. 111681. ISSN: 1387-1811. DOI: https://doi.org/10.1016/j.micromeso.2022.111681. URL: https://www.sciencedirect.com/science/article/pii/S1387181122000038.

[22] Venu Arunajatesan et al. 'Carbon-Supported Catalysts for the Chemical Industry'. In: *Carbon Materials for Catalysis*. 2008, pp. 535–572. DOI: https://doi.org/10.1002/9780470403709.ch15. URL: https://onlinelibrary.wiley.com/doi/abs/10.1002/9780470403709.ch15.

[23] Jean-Baptiste Donnet. *Carbon black: science and technology*. CRC Press, 1993. ISBN: 082478975X.

[24] Yalda Rangraz and Majid M Heravi. 'Recent advances in metal-free heteroatom-doped carbon heterogonous catalysts'. In: *RSC Advances* 11.38 (2021), pp. 23725–23778. DOI: 10.1039/D1RA03446D. URL: http://dx.doi.org/10.1039/D1RA03446D.

[25] Wei Qi et al. 'Oxidative Dehydrogenation on Nanocarbon: Intrinsic Catalytic Activity and Structure–Function Relationships'. In: *Angewandte Chemie International Edition* 54.46 (Nov. 2015), pp. 13682–13685. ISSN: 1433-7851. DOI: https://doi.org/10.1002/anie.201505818. URL: https://doi.org/10.1002/anie.201505818.

[26] Mohammad Saleh Shafeeyan et al. 'A review on surface modification of activated carbon for carbon dioxide adsorption'. In: *Journal of Analytical and Applied Pyrolysis* 89.2 (2010), pp. 143–151. ISSN: 0165-2370. DOI: https://doi.org/10.1016/j.jaap.2010.07.006. URL: https://www.sciencedirect.com/science/article/pii/S0165237010001063.

[27] Zhixin Yu et al. 'Role of surface oxygen in the preparation and deactivation of carbon nanofiber supported cobalt Fischer–Tropsch catalysts'. In: *Topics in Catalysis* 45.1 (2007), pp. 69–74. ISSN: 1572-9028. DOI: 10.1007/s11244-007-0242-7. URL: https://doi.org/10.1007/s11244-007-0242-7.

[28] Tijmen G Ros et al. 'Surface Oxidation of Carbon Nanofibres'. In: *Chemistry – A European Journal* 8.5 (2002), pp. 1151–1162. ISSN: 0947-6539. DOI: https://doi.org/10.1002/1521-3765(20020301)8:5⟨1151::AID-CHEM1151⟩3.0.CO;2-{\#}. URL: https://chemistry-europe.onlinelibrary.wiley.com/doi/abs/10.1002/1521-3765%2820020301%298%3A5%3C1151%3A%3AAID-CHEM1151%3E3.0.CO%3B2-%23.

[29] Tao Li et al. 'The Effect of Surface Wettability and Coalescence Dynamics in Catalytic Performance and Catalyst Preparation: A Review'. In: *ChemCatChem* 11.6 (Mar. 2019), pp. 1576–1586. ISSN: 1867-3880. DOI: https://doi.org/10.1002/cctc.201801925. URL: https://doi.org/10.1002/cctc.201801925.

[30] Shankhamala Kundu et al. 'Thermal Stability and Reducibility of Oxygen-Containing Functional Groups on Multiwalled Carbon Nanotube Surfaces: A Quantitative High-Resolution XPS and TPD/TPR Study'. In: *The Journal of Physical Chemistry C* 112.43 (2008), pp. 16869–16878. ISSN: 1932-7447. DOI: 10.1021/jp804413a. URL: https://doi.org/10.1021/jp804413a.

[31] Tingjun Fu et al. 'Effect of carbon support on Fischer–Tropsch synthesis activity and product distribution over Co-based catalysts'. In: *Fuel Processing Technology* 110 (2013), pp. 141–149. ISSN: 0378-3820. DOI: https://doi.org/10.1016/j.fuproc.2012.12.006. URL: https://www.sciencedirect.com/science/article/pii/S0378382012004535.

[32] S A Chernyak et al. 'Co catalysts supported on oxidized CNTs: Evolution of structure during preparation, reduction and catalytic test in Fischer-Tropsch synthesis'. In: *Applied Catalysis A: General* 523 (2016), pp. 221–229. ISSN: 0926-860X. DOI: https://doi.org/10.1016/j.apcata.2016.06.012. URL: https://www.sciencedirect.com/science/article/pii/S0926860X1630326X.

[33] Xu Chen et al. 'Mechanisms of surfactant adsorption on non-polar, air-oxidized and ozone-treated carbon surfaces'. In: *Carbon* 41.8 (2003), pp. 1489–1500. ISSN: 0008-6223. DOI: https://doi.org/10.1016/S0008-6223(03)00053-8. URL: https://www.sciencedirect.com/science/article/pii/S0008622303000538.

[34] V Datsyuk et al. 'Chemical oxidation of multiwalled carbon nanotubes'. In: *Carbon* 46.6 (2008), pp. 833–840. ISSN: 0008-6223. DOI: https://doi.org/10.1016/j.carbon.2008.02.012. URL: https://www.sciencedirect.com/science/article/pii/S0008622308000717.

[35] Jingjing Tang et al. 'Oxidation of acetylene black by nitric acid in hermetically sealed condition'. In: *Microporous and Mesoporous Materials* 193 (2014), pp. 54–60. ISSN: 1387-1811. DOI: https://doi.org/10.1016/j.micromeso.2014.03.020. URL: https://www.sciencedirect.com/science/article/pii/S138718111400136X.

[36] N Yao et al. 'Structure and Oxidation Patterns of Carbon Nanotubes'. In: *Journal of Materials Research* 13.9 (1998), pp. 2432–2437. ISSN: 2044-5326. DOI: 10.1557/JMR.1998.0338. URL: https://doi.org/10.1557/JMR.1998.0338.

[37] Hajime Serizawa et al. 'Effects of Oxidation of Carbon Black Surface on the Properties of Carbon Black–Natural Rubber Systems'. In: *Polymer Journal* 15.3 (1983), pp. 201–206. ISSN: 1349-0540. DOI: 10.1295/polymj.15.201. URL: https://doi.org/10.1295/polymj.15.201.

[38] J L Figueiredo et al. 'Modification of the surface chemistry of activated carbons'. In: *Carbon* 37.9 (1999), pp. 1379–1389. ISSN: 0008-6223. DOI: https://doi.org/10.1016/S0008-6223(98)00333-9. URL: https://www.sciencedirect.com/science/article/pii/S0008622398003339.

[39] Felix Herold et al. 'Synthesis strategies towards amorphous porous carbons with selective oxygen functionalization for the application as reference material'. In: *Carbon* 171 (2021), pp. 658–670. ISSN: 0008-6223. DOI: https://doi.org/10.1016/j.carbon.2020.09.030. URL: https://www.sciencedirect.com/science/article/pii/S0008622320308848.

[40] C A Leon y Leon et al. 'Evidence for the protonation of basal plane sites on carbon'. In: *Carbon* 30.5 (1992), pp. 797–811. ISSN: 0008-6223. DOI: https://doi.org/10.1016/0008-6223(92)90164-R. URL: https://www.sciencedirect.com/science/article/pii/000862239290164R.

[41] Felix Herold et al. 'Can Temperature-Programmed Techniques Provide the Gold Standard for Carbon Surface Characterization?' In: *Chemistry of Materials* (2022). ISSN: 0897-4756. DOI: 10.1021/acs.chemmater.2c02449. URL: https://doi.org/10.1021/acs.chemmater.2c02449.

[42] Maximilian Göckeler et al. 'Surface reactions during temperature-programmed desorption and reduction experiments with oxygen-functionalized carbon blacks'. In: *Applied Surface Science* 561 (2021), p. 150044. ISSN: 0169-4332. DOI: https://doi.org/10.1016/j.apsusc.2021.150044. URL: https://www.sciencedirect.com/science/article/pii/S016943322101120X.

[43] Peter J Hall and Joseph M Calo. 'Secondary interactions upon thermal desorption of surface oxides from coal chars'. In: *Energy & Fuels* 3.3 (May 1989), pp. 370–376. ISSN: 0887-0624. DOI: 10.1021/ef00015a020. URL: https://doi.org/10.1021/ef00015a020.

[44] Pascal Düngen, Robert Schlögl and Saskia Heumann. 'Non-linear thermogravimetric mass spectrometry of carbon materials providing direct speciation separation of oxygen functional groups'. In: *Carbon* 130 (2018), pp. 614–622. ISSN: 0008-6223. DOI: https://doi.org/10.1016/j.carbon.2018.01.047. URL: https://www.sciencedirect.com/science/article/pii/S0008622318300563.

[45] G Tremblay, F J Vastola and P L Walker. 'Thermal desorption analysis of oxygen surface complexes on carbon'. In: *Carbon* 16.1 (1978), pp. 35–39. ISSN: 0008-6223. DOI: https://doi.org/10.1016/0008-6223(78)90113-6. URL: https://www.sciencedirect.com/science/article/pii/0008622378901136.

[46] Q L Zhuang, Takashi Kyotani and A Tomita. 'DRIFT and TK/TPD analyses of surface oxygen complexes formed during carbon gasification'. In: *Energy & Fuels* 8.3 (1994), pp. 714–718. ISSN: 0887-0624.

[47] J Angel Menéndez et al. 'Low-Temperature Generation of Basic Carbon Surfaces by Hydrogen Spillover'. In: *The Journal of Physical Chemistry* 100.43 (1996), pp. 17243–17248. ISSN: 0022-3654. DOI: 10.1021/jp961243+. URL: https://doi.org/10.1021/jp961243+.

[48] J Angel Menéndez et al. 'On the Modification and Characterization of Chemical Surface Properties of Activated Carbon: In the Search of Carbons with Stable Basic Properties'. In: *Langmuir* 12.18 (1996), pp. 4404–4410. ISSN: 0743-7463. DOI: 10.1021/la9602022. URL: https://doi.org/10.1021/la9602022.

[49] Iris C ten Have and Bert M Weckhuysen. 'The active phase in cobalt-based Fischer-Tropsch synthesis'. In: *Chem Catalysis* 1.2 (2021), pp. 339–363. ISSN: 2667-1093. DOI: https://doi.org/10.1016/j.checat.2021.05.011. URL: https://www.sciencedirect.com/science/article/pii/S2667109321000427.

[50] Sharan Shetty and Rutger A van Santen. 'CO dissociation on Ru and Co surfaces: The initial step in the Fischer–Tropsch synthesis'. In: *Catalysis Today* 171.1 (2011), pp. 168–173. ISSN: 0920-5861. DOI: https://doi.org/10.1016/j.cattod.2011.04.006. URL: https://www.sciencedirect.com/science/article/pii/S0920586111002847.

[51] Eric van Steen and Hans Schulz. 'Polymerisation kinetics of the Fischer–Tropsch CO hydrogenation using iron and cobalt based catalysts'. In: *Applied Catalysis A: General* 186.1 (1999), pp. 309–320. ISSN: 0926-860X. DOI: https://doi.org/10.1016/S0926-860X(99)00151-9. URL: https://www.sciencedirect.com/science/article/pii/S0926860X99001519.

[52] Hans Schulz, Zhiqin Nie and Farid Ousmanov. 'Construction of the Fischer–Tropsch regime with cobalt catalysts'. In: *Catalysis Today* 71.3 (2002), pp. 351–360. ISSN: 0920-5861. DOI: https://doi.org/10.1016/S0920-5861(01)00462-X. URL: https://www.sciencedirect.com/science/article/pii/S092058610100462X.

[53] Jin-Xun Liu et al. 'Crystallographic Dependence of CO Activation on Cobalt Catalysts: HCP versus FCC'. In: *Journal of the American Chemical Society* 135.44 (2013), pp. 16284–16287. ISSN: 0002-7863. DOI: 10.1021/ja408521w. URL: https://doi.org/10.1021/ja408521w.

[54] Shuai Lyu et al. 'Role of Active Phase in Fischer–Tropsch Synthesis: Experimental Evidence of CO Activation over Single-Phase Cobalt Catalysts'. In: *ACS Catalysis* 8.9 (2018), pp. 7787–7798. DOI: 10.1021/acscatal.8b00834. URL: https://doi.org/10.1021/acscatal.8b00834.

[55] Gérôme Melaet et al. 'Evidence of Highly Active Cobalt Oxide Catalyst for the Fischer–Tropsch Synthesis and CO2 Hydrogenation'. In: *Journal of the American Chemical Society* 136.6 (2014), pp. 2260–2263. ISSN: 0002-7863. DOI: 10.1021/ja412447q. URL: https://doi.org/10.1021/ja412447q.

[56] Yan-Peng Pei et al. 'High Alcohols Synthesis via Fischer–Tropsch Reaction at Cobalt Metal/Carbide Interface'. In: *ACS Catalysis* 5.6 (2015), pp. 3620–3624. DOI: 10.1021/acscatal.5b00791. URL: https://doi.org/10.1021/acscatal.5b00791.

[57] Osamu Kitakami et al. 'Size effect on the crystal phase of cobalt fine particles'. In: *Physical Review B* 56 (1997), pp. 13849–13854.

[58] Nikolaos E Tsakoumis et al. 'A combined in situ XAS-XRPD-Raman study of Fischer–Tropsch synthesis over a carbon supported Co catalyst'. In: *Catalysis Today* 205 (2013), pp. 86–93. ISSN: 0920-5861. DOI: https://doi.org/10.1016/j.cattod.2012.08.041. URL: https://www.sciencedirect.com/science/article/pii/S092058611200627X.

[59] G Leendert Bezemer et al. 'Cobalt Particle Size Effects in the FischerTropsch Reaction Studied with Carbon Nanofiber Supported Catalysts'. In: *Journal of the American Chemical Society* 128.12 (2006), pp. 3956–3964. ISSN: 0002-7863. DOI: 10.1021/ja058282w. URL: https://doi.org/10.1021/ja058282w.

[60] J P den Breejen et al. 'On the Origin of the Cobalt Particle Size Effects in Fischer-Tropsch Catalysis'. In: *Journal of the American Chemical Society* 131.20 (2009), pp. 7197–7203. ISSN: 0002-7863. DOI: 10.1021/ja901006x. URL: https://doi.org/10.1021/ja901006x.

[61] Gonzalo Prieto et al. 'Cobalt particle size effects in Fischer–Tropsch synthesis: structural and in situ spectroscopic characterisation on reverse micelle-synthesised Co/ITQ-2 model catalysts'. In: *Journal of Catalysis* 266.1 (2009), pp. 129–144. ISSN: 0021-9517. DOI: https://doi.org/10.1016/j.jcat.2009.06.001. URL: https://www.sciencedirect.com/science/article/pii/S0021951709001869.

[62] Hilde J Venvik, Anne Borg and Cecilie Berg. 'Formation of the CO-induced (3 × 1) surface structure on Co(112̄0) studied by STM'. In: *Surface Science* 397.1 (1998), pp. 322–332. ISSN: 0039-6028. DOI: https://doi.org/10.1016/S0039-6028(97)00751-6. URL: https://www.sciencedirect.com/science/article/pii/S0039602897007516.

[63] H J Venvik, C Berg and A Borg. 'CO adsorption on Co(1012) – a STM study'. In: *Surface Science* 402-404 (1998), pp. 57–61. ISSN: 0039-6028. DOI: https://doi.org/10.1016/S0039-6028(97)01023-6. URL: https://www.sciencedirect.com/science/article/pii/S0039602897010236.

[64] Jon Wilson and Cor de Groot. 'Atomic-Scale Restructuring in High-Pressure Catalysis'. In: *The Journal of Physical Chemistry* 99.20 (1995), pp. 7860–7866. ISSN: 0022-3654. DOI: 10.1021/j100020a005. URL: https://doi.org/10.1021/j100020a005.

[65] I M Ciobîcă et al. 'Adsorbate induced reconstruction of cobalt surfaces'. In: *Surface Science* 602.1 (2008), pp. 17–27. ISSN: 0039-6028. DOI: https://doi.org/10.1016/j.susc.2007.09.060. URL: https://www.sciencedirect.com/science/article/pii/S0039602807009260.

[66] T W van Deelen et al. 'Cobalt nanocrystals on carbon nanotubes in the Fischer-Tropsch synthesis: Impact of support oxidation'. In: *Applied Catalysis A: General* 593 (2020), p. 117441. ISSN: 0926-860X. DOI: https://doi.org/10.1016/j.apcata.2020.117441. URL: https://www.sciencedirect.com/science/article/pii/S0926860X2030034X.

[67] Sergei A Chernyak et al. 'Effect of Co crystallinity on Co/CNT catalytic activity in CO/CO2 hydrogenation and CO disproportionation'. In: *Applied Surface Science* 372 (2016), pp. 100–107. ISSN: 0169-4332. DOI: https://doi.org/10.1016/j.apsusc.2016.03.052. URL: https://www.sciencedirect.com/science/article/pii/S0169433216304883.

[68] Maryam Davari et al. 'Enhancement of activity, selectivity and stability of CNTs-supported cobalt catalyst in Fischer–Tropsch via CNTs functionalization'. In: *Applied Catalysis A: General* 485 (2014), pp. 133–142. ISSN: 0926-860X. DOI: https://doi.org/10.1016/j.apcata.2014.07.023. URL: https://www.sciencedirect.com/science/article/pii/S0926860X14004530.

[69] Mariane Trépanier et al. 'Fischer–Tropsch synthesis over carbon nanotubes supported cobalt catalysts in a fixed bed reactor: Influence of acid treatment'. In: *Fuel Processing Technology* 90.3 (2009), pp. 367–374. ISSN: 0378-3820. DOI: https://doi.org/10.1016/j.fuproc.2008.10.012. URL: https://www.sciencedirect.com/science/article/pii/S0378382008002683.

[70] Kang Cheng et al. 'Chapter Three - Advances in Catalysis for Syngas Conversion to Hydrocarbons'. In: *Advances in Catalysis*. Ed. by Chunshan Song. Vol. 60. Academic Press, 2017, pp. 125–208. ISBN: 0360-0564. DOI: https://doi.org/10.1016/bs.acat.2017.09.003. URL: https://www.sciencedirect.com/science/article/pii/S0360056417300032.

[71] Erling Rytter, Nikolaos E Tsakoumis and Anders Holmen. 'On the selectivity to higher hydrocarbons in Co-based Fischer–Tropsch synthesis'. In: *Catalysis Today* 261 (2016), pp. 3–16. ISSN: 0920-5861. DOI: https://doi.org/10.1016/j.cattod.2015.09.020. URL: https://www.sciencedirect.com/science/article/pii/S0920586115005945.

[72] Qinghong Zhang, Jincan Kang and Ye Wang. 'Development of Novel Catalysts for Fischer–Tropsch Synthesis: Tuning the Product Selectivity'. In: *ChemCatChem* 2.9 (Sept. 2010), pp. 1030–1058. ISSN: 1867-3880. DOI: https://doi.org/10.1002/cctc.201000071. URL: https://doi.org/10.1002/cctc.201000071.

[73] I Puskas and R S Hurlbut. 'Comments about the causes of deviations from the Anderson–Schulz–Flory distribution of the Fischer–Tropsch reaction products'. In: *Catalysis Today* 84.1 (2003), pp. 99–109. ISSN: 0920-5861. DOI: https://doi.org/10.1016/S0920-5861(03)00305-5. URL: https://www.sciencedirect.com/science/article/pii/S0920586103003055.

[74] Sara Lögdberg et al. 'Effect of water on the space-time yield of different supported cobalt catalysts during Fischer–Tropsch synthesis'. In: *Applied Catalysis A: General* 393.1 (2011), pp. 109–121. ISSN: 0926-860X. DOI: https://doi.org/10.1016/j.apcata.2010.11.030. URL: https://www.sciencedirect.com/science/article/pii/S0926860X10007970.

[75] Sara Lögdberg et al. 'On the selectivity of cobalt-based Fischer–Tropsch catalysts: Evidence for a common precursor for methane and long-chain hydrocarbons'. In: *Journal of Catalysis* 274.1 (2010), pp. 84–98. ISSN: 0021-9517. DOI: https://doi.org/10.1016/j.jcat.2010.06.007. URL: https://www.sciencedirect.com/science/article/pii/S0021951710002125.

[76] C J Weststrate and J W Niemantsverdriet. 'Understanding FTS selectivity: the crucial role of surface hydrogen'. In: *Faraday Discussions* 197.0 (2017), pp. 101–116. ISSN: 1359-6640. DOI: 10.1039/C6FD00191B. URL: http://dx.doi.org/10.1039/C6FD00191B.

[77] Heng Zhang et al. 'Hydrogen spillover effects in the Fischer–Tropsch reaction over carbon nanotube supported cobalt catalysts'. In: *Catalysis Science & Technology* 13.6 (2023), pp. 1888–1904. ISSN: 2044-4753. DOI: 10.1039/D3CY00014A. URL: http://dx.doi.org/10.1039/D3CY00014A.

[78] Zhao Wang, Frances H Yang and Ralph T Yang. 'Enhanced Hydrogen Spillover on Carbon Surfaces Modified by Oxygen Plasma'. In: *The Journal of Physical Chemistry C* 114.3 (2010), pp. 1601–1609. ISSN: 1932-7447. DOI: 10.1021/jp909480d. URL: https://doi.org/10.1021/jp909480d.

[79] Amel C Ghogia et al. 'Hydrogen Spillover in the Fischer-Tropsch Synthesis on Carbon-supported Cobalt Catalysts'. In: *ChemCatChem* 12.4 (2020), pp. 1117–1128. ISSN: 1867-3880. DOI: https://doi.org/10.1002/cctc.201901934. URL: https://chemistry-europe.onlinelibrary.wiley.com/doi/abs/10.1002/cctc.201901934.

[80] Erling Rytter and Anders Holmen. 'Perspectives on the Effect of Water in Cobalt Fischer–Tropsch Synthesis'. In: *ACS Catalysis* 7.8 (2017), pp. 5321–5328. DOI: 10.1021/acscatal.7b01525. URL: https://doi.org/10.1021/acscatal.7b01525.

[81] Ali Nakhaei Pour, Mohammad Reza Housaindokht and Seyed Mehdi Kamali Shahri. 'Fischer–Tropsch Synthesis over Cobalt/CNTs Catalysts: Functionalized Support and Catalyst Preparation Effect on Activity and Kinetic Parameters'. In: *Industrial & Engineering Chemistry Research* 57.41 (2018), pp. 13639–13649. ISSN: 0888-5885. DOI: 10.1021/acs.iecr.8b02485. URL: https://doi.org/10.1021/acs.iecr.8b02485.

[82] Nikolaos E Tsakoumis et al. 'Deactivation of cobalt based Fischer–Tropsch catalysts: A review'. In: *Catalysis Today* 154.3 (2010), pp. 162–182. ISSN: 0920-5861. DOI: https://doi.org/10.1016/j.cattod.2010.02.077. URL: https://www.sciencedirect.com/science/article/pii/S0920586110002282.

[83] J A Moulijn, A E van Diepen and F Kapteijn. 'Catalyst deactivation: is it predictable?: What to do?' In: *Applied Catalysis A: General* 212.1 (2001), pp. 3–16. ISSN: 0926-860X. DOI: https://doi.org/10.1016/S0926-860X(00)00842-5. URL: https://www.sciencedirect.com/science/article/pii/S0926860X00008425.

[84] Ali Karimi et al. 'Functional group effect on carbon nanotube (CNT)-supported cobalt catalysts in Fischer–Tropsch synthesis activity, selectivity and stability'. In: *Fuel* 117 (2014), pp. 1045–1051. ISSN: 0016-2361. DOI: https://doi.org/10.1016/j.fuel.2013.10.014. URL: https://www.sciencedirect.com/science/article/pii/S0016236113009551.

[85] Eric van Steen et al. 'Stability of Nanocrystals: Thermodynamic Analysis of Oxidation and Re-reduction of Cobalt in Water/Hydrogen Mixtures'. In: *The Journal of Physical Chemistry B* 109.8 (Mar. 2005), pp. 3575–3577. ISSN: 1520-6106. DOI: 10.1021/jp045136o. URL: https://doi.org/10.1021/jp045136o.

[86] Iann Gerber et al. 'Theoretical and Experimental Studies on the Carbon-Nanotube Surface Oxidation by Nitric Acid: Interplay between Functionalization and Vacancy Enlargement'. In: *Chemistry – A European Journal* 17.41 (Oct. 2011), pp. 11467–11477. ISSN: 0947-6539. DOI: https://doi.org/10.1002/chem.201101438. URL: https://doi.org/10.1002/chem.201101438.

[87] Antônio M Da Silva, Hélio F Dos Santos and Paolo Giannozzi. 'Carbonyl group generation on single-wall carbon nanotubes with nitric acid: A theoretical description'. In: *Chemical Physics Letters* 582 (2013), pp. 123–128. ISSN: 0009-2614. DOI: https://doi.org/10.1016/j.cplett.2013.07.058. URL: https://www.sciencedirect.com/science/article/pii/S0009261413009494.

[88] Aliya F Khusnuriyalova et al. 'Preparation of Cobalt Nanoparticles'. In: *European Journal of Inorganic Chemistry* 2021.30 (Aug. 2021), pp. 3023–3047. ISSN: 1434-1948. DOI: https://doi.org/10.1002/ejic.202100367. URL: https://doi.org/10.1002/ejic.202100367.

[89] Celso de Mello Donegá. 'Synthesis and properties of colloidal heteronanocrystals'. In: *Chemical Society Reviews* 40.3 (2011), pp. 1512–1546. ISSN: 0306-0012. DOI: 10.1039/C0CS00055H. URL: http://dx.doi.org/10.1039/C0CS00055H.

[90] Soon Gu Kwon and Taeghwan Hyeon. 'Formation Mechanisms of Uniform Nanocrystals via Hot-Injection and Heat-Up Methods'. In: *Small* 7.19 (Oct. 2011), pp. 2685–2702. ISSN: 1613-6810. DOI: https://doi.org/10.1002/smll.201002022. URL: https://doi.org/10.1002/smll.201002022.

[91] John Regalbuto. *Catalyst preparation : science and engineering*. Boca Raton, Fla: CRC Press, 2007. ISBN: 9780849370885.

[92] Dan Guo, Guoxin Xie and Jianbin Luo. 'Mechanical properties of nanoparticles: basics and applications'. In: *Journal of Physics D: Applied Physics* 47.1 (2014), p. 013001. ISSN: 0022-3727. DOI: 10.1088/0022-3727/47/1/013001. URL: https://dx.doi.org/10.1088/0022-3727/47/1/013001.

[93] Matthias Thommes et al. 'Physisorption of gases, with special reference to the evaluation of surface area and pore size distribution (IUPAC Technical Report)'. In: *Pure and Applied Chemistry* 87.9-10 (2015), pp. 1051–1069. DOI: doi:10.1515/pac-2014-1117. URL: https://doi.org/10.1515/pac-2014-1117.

[94] 'Solid Catalysts'. In: *Concepts of Modern Catalysis and Kinetics*. 2003, pp. 167–214. DOI: https://doi.org/10.1002/3527602658.ch5. URL: https://onlinelibrary.wiley.com/doi/abs/10.1002/3527602658.ch5.

[95] 'Catalyst Characterization'. In: *Concepts of Modern Catalysis and Kinetics*. 2003, pp. 129–166. DOI: https://doi.org/10.1002/3527602658.ch4. URL: https://onlinelibrary.wiley.com/doi/abs/10.1002/3527602658.ch4.

[96] Boy Cornils. *Catalysis from A to Z : a concise encyclopedia : Vol. 3 : O to Z*. Vol. 3. Wiley-VCH, 2007.

[97] M A Reiche, M Maciejewski and A Baiker. 'Characterization by temperature programmed reduction'. In: *Catalysis Today* 56.4 (2000), pp. 347–355. ISSN: 0920-5861. DOI: https://doi.org/10.1016/S0920-5861(99)00294-1. URL: https://www.sciencedirect.com/science/article/pii/S0920586199002941.

[98] 'Introduction, Basic Theory and Principles'. In: *Modern Raman Spectroscopy – A Practical Approach*. 2004, pp. 1–21. DOI: https://doi.org/10.1002/0470011831.ch1. URL: https://onlinelibrary.wiley.com/doi/abs/10.1002/0470011831.ch1.

[99] V Balaram. 'Microwave plasma atomic emission spectrometry (MP-AES) and its applications – A critical review'. In: *Microchemical Journal* 159 (2020), p. 105483. ISSN: 0026-265X. DOI: https://doi.org/10.1016/j.microc.2020.105483. URL: https://www.sciencedirect.com/science/article/pii/S0026265X20311693.

[100] Muhammad Sajid Hamid Akash and Rehman Kanwal. *Essentials of Pharmaceutical Analysis*. 1st edition. Singapore: Springer Singapore, 2020.

[101] Werner Engewald and Katja Dettmer-Wilde. 'Introduction'. In: *Practical Gas Chromatography: A Comprehensive Reference*. Ed. by Katja Dettmer-Wilde and Werner Engewald. Berlin, Heidelberg: Springer Berlin Heidelberg, 2014, pp. 3–20. ISBN: 978-3-642-54640-2. DOI: 10.1007/978-3-642-54640-2{_}1. URL: https://doi.org/10.1007/978-3-642-54640-2_1.

[102] Viacheslav Iablokov et al. 'Size-Controlled Model Co Nanoparticle Catalysts for CO2 Hydrogenation: Synthesis, Characterization, and Catalytic Reactions'. In: *Nano Letters* 12.6 (2012), pp. 3091–3096. ISSN: 1530-6984. DOI: 10.1021/nl300973b. URL: https://doi.org/10.1021/nl300973b.

[103] Philippe Mallet-Ladeira et al. 'A Raman study to obtain crystallite size of carbon materials: A better alternative to the Tuinstra–Koenig law'. In: *Carbon* 80 (2014), pp. 629–639. ISSN: 0008-6223. DOI: https://doi.org/10.1016/j.carbon.2014.09.006. URL: https://www.sciencedirect.com/science/article/pii/S0008622314008574.

[104] JunShi Tang et al. 'Oxidation behavior of a kind of carbon black'. In: *Science China-technological Sciences - SCI CHINA-TECHNOL SCI* 52 (2009), pp. 1535–1542. DOI: 10.1007/s11431-009-0196-z.

[105] A C Ferrari and J Robertson. 'Raman spectroscopy of amorphous, nanostructured, diamond-like carbon, and nanodiamond'. eng. In: *Philos Trans A Math Phys Eng Sci* 362.1824 (2004), pp. 2477–2512. ISSN: 1364-503X (Print) 1364-503x. DOI: 10.1098/rsta.2004.1452.

[106] F Tuinstra and J L Koenig. 'Raman Spectrum of Graphite'. In: *The Journal of Chemical Physics* 53.3 (Sept. 2003), pp. 1126–1130. ISSN: 0021-9606. DOI: 10.1063/1.1674108. URL: https://doi.org/10.1063/1.1674108.

[107] Yoshinobu Otake and Robert G Jenkins. 'Characterization of oxygen-containing surface complexes created on a microporous carbon by air and nitric acid treatment'. In: *Carbon* 31.1 (1993), pp. 109–121. ISSN: 0008-6223. DOI: https://doi.org/10.1016/0008-6223(93)90163-5. URL: https://www.sciencedirect.com/science/article/pii/0008622393901635.

[108] Calvin H Bartholomew. 'Mechanisms of catalyst deactivation'. In: *Applied Catalysis A: General* 212.1 (2001), pp. 17–60. ISSN: 0926-860X. DOI: https://doi.org/10.1016/S0926-860X(00)00843-7. URL: https://www.sciencedirect.com/science/article/pii/S0926860X00008437.

[109] Eric van Steen et al. 'Stability of Nanocrystals: Thermodynamic Analysis of Oxidation and Re-reduction of Cobalt in Water/Hydrogen Mixtures'. In: *The Journal of Physical Chemistry B* 109.8 (Mar. 2005), pp. 3575–3577. ISSN: 1520-6106. DOI: 10.1021/jp045136o. URL: https://doi.org/10.1021/jp045136o.

[110] C E Kliewer, G Kiss and S L Soled. 'Characterizing Intrinsic Deactivation in Cobalt-Catalyzed Fischer-Tropsch Synthesis'. In: *Microscopy and Microanalysis* 16.S2 (July 2010), pp. 1258–1259. ISSN: 1431-9276. DOI: 10.1017/S1431927610053547. URL: https://doi.org/10.1017/S1431927610053547.

Appendix A

TPD

A.1 Quantification of TPD data

The CO and CO_2 emissions were found by using the following conversion from vol% to mmol.

$$\dot{v} = \frac{vol\%}{100} \cdot \dot{V}_{tot} \tag{A.1}$$

$$\dot{n} = \frac{\dot{v}}{V_m} \tag{A.2}$$

Where $\dot{v}$ is the volumetric flowrate of either CO or CO_2, vol% is the volume prosent measured by the MS of the compound in question, $\dot{V_{tot}}$ is the total volumetric flowrate, $\dot{n}$ is the molar flowrate and V_m is the molar volume of gas, namely 22.4 L.

A.1.1 Fitting of TPD curves

The TPD data was fitted wit Gaussian curves. The following equation was used

$$y = Iexp(-(\frac{x - x_m}{FWHM})^2) \tag{A.3}$$

Where I is the intensity, x_m is the temperature at maximum intensity and FWHM is the full width at half maximum of the peak. The data was fitted in Excel with a least squares fit procedure and an evolutionary solving method. The temperatures for the maximum desorption as CO emissions were positioned at 85 ± 25°C for low temperature CO emissions, 500 ± 25°C for primary alcohols, 600 ± 25°C for phenols, 700 ± 25°C for ethers and 835 ± 35°C for quinones. For CO_2 the desorption temperatures were 260 ± 25°C for carboxylic acids, 270 ± 25°C for anhydrides, 645 ± 25°C for the first type of lactones, 790 ± 25°C for the second type of lactones. The HWHM was 85 ± 25°C for all species decomposing as CO and 100 ± 25°C for all species decomposing as CO_2. The

integrals were found by using a trapezoidal numeric integration method.

Appendix B

XPS

B.1 Fitting of XPS data

The energy axis was calibrated by fixing the C1s contribution of sp^2 hybridized carbon at 284.6 eV, and Shirley background subtraction was performed before fitting the data. Linear combinations between Gaussian and Lorentzian functions (Pseudo-Voigt profiles) were used for deconvolution.

B.1.1 C 1s orbital

The C 1s orbital was deconvoluted by assuming the contribution from sp^2 hybridized non-functionalized carbon at 284.6 ± 0.1 eV, carbon bound to oxygen via a single bond at 286.1 ± 0.1 eV, carbon bound to oxygen via a double bond at 287.5 ± 0.1 eV, carboxylic acid derivatives at 289.0 ± 0.1 eV, and the $\pi \rightarrow \pi*$ shakeup-line at 290.5 ± 0.1 eV. The Full width at half maximum (FWHM) was restricted to be between 1 eV and 1.6 eV for all contributions.

B.1.2 O 1s orbital

The O 1s regions were fitted assuming the contribution from oxygen bound to carbon via a single bond at 533.5 ± 0.2 eV, oxygen bound to carbon via a double bond at 532.0 ± 0.2 eV, and adsorped water at 535.2 ± 0.2 eV. The FWHM was restricted to be between 1.4 eV and 1.8 eV for all contributions.

B.1.3 XPS spectra

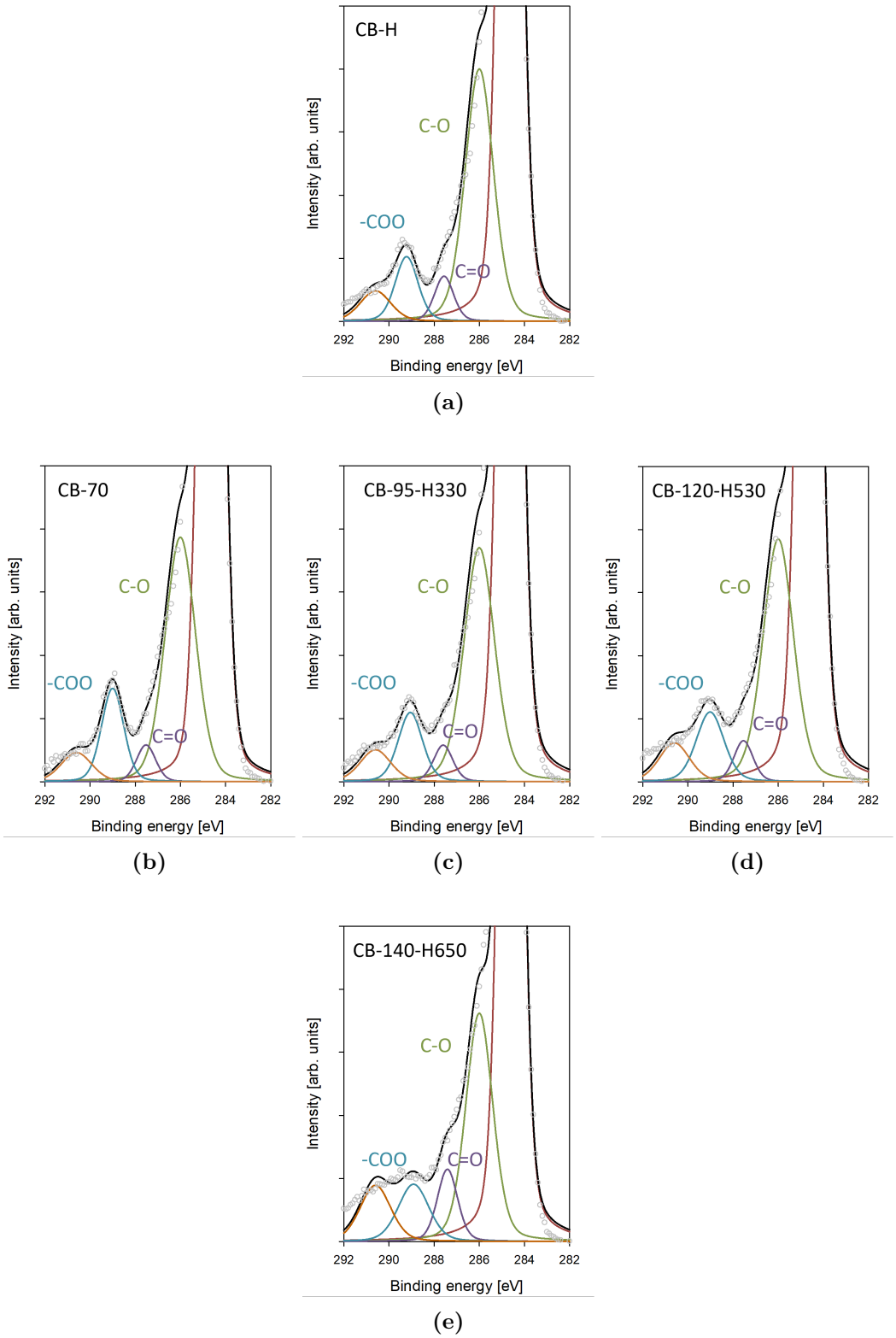

Figure B.1: Deconvoluted C 1s orbital.

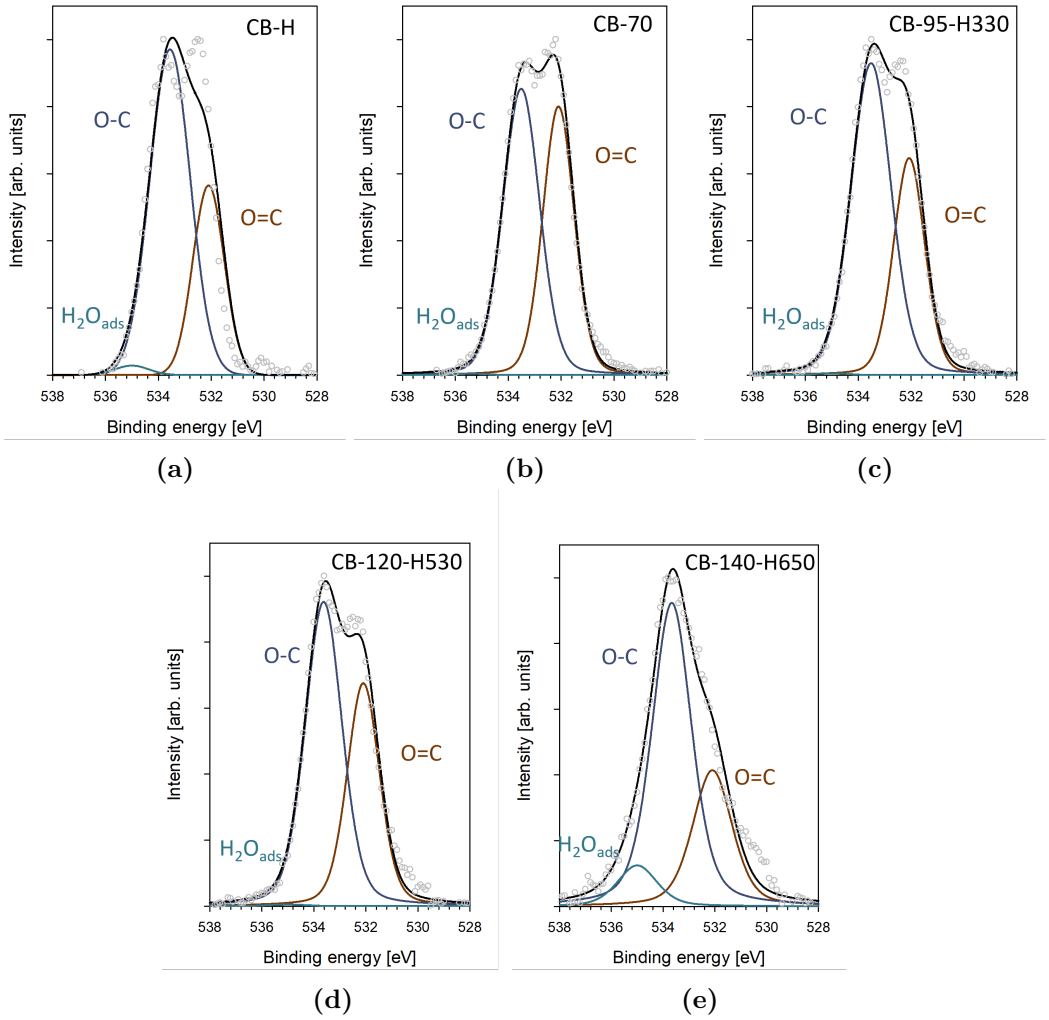

Figure B.2: Deconvoluted O 1s orbital

Appendix C

Raman spectroscopy

C.1 Deconvolution of Raman spectra

The deconvolution of Raman spectra was performed according to a procedure by Mallet-Ladeira et al.[103]. The D1 and D2 peak were fitted with two Lorentzians located at the same wavenumber. The G peak was fitted with a Breit-Wigner-Fano shape. The D' peak was also fitted with a Lorentzian function.

C.2 Crystallinity parameters

Table C.1: Ratio between D and G peak, position of the G peak, and half width at half maximum for the G peak for all the catalyst supports.

	ID/IG	G position	$HWHM_G$
CB-H	1.25 ± 0.05	1594.2 ± 3.6	41.8 ± 2.0
CB-70	1.27 ± 0.05	1597.9 ± 1.2	43.6 ± 3.4
CB-95-H330	1.22 ± 0.04	1598.6 ± 1.8	44.3 ± 2.0
CB-120-H530	1.28 ± 0.05	1595.8 ± 2.6	42.9 ± 0.9
CB-140-H650	1.25 ± 0.09	1602.9 ± 3.1	45.0 ± 3.5

Appendix D

Nitrogen adsorption-desorption

D.1 Sample weight

Table D.1: Weight of measured sample used to find the specific surface area of the catalyst suppors

	Weight [mg]
CB-H	58.4
CB-70	57.6
CB-95-H330	60.8
CB-120-H530	61.4
CB-140-H650	54.4

D.2 Physisorption isotherms

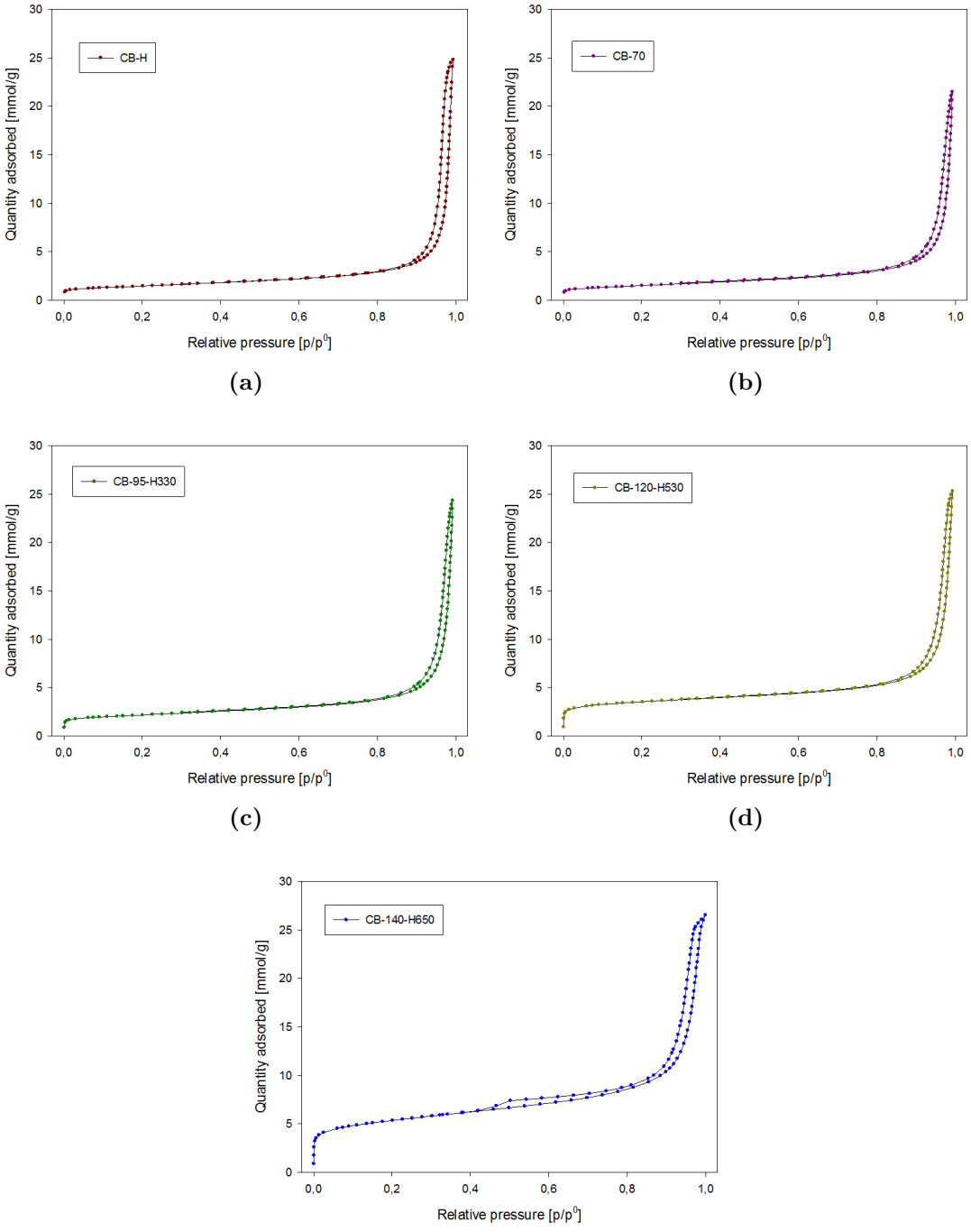

Figure D.1: N_2 physisorption isotherms for all catalyst supports

Appendix E

Particle size distributions

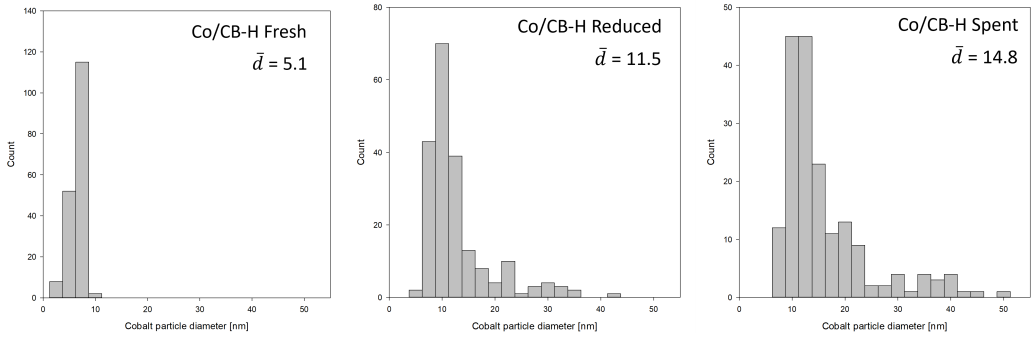

(a) **(b)** **(c)**

Figure E.1: Particle size distribution for fresh, reduced and spent catalyst Co/CB-H

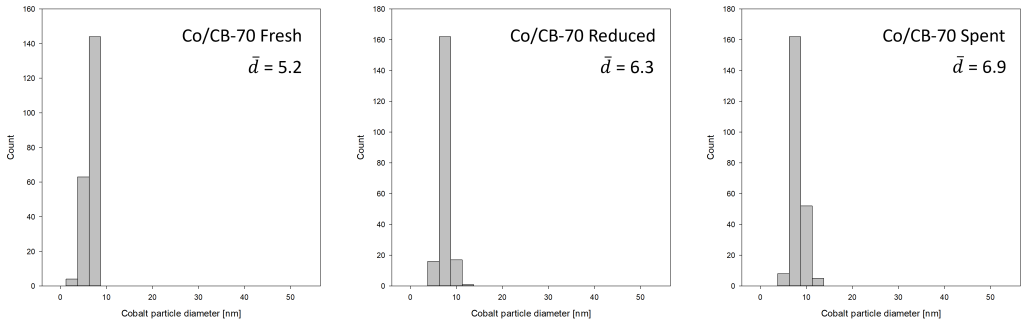

(a) **(b)** **(c)**

Figure E.2: Particle size distribution for fresh, reduced and spent catalyst Co/CB-70

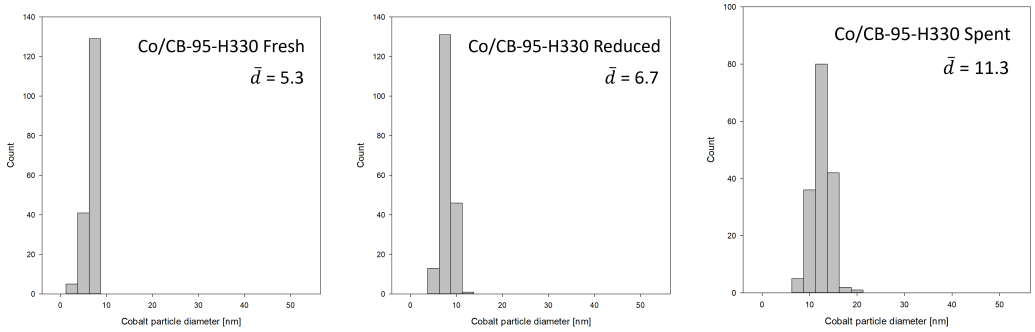

(a) **(b)** **(c)**

Figure E.3: Particle size distribution for fresh, reduced and spent catalyst Co/CB-95-H330

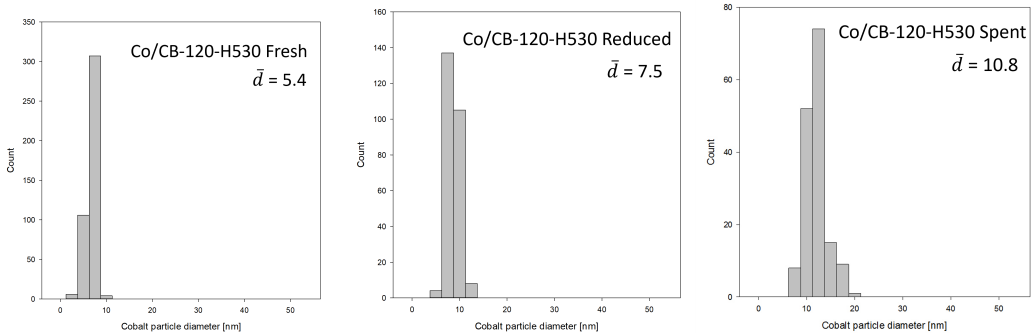

(a) **(b)** **(c)**

Figure E.4: Particle size distribution for fresh, reduced and spent catalyst Co/CB-120-H530

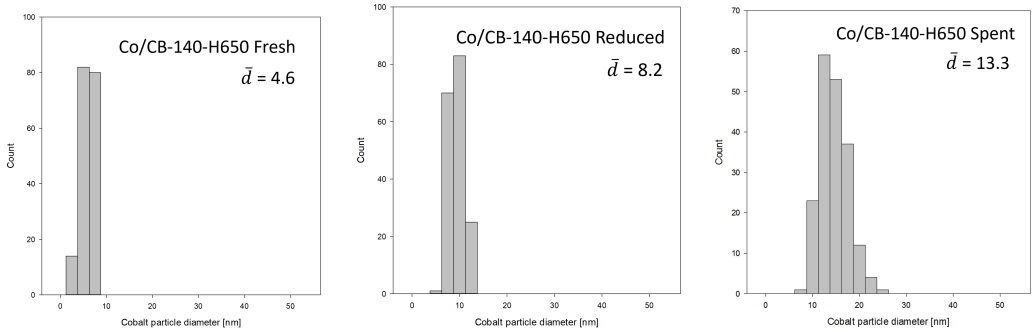

(a) **(b)** **(c)**

Figure E.5: Particle size distribution for fresh, reduced and spent catalyst Co/CB-140-H650

Appendix F

MP-AES

Table F.1: Weight of the samples used for MP-AES to determine cobalt loading.

	weight [mg]
CB-H	29.3
CB-70	38.9
CB-95-H330	31.8
CB-120-H530	30.2
CB-140-H650	33.8

Appendix G

TPR

G.1 Sample weight

Table G.1: Weight of measured sample used for TPR. Both a linear temperature program, and a reduction program mimicking the reduction the catalyst is subjected to prior to synthesis.

	weight for temperature ramp [mg]	weight for 8 h reduction program [mg]
CB-H	26.7	26.7
CB-70	28.5	26.2
CB-95-H330	27.1	28.4
CB-120-H530	25.8	26.8
CB-140-H650	26.7	28.0

G.2 TPR measurements

Two temperature programs were employed for the TPR measurements, one linear and one isothermal program with a temperature ramp from the reduction temperature at 350°C to 800°C. The measurements taken with a temperature ramp are shown in orange, while the isothermal program is presented as a blue graph.

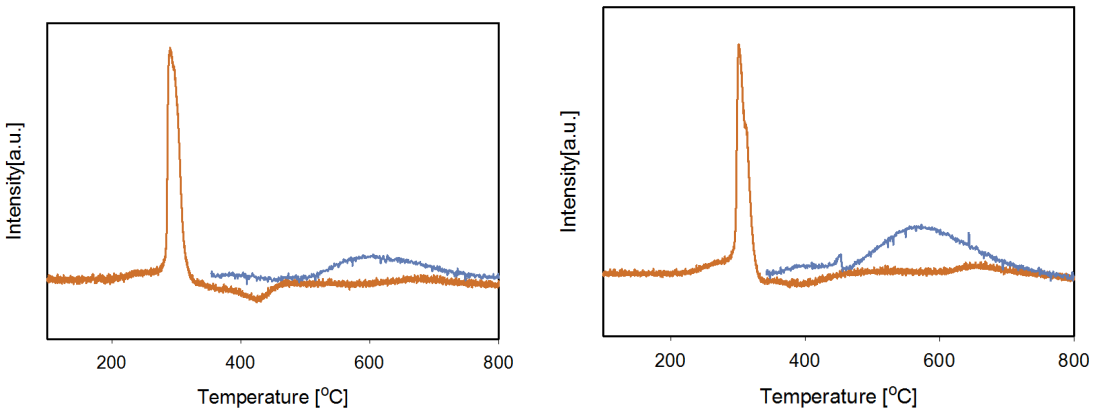

(a) Co/CB-H

(b) Co/CB-70

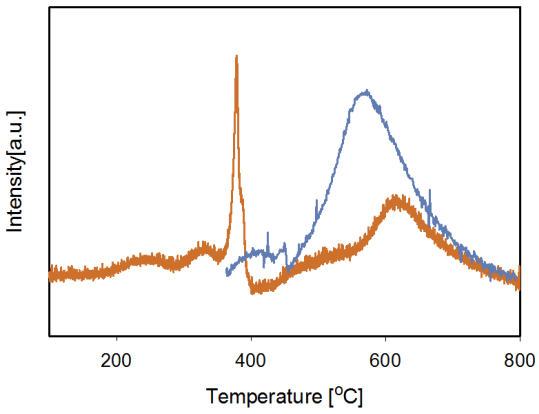

(c) Co/CB-95-H330

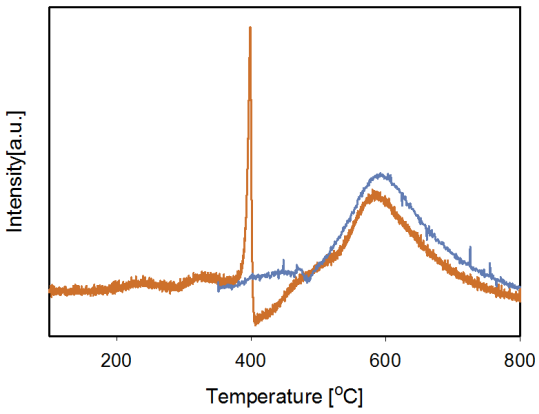

(d) Co/CB-120-H530

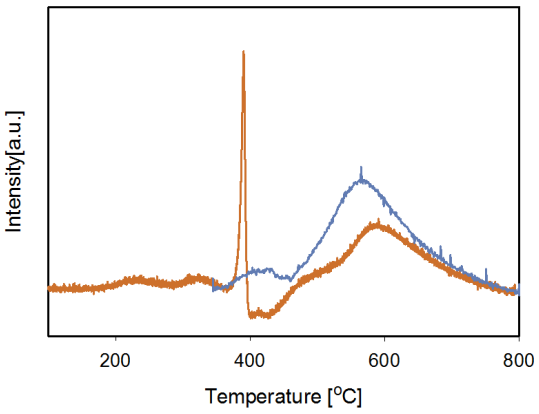

(e) Co/CB-140-H650

Figure G.1: TPR measurements for all the catalysts

Appendix H

Catalytic testing

The CO conversion, CTY, STY and selectivities from the catalytic tests were calculated from the concentration of species measured by a gas chromatograph.

H.1 Activity calculations

H.1.1 CO conversion

$$X_{CO} = 1 - \frac{CO/Ar}{CO_0/Ar_0} \tag{H.1}$$

$$CTY = \frac{X_{CO}}{m_{Co}} \tag{H.2}$$

Where CO and Ar are the concentrations of CO and Ar [vol%] at the time of the measurement, while CO_0 and Ar_0 are the inlet concentrations of CO and Ar to the reactor. X_{CO} is the conversion of CO, and m_{Co} is the mass of cobalt in the reactor.

$$\text{nb particles} = \frac{m_{Co}}{V_p \cdot \rho_{Co}} \tag{H.3}$$

$$n_{Co,surface} = \frac{A_p}{0.0662 \cdot N_A} \tag{H.4}$$

$$STY = \frac{X_{Co}}{n_{Co,surface} \cdot \text{nb particles}} \tag{H.5}$$

Where V_p is the volume of an average cobalt particle, ρ_{Co} is the density of cobalt, A_p is the total surface area of an average cobalt particle, 0.0662 is the cross-sectional area of one cobalt atom, and N_A is Avogadro's number.

H.2 Selectiviy calculations

The selectivity of hydrocarbons with carbon number n was calculated using the following equation.

$$S_{C_n} = \frac{C_n}{100} \cdot n \frac{V_{tot}}{X_{Co}} \tag{H.6}$$

$$S_{C5+} = 1 - (S_{C_1} + S_{C_2} + S_{C_3} + S_{C_4}) \tag{H.7}$$

Appendix I

P&ID

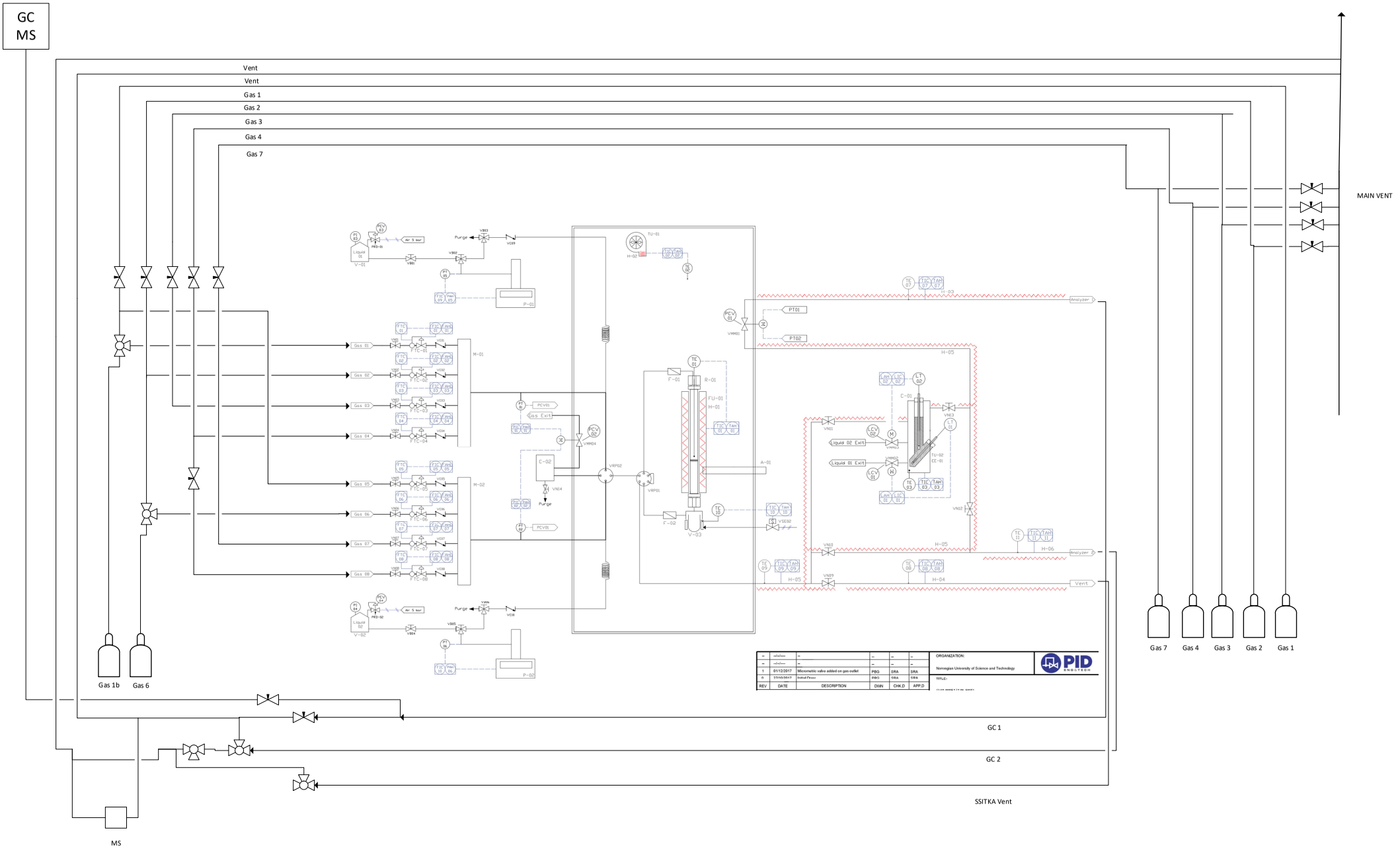
GC
MS
Vent
Vent
Gas 1
Gas 2
Gas 3
Gas 4
Gas 7
MAIN VENT
Gas 7
Gas 4
Gas 3
Gas 2
Gas 1
Gas 1b
Gas 6
GC 1
GC 2
SSITKA Vent
MS
ORGANIZATION:
Norwegian University of Science and Technology
PID ENGITECH
TITLE-
REV
DATE
DESCRIPTION
DWN
CHK.D
APP.D
01/12/2017
Micrometric valve added on gas outlet
PBG
SRA
SRA

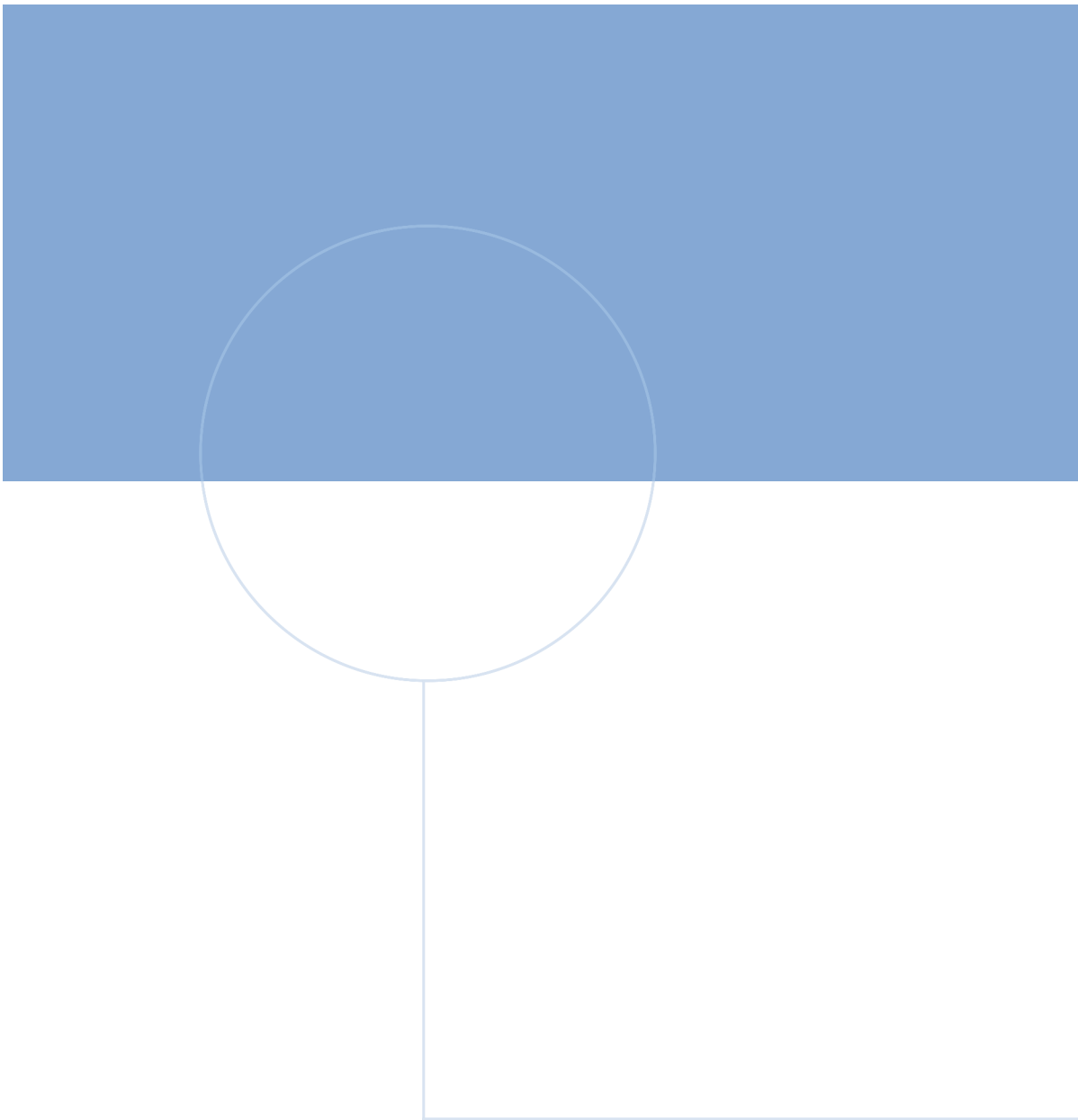

NTNU

Norwegian University of
Science and Technology